Achieving 100% roof-top based PV penetration in a low voltage distribution network

Sai Amith Chillamcherla

TU Delft
Delft
University of
Technology

Delft Center for Systems and Control

Achieving 100% roof-top based PV penetration in a low voltage distribution network

by

Sai Amith Chillamcherla

to obtain the degree of Master of Science in

Sustainable Energy Technology

at the Delft University of Technology,

to be defended publicly on Thursday August 26, 2021 at 10:00

TUDelft

PVMD
Delft University of Technology

ACKNOWLEDGEMENT

When it comes to how important advanced technologies are to society, I'm enthralled by the science of engineering and technology, particularly with regard to how significantly they've shaped our communal advancement. I am fascinated, for instance, by renewable energy technologies, which has a huge potential to dramatically change human civilization. TU Delft My master's degree in TU DELFT in sustainable energy technology has been an engaging two-year adventure that has introduced me to interesting and unique people from various backgrounds. Learning more about several sustainable energy technologies gave me time to enhance my skill set, that enabled to finish this project

I am grateful to my supervisors, Dr. Zameer Ahmad and Dr. Hesan Ziar, for assisting me in the completion of this thesis work. I am thankful to Dr. Gopinath for the invaluable support he has provided over the course of my thesis. His patience, affection and tolerance helped me to smoothly advance my thesis. This project would not have been completed effectively without the assistance of all of the individuals mentioned above. Additionally, I'd want to express my gratitude to Dr. René van Swaaij and Dr. P.P. (Pedro) Vergara Barrios for accepting my invitation to join my thesis committee.

Additionally, I'd want to express my gratitude to my pals Abhishek, Rohit and Sushanth for assisting me in multiple ways. Their contributions were important and aided me in refining the report. Additionally, I am grateful to them for reviewing my report. Also, I'd like to express my appreciation to my parents for their wise guidance and listening ear. They were there for me throughout the duration of my project's challenging periods.

<div align="right">

Delft, July 13th 2021
Sai Amith Chillamcherla

</div>

ABSTRACT

Given the merits of photovoltaic technology (PV), rooftop PV systems are becoming more prevalent in residential and commercial areas. As a result of the growing number of photovoltaic systems connected to low voltage (LV) distribution grids, a significant portion of power flow from photovoltaic arrays to the LV grid, As the PV penetration increases, this effect becomes more severe. This reversal of power flow (from the load side to the grid side) results in a voltage rise problem along the distribution feeder. Such an issue is more pronounced near the point of common coupling (PCC). Overvoltages are not desired as they can damage consumers' electronic devices, burn the insulation and can trip protective equipment, causing sudden power outages. The principal objective of this study is to achieve 100% PV penetration in a low voltage distribution network while maintaining voltages within the grid constraints by employing numerous voltage control techniques. To conduct PV penetration studies, the European low-voltage distribution benchmark network developed by CIGRE is selected.

PV systems of various configurations are designed and integrated into the CIGRE LV network. The results of the PV penetration analysis on the CIGRE network suggest that with the increase in the distance between the source and the load, the penetration level decreases drastically. The worst-case network model in which the penetration level is reduced to 65% is selected for employing voltage control strategies. Two main strategies have been used to improve pv penetration. In the first category of methods, the reactive power is controlled by the PV system so that voltages at the PCCs are within the grid voltage limits. Four different reactive power control methods are employed. The second category of methods are based on active power control, in which the voltages are controlled by batteries/electrolyzers by absorbing excess power generated by the PV system, avoiding reverse power flow into the grid.

The results obtained reveal that all the techniques employed are successful at increasing PV penetration to 100% without violating grid voltage limits. However, it is concluded that, batteries/electrolyzer systems provide better value in terms of effectiveness in solving the voltage rise issue. They also offers lower losses, and multiple-use cases.

ABBREVIATIONS AND SYMBOLS

IEEE: Institute of Electrical and Electronics Engineers
CIGRE: International Council on Large Electric Systems
LV network: Low voltage network
PV Photovoltaic
STC: Standard Test Conditions
DERs: Distributed energy resources
CTF: Comprehensive Test Feeder
NEV feeder: Neutral Earth Voltage feeder
EPRI: Electric Power Research Institute
PGE: Pacific Gas and Electric Company
PNNL Pacific Northwest National Laboratory
ABDTF: Agent-based distribution test feeders
ENSLVTN: European non-synthetic low-voltage test network
MPPT: Maximum power point tracking

MPP: Maximum power point
PWM: Pulse Width Modulation
GHI: Global horizontal irradiance
DHI: Diffuse horizontal irradiance
DNI: Direct normal irradiance
G_{direct}: Direct component of irradiance
In: Indium
CPC: Compound parabolic concentrating
SVF: Sky view factor
AOI: Angle of incidence
G_{total}: Total irradiance falling on the module
CPF: Constant power factor
VPF: Variable power factor
Q(V): Reactive power as a function of voltage
CRP: Constant reactive power
DC: Direct current
AC: Alternating current
P: Active power
Q: Reactive power
A_m: Module's Azimuth
A_s: Sun's Azimuth
a_m: Altitude of the module
a_s Altitude of the Sun
θ_m Tilt angle of the module
α: albedo
Θ_z: Angle between Zenith and sun position
R_s: Series resistance of a solar cell
R_p: Parallel resistance of a solar cell

I_0: Saturation current or dark current
n: Ideality factor
q: Charge of an electron
T: Temperature
K_B: Boltzman constant
I_{ph}: Photo-generated current
V_{oc}: Open circuit voltage
I_{sc}: Short circuit current
V_{MPP}: Voltage at maximum power point
I_{MPP}: Current at maximum power point
I_{in}: Irradiation at STC conditions
η: Efficiency of a solar cell
J_{MPP}: Current dunseity at MPP point
M: Number of cells connected in parallel

N: Number of cells connected in series
α_V: Temperature coefficient of V_{oc} :,
α_I: Temperature coefficient of I_{sc}
E_g: Bandgap of the semi conductor
K_{Eg}: Temperature dependence of the bandgap
ΔI: Ripple in inductor current
ΔV_{in}: Voltage ripple across the input capacitor
f: 50Hz AC frequency
$V_{DC-Link}$: Voltage across the DC link capacitor
e_d: Direct component of grid voltage
e_q: Quadrature component of grid voltage
i_d: Direct components of grid currents
i_q: Quadrature component of grid currents
k_p: Proportional constant
K_i: Integral constant
V_{PCC}: Voltage at PCC
V_0: Output voltage of the boost converter
I_0: Output current from the boost converter
L: Inductance
R: Resistance
C: Capacitance
i_d^*: Reference direct axis current
i_q^*: Reference qudrature axis current
V_{DC}: Reference DC-Link Voltage
X: Reactance
S: Sensitivity Matrix
Y: Admittance
PI: Proportional and Integral controller

CONTENTS

LIST OF FIGURES

LIST OF TABLES

1

INTRODUCTION

Climate change is one of the most pressing areas of concern at the nexus of human problems in the 21st century. Harmful emissions from utilizing conventional sources of energy like fossil fuels are the principal promoters of climate change. This results in an increasing global temperature, with catastrophic repercussions that threaten the lives of plants and fauna in the world, including humans [15]. Global surface temperatures have increased by about 1°C compared to the last century. The previous five years have been the hottest on record [16], [17]. Hence, this is followed by the faster melting of ice, increasing the water levels in the oceans. The world has been evolving around fossil fuel use for centuries as it is a predictable and reliable source. Nevertheless, governments and society are now conscious of the adverse effects of fossil fuels and are interested in taking the world in the direction of a clean and green future by utilizing renewable energy sources [18]. A drastic change to an all-renewable end would decrease greenhouse emissions significantly. Renewable energy sources like solar and wind energy could hold the key to combating climate change. Solar energy is omnipresent. It offers exceptional opportunities to make the energy transition feasible.

Over the past few decades, extensive research has been carried out in the field of photovoltaics. As a result, Photovoltaic (PV) modules are not only more efficient but are also more affordable and more reliable than ever before. The average commercial wafer-based silicon module efficiency has improved from 15% to 20% [19] during the last decade. Solar cells with a high concentration of multi-junctions attain an efficiency of up to 46.0% [20] in the laboratory today. The increasing popularity of PV modules across the globe can also be attributed to the ease of installation and modularity of PV technology. Over the next five years, the global photovoltaic industry is predicted to increase from 76.6 billion USD in 2020 to 222.3 billion USD by 2026 , at an average annual growth rate of 8.1% [21]. Government policies and activities that foster market expansion are the key drivers of the PV market. The need for PV systems for residential applications will be strong enough to further boost PV demand in the future. Also, the energy payback time has seen a significant improvement in recent years. It takes 2.5 years for PV systems in Northern Europe to balance the energy intake, but PV systems in southern Europe take no more than 1.5 years and are likely less, depending on the PV technology [22].

Given the merits of PV technology, the general public has expressed a strong desire to install PV systems on their houses' roofs (figure 1.1). Residential and commercial loads form a greater part of most power systems. For example, in the Netherlands and the US, domestic loads account for about 40% of total final energy consumption [23]. Ideally, electricity generation should be located close to the loads to avoid long-distance transmission losses and also this could help in reducing costs. Hence, PV system installations in residential/commercial buildings should be encouraged. This is indeed the best method to benefit both the customers and the grid. Rooftop photovoltaic (PV) systems are a type of distributed energy system that serves the energy needs of commercial and residential buildings in a distribution network. Land use becomes immaterial in the case of PV installations to the low voltage network. In the vast majority of situations, the system makes use of rooftops, building facades, windows, or parking lots, resulting in practicality, beauty, and better environmental friendliness. The benefits of rooftop-based PV system include-

- The absence of additional infrastructure (i.e. distribution network),

- Lower energy loss (due to closeness to load), and

- Improved voltage control and management.
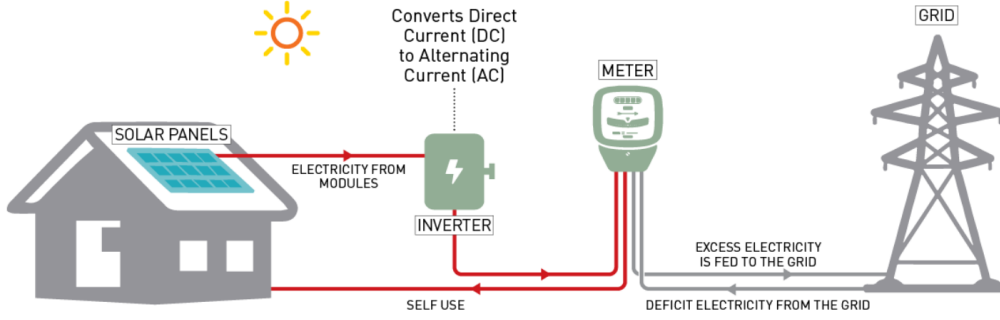
Figure 1.1: Grid connected roof-top PV system

Due to an increase in competitiveness in photovoltaics and to the government's increasing number of initiatives and programmes, the market for solar power is rapidly expanding. As well, FIT programmes in several nations have increased the business for rooftop PV. Global rooftop solar PV installation was worth $29.7 billion in 2016, and it is projected to grow to $64.7 billion over the next few years, representing a CAGR growth of 11.2% from 2017 to 2023 [24]. Consequently, it can be argued that the usage of small-scale PV systems will grow in residential and commercial building projects in the future.

1.1. Problem statement

Due to the increase in the number of PV systems used in low voltage distribution networks, challenges including overvoltages, line overloads, and voltage unbalancing may arise [25–32]. In general, the customer connected towards the end of the distribution feeder experiences the highest voltage drop due to the increased power losses along the distribution line. To avoid such loss, the transformer taps are positioned so that the secondary side voltage remains slightly above 1 p.u. Generally, such an approach should suffice for the distribution networks devoid of distributed energy systems like PV. However, with an increasing number of PV systems connected to LV grids, there will be a large amount of reverse power flow, especially as the level of photovoltaic power penetration increases. Therefore, the above method might not work accurately [30–32]. This reversal of energy flow can result in a variety of power quality problems, including voltage increase along the feeder. Overvoltage is not desired as it can damage consumers' electronic devices and can trip protective equipment, causing sudden power outages. To avoid overvoltages, two of the traditional methods are to decrease the PV penetration and use PV curtailment methods. [33–35]. The PV penetration is defined as the ratio of peak PV power generated and peak power consumed by the load over a particular period [36].

The voltage rise issue can be analytically described in the context of the system depicted in figure 1.2, where V_s and $Z_{line} = R_{line} + jX_{line}$ are the corresponding line parameters in the grid side of the distribution network. At the point of common coupling, the voltage is expressed as V_{Pcc}, as illustrated in the figure. Assuming, the power flows from PV system to the grid due to high PV penetration levels, the difference between the voltage at the PCC and the source voltage can be derived according to the following equations.

$$V_{Pcc} - V_s = i_{grid} Z_{line} \tag{1.1.1}$$

$$P = P_g - P_l \quad ; \quad Q = Q_g - Q_l$$

$$S = V_{Pcc} * i^*_{grid}$$

$$i_{grid} = \frac{S^*}{V^*_{Pcc}}$$

$$i_{grid} = \frac{P - jQ}{V^*_{Pcc}} \tag{1.1.2}$$

Inserting Eq. (1.1.2) in (1.1.1),

$$V_{Pcc} - V_s = \frac{PR_{line} + QX_{line}}{V_{Pcc}^*} + j\frac{PX_{line} - QR_{line}}{V_{Pcc}^*} \qquad (1.1.3)$$

Assuming, the network's $\frac{R}{X}$ ratios is high (typical to the LV networks) [37–39], the phase angle difference between V_{Pcc} and V_s points can be neglected resulting in,

$$V_{Pcc} - V_s = \frac{PR_{line} + QX_{line}}{|V_{Pcc}|} \qquad (1.1.4)$$

Where, P, Q are the excess active and reactive power sent into the grid. P_g and Q_g in the figure 1.2
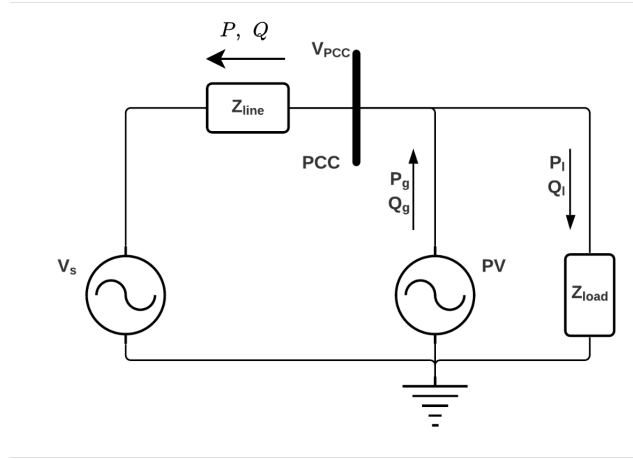
Figure 1.2: Circuit equivalent of PV system connected to the grid

denote the active and reactive power generated by the photovoltaic systems, respectively, while P_l and Q_l denote the active and reactive power consumed by the loads connected to the same PCC. It is evident from Eq. (1.1.4) that the voltage difference between the PCC and the alternating current (AC) voltage source on the grid side is positive. As a result, under the prior assumptions, it is reasonable to presume that the voltage at the PCC increases when the power flows in the opposite direction (from PV to the grid). The four parameters shown in the Eq. (1.1.4) affect the voltage at the PCC. P_l and Q_l are not the control variables (if demand side management is followed). The demand profiles set by the consumer must be met by the power supply from the source. Hence P_g and Q_g are the only variables that can assist in voltage support.

1.2. SCOPE OF THIS THESIS

The purpose of this study is to address the voltage rise issue and increase the PV penetration in the LV network, in the event of low electricity demand and high solar energy input. A plethora of techniques are recommended in the literature to address the voltage increase problem. They can be categorized as follows -

Upgrades to the network: One option is to increase the capacity of the distribution network by the use of thicker cables and higher-rated transformers, among other measures. However, such an approach necessitates a significant financial investment. Occasionally, during the installation process of new equipment (which could take several days), customers living nearby may be forced to endure unavoidable power disruptions due to safety concerns. Also, this method do not solve the voltage rise problem directly but makes the system more robust and resilient towards voltage rise problem.

Altering network state: The state or the stationary set point of the LV network can be altered to ensure optimal operation. One example is positioning the tap to increase or decrease the voltage on the secondary side of the transformer. However, the introduction of photovoltaic systems into the LV network increased the unpredictability of power flow. As a result, this necessitates frequent tap changes, which

is impractical.

PV system infrastructure: Inverter is one of the prime components of the PV systems infrastructure. They convert DC components to AC components. When employed with appropriate switching operations, the inverters can either absorb or generate reactive power. Such a strategy aids in the regulation of the voltage at the PCC. Additionally, the PCC voltage can be maintained by employing PV power curtailment techniques. These methods require the PV systems to function at an operating point other than maximum power point, limiting the PV power penetration into the grid. The obvious disadvantage of using this strategy is that the system does not perform at its peak efficiency.

Utilizing energy storage devices: Similarly, energy storage technologies such as batteries and electrolyzers employed in conjunction with PV systems can assist in maintaining the grid voltage at permissible levels by absorbing the extra power generated by the PV system, thus reducing the reverse power flow.

This thesis is primarily concerned with the third and fourth methods, which involves investigating and using various reactive power control methods and storage technologies to increase the PV penetration. All the strategies will be evaluated in terms of energy losses caused by reactive power absorption by the inverters in the photovoltaic system. Additionally, the electrolyzer/battery will be modelled as a load and will be employed in place of reactive power control schemes in order to maintain grid voltage. Finally, the importance of batteries and electrolyzers in sustaining grid voltage will be addressed.

1.3. GOAL OF THIS THESIS

To summarise, despite the benefits of rooftop photovoltaic installations, there are significant drawbacks, especially when PV penetration in the LV network approaches specific limits. Voltage rise is critical, among other problems. The primary goal of this project is to boost PV penetration to 100% without exceeding the grid voltage limit. Numerous strategies will be investigated in order to reach 100% penetration.

The project has the following objectives:

1. Literature study about PV penetration, low voltage distribution network and power electronic converters control.

2. Development of a dynamic model of a selected low voltage network and PV system infrastructure

3. Establish appropriate inverter control

4. Analysis of the impact of PV penetration on the developed LV distribution network

5. To apply various methods to increase the PV penetration to 100%, including minimum storage.

The following research questions will be addressed in this thesis:

- In a selected low voltage distribution network, what is the maximum PV penetration that may be achieved?

- How does the network's length influence the PV penetration?

- What are the primary strategies for achieving 100% pv penetration?

- What are the energy costs associated with implementing voltage control techniques?

- Which of the following strategies is the most effective for increasing PV penetration in an LV distribution network?

1.4. OUTLINE OF THIS THESIS

This section serves as a synopsis of the remainder of the thesis, guiding readers through this study on PV penetration. The rest of the study is as follows:

CHAPTER 2

This chapter outlines the literature study conducted as part of the thesis. To begin, a brief history of past work on the problem formulation of this thesis is presented. In the next section, literature study on several low voltage distribution grids is conducted, and the suitable grid is selected. Various MPPT algorithms, inverter topologies, and PWM approaches are explored in the following sections.

CHAPTER 3

This chapter discusses the modelling and design of several components in a photovoltaic system, including photovoltaic modules, inverters, MPPT, boost converters, and LC filters, as well as irradiance calculations. Following that, is a brief description of the control technique employed in this thesis. The plant models and control loops are provided for both the outer and inner control.

CHAPTER 4

This chapter discusses the outcomes of connecting the proposed photovoltaic system to the grid. Maximum voltage and the PV penetration studies are conducted on the selected low voltage distribution network.

CHAPTER 5

This chapter begins with an overview of the effect of reactive power on voltages. Then it is explained how reactive power can be absorbed and injected. Finally, four distinct reactive power control methods and two active power control strategies are presented as solutions.

CHAPTER 6

The results obtained after incorporating the reactive power control techniques into the inverter control are depicted. The chapter concludes with a brief discussion on the obtained outcomes.

CHAPTER 7

This chapter describes the final conclusions drawn from the findings of this thesis. Additionally, the limitations and future recommendations are discussed in detail.

2

LITERATURE RESEARCH

The preceding chapter introduced the problem that arises as a result of high PV penetration in the LV distribution network, as well as the goals of this thesis. This chapter describes the literature review that was undertaken as part of the study. The first section provides a brief history of previous work on the problem formulation of this thesis. In the next part, a literature review of several low voltage distribution grids is undertaken, and the suitable grid is ultimately chosen. The following section discusses the requirements and operation of MPPT trackers, and finally, the essential MPPT algorithms are reviewed and the preferred one is presented. Many inverter topologies have been published in the literature. The three-level inverter is selected among them. This inverter topology is covered in the following section. In the final section, PWM approaches are explored and the appropriate one is selected.

2.1. BACKGROUND

Penetration investigations on low voltage distribution networks are carried out in a variety of studies. For example, for penetration research, in [40] a small distribution feeder of around 150m is considered. Three different modes of voltage control operation were employed. PV systems can operate in one of three modes depending on the voltages detected at PCCs. There is no reactive power absorbed in mode one. In mode two, reactive power is absorbed, ensuring that the PCC maintains a PF of 0.9 at relatively higher voltages. For even higher voltages during peak insolation, the control functions in mode three, where, in addition to reactive power absorption, the power produced by the photovoltaic modules is limited by forcing them to operate at non-MPPT. The results indicate that a high level of PV penetration is possible with the selected network due to the line's low impedance.

In the journal [41], a thorough examination of the effects of various amounts of distributed generation (DG) penetration were conducted on an LV network based in Sutton, Newyork. The network is quite vast, with 1375 grid sections and 284 customers. In this study, distributed generators are assigned probabilistically to reflect for the uncertainty associated with potential DG installations. The results indicate that if grid consumers install DGs without constraints, the voltage rise problem emerges at approximately 30% of the minimum load penetration. Additionally, the results indicate that even at low penetration levels (2.5%), there may be a large or minor voltage rise problem if the DGs are placed in the incorrect location or if a large number of DGs are installed in a single site. However, high penetration levels of around 95% are possible if DGs are deployed in an appropriate manner, for as by requiring people to install DGs with a capacity equal to the minimum load. Similar findings have also been mentioned in [42] where voltage rise issue occurs at penetration level equal to or more than 135%. However, no voltage rise mitigation techniques are considered in this study.

In [43], a massive meshed urban LV distribution network centred on the metropolis of New Orleans, USA, was chosen for penetration investigations. The network is comprised of 1209 nodes, 1243 lines, and 169 transformers in total. This study considers three distinct scenarios. The first one featured 228 photovoltaic systems at various loads. In comparison, just 56 photovoltaic systems were erected near huge loads in the second scenario, whereas 172 photovoltaic systems were installed near residential loads with a maximum power consumption of less than 200kw. PV penetration reaches a maximum of 30%, 60%, and 90% in the three scenarios respectively. Additionally, there were a few instances where the ampere capacity of the lines was exceeded. Similar to the previous study, no voltage rise mitigation techniques are implemented.

Penetration studies were performed on a 312-house Swiss local network distribution network in [44]. The purpose of this study is to determine if the current distribution system is adequate for a future scenario in which photovoltaic (PV) generation accounts for 20% of total energy generated in Switzerland in 2050. According to the study, the LV network can support up to 43% PV penetration without experiencing significant voltage rise. Nonetheless, a voltage increase issue and transformer overloading have been discovered at the 100% penetration level. Active power curtailment, demand-side control, and battery storage technologies were utilised to address these issues. The losses exceed 20% of the maximum power generated by the photovoltaic array in the case of PV curtailment method. Finally, it was determined that a combination of active power curtailment and battery management techniques could greatly reduce losses. However, no reactive power control strategies were examined in this research to regulate the voltages at the PCC.

The PV penetration of a simulated LV radial network was investigated using an electronic on-load tap changing (EOLTC) transformer in [45]. This network consists of 20 nodes and a total of 60 houses, with each node equipped with a photovoltaic system. The simulation results show that without the EOLTC transformer, the network can support a 20% PV penetration without encountering voltage violations. The PV penetration level, however, was increased to 40 percent with the EOLTC transformer but reduced to 30 percent with greater line impedances. A research on a radial Low voltage distribution network in [46] found that adoption of Battery storage systems (BSS) can increase the PV systems hosting capacity of the distribution networks by preventing the voltage from rising more than a permissible level during peak irradiance.

The research reported in [47] demonstrates how energy storage in battery systems boosts PV penetration level in a radial LV distribution network. Any voltage violations are not detected until PV penetration reaches 50%. However, as PV penetration reached 80 percent, the LV distribution network encountered serious voltage rise issues and breached grid codes. As a result, the photovoltaic systems were disconnected from the grid to reduce the voltages at the PCCs. To avoid such disconnection, a 9kWH BSS is implemented, and in the end, it has been established that the BSS are effective in preventing voltage violations to a fair amount.

Monte Carlo methods have been used in [48], [49] and [50] for PV penetration studies. In Monte Carlo simulations a range is given to the system variables such as PV size, load profiles and locations where PV can be installed. Then, hundreds of simulations are carried out in the created domain to find the solution space based on the requirement and the problem. In [48] penetration studies were carried out on a real LV distribution network in the UK. OLTC transformer with novel control architecture has been used to increase penetration. The results conclude that the PV penetration has been increased from 30% to 50% with the adaptation of OLTC transformer with the appropriate control. Similar results were obtained in [50] and [49].

PV hosting capacity studies have been conducted for a rural LV distribution network in Brazil in [51]. It has been reported that if the PF is kept 0.92 there were no voltage violations detected at 30% PV penetration. To increase the PV penetration to 100% OLTC transformer has been used. A similar study has been conducted in [52] where a novel voltage droop control for the OLTC transformers along with a reactive power control technique has been used to enhance the PV systems hosting capacity of the selected low voltage network. It has been concluded by the authors that PV penetration can only reach up to 45% without causing serious voltage rise problems.

PV penetration research have been carried in all of the aforementioned studies utilising a variety of approaches, including reactive power management, PV power curtailment, and the use of storage and OLTC transformers. However, a comprehensive comparison in terms of active power losses across several reactive power techniques and battery storage systems was not conducted, nor was the fluctuation in PV penetration level with the length of distribution feeders investigated in one particular study. Additionally, several research omitted time-series simulations. Commercial, industrial, and residential network load patterns can be quite diverse. All of these networks were not included in any of the aforementioned works for penetration investigations. The penetration analysis for a low voltage distribution network comprised of residential, commercial, and industrial networks is done in this work of thesis.

Additionally, this study examines how the length of distribution network feeders affects penetration levels. The worst-case distance with the lowest PV penetration will be chosen to use active and reactive power strategies to improve PV penetration to 100% by lowering PCC voltages. Four distinct reactive power management techniques will be applied, as well as two active power control strategies based on electrolyser/battery storage systems. Finally, the active power losses incurred as a result of these approaches are quantified. PV power curtailment strategies are not employed since they can result in significant losses due to the PV modules' maximum output power not being supplied. Additionally, the whole inverter control strategy will be developed in terms of per-units to facilitate the design process.

2.2. DISTRIBUTION NETWORK

It is commonly acknowledged that the shift to widespread usage of distributed energy resources (DERs) such as photovoltaics is a critical challenge for the twenty-first century concerning grid integration. To enable abiding sustainable power production, considerable adjustments must be made to the power systems to facilitate architectures that are primarily or totally powered by renewables. Solutions for a successful transition to a sustainable energy future emphasize the efficient integrating of renewable energy sources into the system. To perform a comprehensive study on the influence of DERs on the grid, it is necessary to have appropriate benchmark test systems, including factual information on all the network elements, published in the literature. These test networks are intended to replicate the performance of a real network which could be used to analyze the effects of various new DERs on various network topologies. Unfortunately, due to data protection restrictions, distribution network data for most countries are not publicly accessible for usage as test samples. As a result, there are just a handful of original networks available for scientific and scholarly purposes today. Consequently, only a fewer number of European benchmark test networks have been documented in various studies, and even smaller numbers provide adequate information about the network components. A Comprehensive literature research on benchmark distribution networks has been carried out. This section discusses several of these networks. Ultimately, the network of choice will be presented.

In 1991, the IEEE (Institute of Electrical and Electronics Engineers) introduced the first test feeders [53].Each of these test feeders is a simplified representation of a real distribution network. In the ensuing years, an increasing number of test feeders are developed and added to the collection, again inspired by real networks in the United States. The new feeders include a range of special features. IEEE has only published a single test feeder based on the European grid infrastructure. In [13], the authors summarised what are all the 11 IEEE test feeders and their use cases in a form of a table as shown in the table 2.1.

13 bus feeder: Compared to the other test feeders this a small network consisting of 13 nodes and operates at 4.16KV. It can be categorized by its short length, high loading, a voltage regulator, overhead lines and underground cables, shunt capacitors and unbalanced loads [13, 53].

34 bus feeder: Modeled after a real-world feeder in Arizona and operates at a base voltage of 24.9 kV. It features a lengthy and light-loaded portion, two voltage regulators to ensure a steady voltages, a transformer for the short 4.16 kV part of the network, unbalanced loads, and shunt capacitors [13, 53].

37 bus feeder: This feeder is modelled after a real-world feeder in California and operates at a base voltage of 24.9 kV. All of the line are underground cables, the voltage regulation is provided at the substation, and the system is highly imbalanced with spot loads. Additionally, IEEE emphasizes that this particular circuit design is relatively unusual

123 bus feeder: As the name suggests, this feeder contains 123 buses and operates at 4.14KV. This network offers voltage drop problems which can be corrected by regulators and parallel cpacitor banks. [13, 53].This circuit is defined by the combination of overhead lines and underground cables, an unbalanced loads due to spot loads with constant current, voltage regulators, shunt capacitors, and several switches. IEEE states that this circuit is "well-behaved" and has few difficulties with convergence [13, 53].

ID	Total line Length (km)	Primary Voltage (kV)	Application Purpose
13 Node	2.49	4.16	Testing power-flow convergence problems for highly unbalanced systems
123 Node	11.96	4.16	Analysis of voltage drop problems, implementation of voltage management with voltage regulators
34 Node	93.91	24.9	Testing power-flow convergence problems due to long line lengths and unbalanced feeders
37 Node	5.50	4.8	Testing algorithms for uncommon configurations
4 Node	1.30	12.47	Analysis of available three-phase transformer connections, of step-up (24.9kV) or step-down (4.16 kV) operations and balanced/unbalanced loads
NEV	1.82	12.47	Load modeling studies
8500 Node	170.00	12.47	Testing of algorithms on realistic large-scale reference systems
CTF	81.67	12.47/ 24.90	Software testing issues
342 Node	15.20	13.2	Evaluation of algorithms in non-radial distribution networks distributed energy resources (DER) studies planning analysis
European LV	1.43	0.416	Studies of low-voltage feeders common in Europe and their mid- to long-term dynamic behavior

Table 2.1: List of IEEE test feeders [13]

Comprehensive Test Feeder (CTF): The CTF feeder was created essentially for the purpose of validating the models of all distribution network components like transformers and regulators. Additionally, it is designed to evaluate the convergence characteristics of various switching schemes. As a result, this feeder contains the majority of the network's components, including voltage regulators, underground cables, overhead lines, centre-tapped transformers, induction machines, switches, capacitor banks, distributed and spot loads, and transformer substations. Due to the incorporated switching devices, a diverse range of network configurations is possible. As a result, the CTF feeder model might be regarded one of the most extensive network models available [13, 53].

Neutral Earth Voltage Feeder (NEV): The NEV test feeder is primarily designed to address the problem of neutral to earth voltage. This difficulty develops when an electric current travels through a neutral conductor in the same direction as in the phase conductors. This test feeder can be used for distribution system analysis, including all features of steady-state frequency-domain analysis (except for lightning analysis) found on distribution systems [13, 53].

8500 Test feeder: This test feeder is a radial distribution feeder modelled based on a real-world distribution circuit in the United States of America. As the name suggests, it has 8500 nodes and consists of medium and low voltage sections. The test case is intended to serve as a benchmark for researchers interested in determining if the algorithms they have created will scale perform well on massive systems. This network can be used for distribution system analysis like power flow solutions and renewable energy generation [13, 53].

342 node Test feeder : The 342 node low-voltage network feeder is an unbalanced and heavily meshed urban system of moderate size. This network also includes unbalanced network components. It incorporates numerous elements present in a distribution network, including the following: Several primary feeders at 13.2kV, network protectors, a 120/208V network section, and numerous 277/480V spot feeders [13, 53].

LVNT: Test networks presented above are based on North American version of power systems. Low-voltage, radial, and meshed distribution systems are also common outside North America. This network is based on benchmark European-style distribution network. It operates at 4.16KV [13, 53].

European Low-Voltage Distribution Benchmark Network : CIGRE Task Force TF C6.04.02 has developed benchmark test systems for high voltage, medium voltage, and low voltage networks that address difficulties associated with DER integration. Both North American (60Hz) and European style (50Hz) networks are created for each benchmark system [1]. However, due to the study's primary focus on LV distribution networks, the CIGRE-developed European-style LV benchmark network will be discussed.

These benchmark networks can be either used for steady-state or transient analysis .

The benchmark network consists of 37 nodes in total as illustrated in figure 2.1 and is modelled after a real-world European low voltage network . As a benchmark network, it preserves significant technical properties while simultaneously reducing the complexity of the network and enabling flexibility for the integration of Distribution Energy Sources. The distribution system can be classified into three segments: residential, commercial, and industrial. Load profiles differ depending on the subnetwork. Any combination of these subnetworks can be utilized for the studies. A single load is connected to the industrial feeder, whereas eight and six loads are connected to the commercial and residential feeders. The loads in a subnetwork are either connected by the overhead lines or undergrounds cables. The low voltage distribution networks operate at the primary voltage 0f 0.4KV.
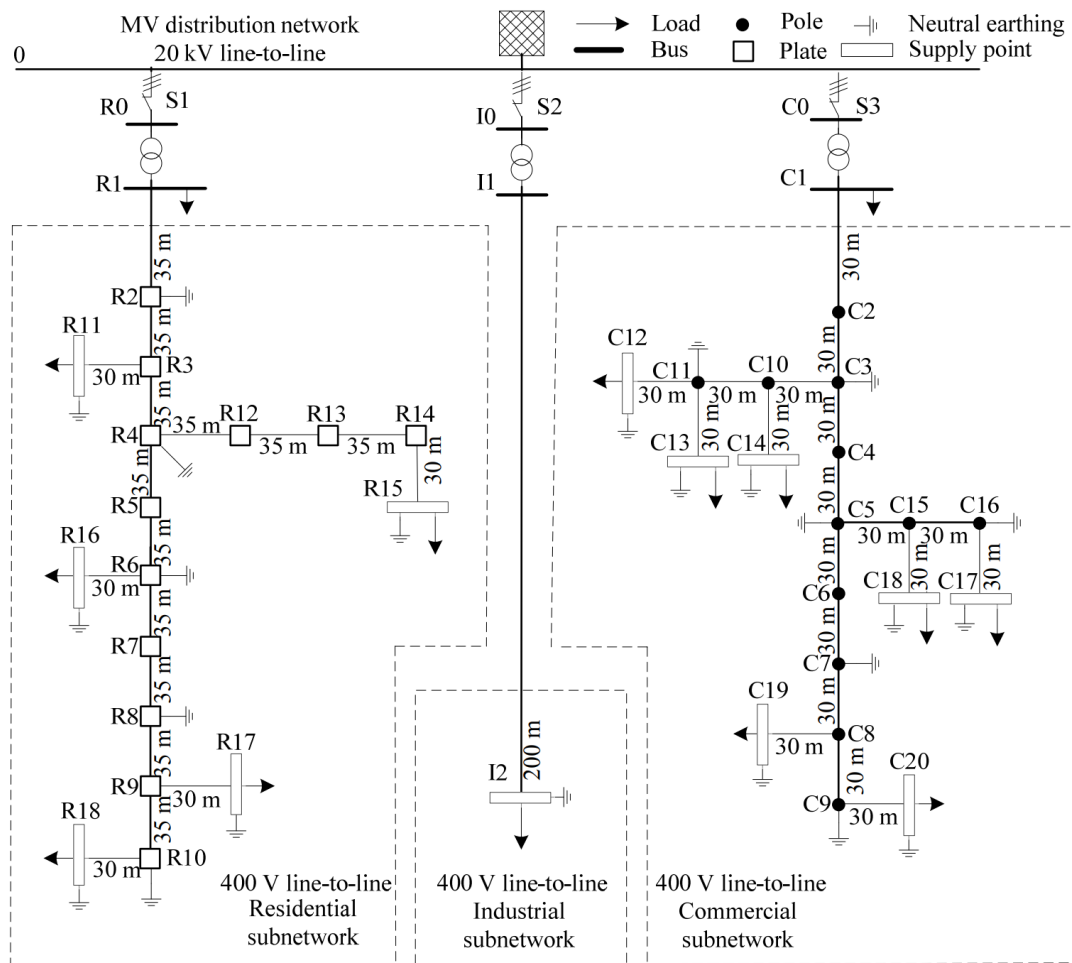
Figure 2.1: Line diagram of the European low voltage distribution network developed by CIGRE [1]

IEEE and CIGRE are the well know electrical organizations that publish industry-standard benchmark test systems. Additionally, other research institutes and laboratories, such as the Pacific Northwest National Laboratory (PNNL) [54, 55], the Electric Power Research Institute (EPRI) [56], and the Pacific Gas and Electric Company (PGE), among others, are also involved in the development of test networks. For instance, PNNL produced 24 prototypical feeder models based on data collected from 575 real radial distribution feeders located throughout the United States [13, 55]. These feeders are categorized according to temperature and climate regions. Moreover, several test feeders have also been developed by independent researchers and research groups. A few of the examples include -

- Agent-based distribution test feeders,

- European representative synthetic distribution test Networks [57],

- European non-synthetic low-voltage test network

The ABDTF developed by Pedram Jahangir and his team is modelled based on the residential feeders in the Iowa state in the US [58]. It is one of the most precise representations of any distribution system, including overhead lines, underground cables, switches, cables, and transformers. The network connects 1370 residences (loads). The network also features smart grid technologies like PVs, plug-in electric vehicles, and smart air conditioning. The network is primarily used to investigate the effects of smart grid designs on a distribution feeder. The ENSLVTN developed in Arpan Koirala is based on data from a small European town's distribution feeders [59]. This is an enormous network with 10290 buses, 8087 loads, and 30 distribution transformers. The network operates at a voltage of 416V. The network is designed to support researchers in carrying out studies on smart grid-enabled technologies such as DERs, EVs, among others.

2.3. CRITERIA FOR THE SELECTION OF TEST SYSTEM

Until now, different test networks have been extensively described in the prior section. However, not all networks are suitable for all types of research and analysis. As a result, an appropriate network must be chosen based on the project's requirements. Below is a list of the criteria used to select the intended test network.

- The network must be based on a real European (50Hz), low voltage (400V) distribution system.

- The network must be diverse in nature, flexible and should support DERs.

- The accurate information on all the network components (transformers, loads, lines and cables) must be available in the literature.

Following a thorough assessment, the CIGRE-developed European low-voltage distribution benchmark network was chosen for further research. The CIGRE LV network is developed in the European version operating at 50Hz and 400V. All the IEEE test systems except the last system in the table are based on the North American version of the distribution system. CIGRE network is relatively small compared to other European test systems (LVNT by IEEE and ENSLVTN). It has fewer nodes and supports the integration of various DERs. This network has, after all, been developed particularly to carry out DER integration studies. To reduce the computation time, as a proof of concept of the employed algorithms, this network has been considered as to conduct penetration studies. A vast amount of information on each element of the CIGRE LV network has been made available in the document Task Force TF C6.04.02 [1]. The detailed information on the selected network is given in appendix.

2.4. MPPT

This section provides a quick overview of maximum power point tracker(MPPT), describing what they are and how they work. Subsequently, several MPPT techniques will be discussed, and one will be chosen for this thesis.

2.4.1. NECESSITY OF MPPT

Consider an ideal solar cell whose terminals are connected to a resistive load R, as displayed in the figure 2.2. In the same figure, the I-V characteristics of both the solar cell and the load are illustrated. The I-V curve of a resistive load is just a straight line (also called a load line) with a slope of $1/R$. The operating point is defined as the point at which both the curves intersect as shown in the figure 2.2. The power drawn by the load at this point can be given by, $p = vi$. Depending on the size and type of load, the operating point is not always at MPP at which the PV cell generates maximum power. Moreover, the load varies majority of the time, and the maximum power-point also varies with the irradiation conditions and temperature of the solar cell. Therefore, this mandates the installation of a maximum power point tracker (MPPT), which continuously monitors the maximum power point under all scenarios and forces the PV cell to operate at its MPP. Absence of MPPTs could result in low power output from the PV cells.
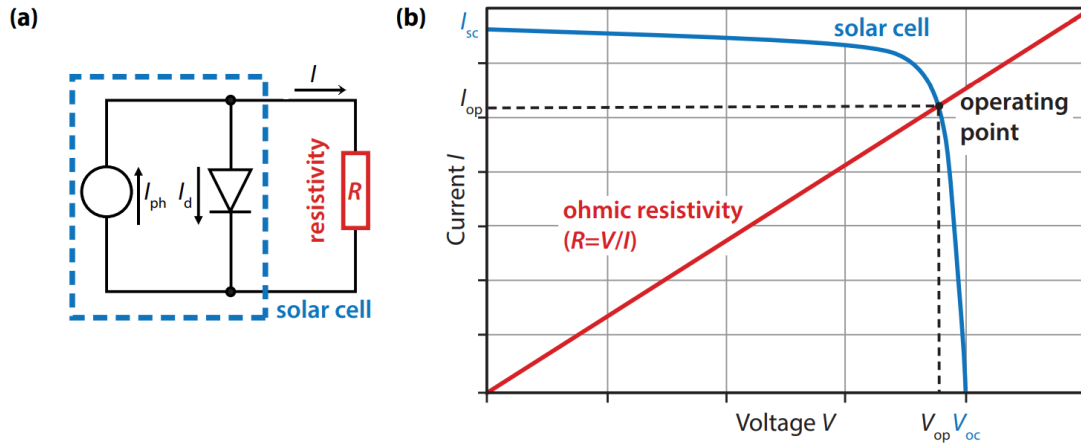
Figure 2.2: a) Ideal PV cell connected to a resistive load [2]   b) The operating point of the PV cell [2]
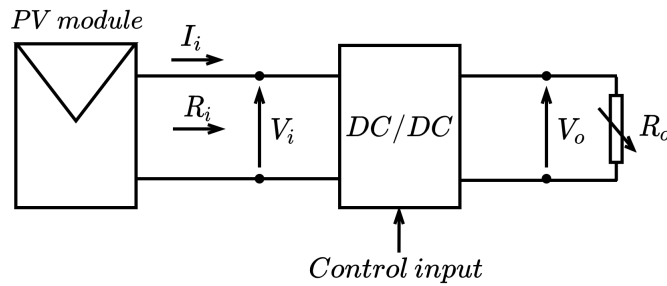
Figure 2.3: MPPT concept

2.4.2. WORKING OF MPP TRACKERS

MPPT is a control system that works in conjuncture with the DC/DC or DC/AC converters based on the PV system topology. Consider a simple PV system portrayed in the figure 2.3. The PV module is connected to a variable load R_0 (DC load) via a DC-DC converter. The input to the converter are the voltage and current from the PV module, and R_i is the terminal resistance viewed from the PV module side. The MPPT control works by giving out control signals to the DC-DC converter such that the input impedance R_i is regulated so that the load line defined by R_i always intersects the MPP on the I-V curves of the PV cell/module. This ensures optimal operation of the PV system, irrespective of the load variations. In this thesis, the boost converter is employed as a DC-DC converter, as represented in the figure 2.4, because it is required to boost the voltage to a level required by the inverter. The voltage and current flowing through the inductor depend on the duty ratio D and the switching cycle of the switch S. As seen in the figure 2.5, the current through the inductor I_L has a triangular waveform while the voltage drop has a square wave shape. The average voltage across the inductor is zero when it is in its steady condition (as determined by flux balance), and the average current flowing through the capacitor is zero. (charge balance). Under these conditions, the voltage and current relationships between the input and output of the converter can be expressed as,

$$V_0 = V_i \cdot \left(\frac{1}{1-D} \right) \tag{2.4.1}$$

$$I_0 = I_i \cdot (1-D) \tag{2.4.2}$$

Dividing the above equations,

$$R_0 = \frac{V_0}{i_0} = \frac{V_i}{I_i} \cdot \left(\frac{1}{(1-D)^2} \right) = \frac{R_i}{(1-D)^2} \tag{2.4.3}$$

or,

$$R_i = R_0 \cdot (1-D^2) \tag{2.4.4}$$
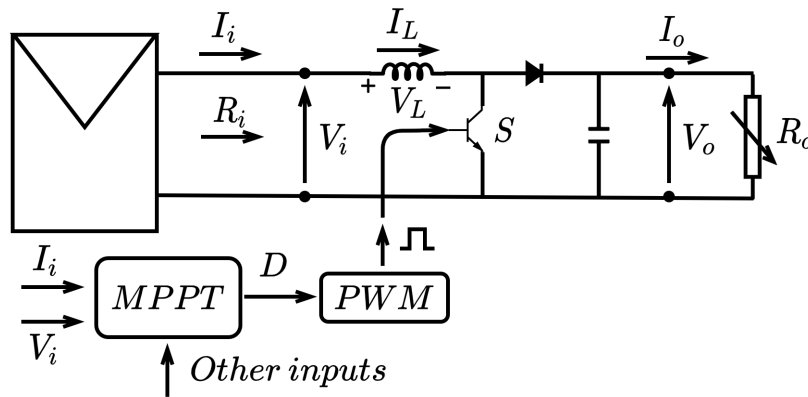
Figure 2.4: Connection of boost converter to the PV module
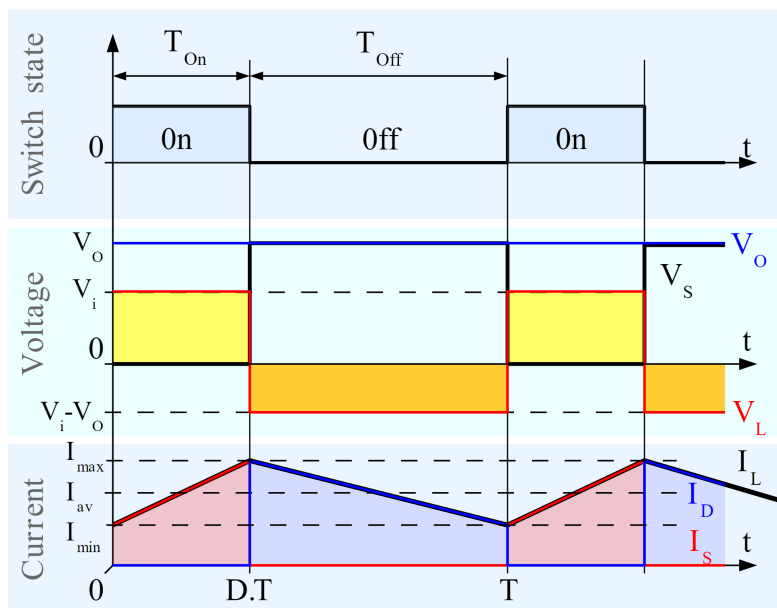
Figure 2.5: Waveforms of current through the inductor and voltage across the inductor

The Eq. (2.4.4) [3] establishes a critical link between the duty ratio and the boost converter's input terminal resistance R_i. If the load R_0 changes, the MPPT controller adjusts the duty ratio so that the PV modules always see an impedance with a load line that intersects the MPP point perfectly. As a result, the modules are always utilized to their full potential. The general topology of the MPPT control scheme is also presented in the figure 2.4. To begin with, the current and the voltage are monitored at the PV module's terminals. They are then processed using a variety of MPPT methods (described in the following section), and reference variables are created. A PI controller works on the error signal obtained from the difference between the reference and feedback variables and outputs a signal that is passed through the pulse width modulator to generate gate pulses for the boost converter.

2.4.3. VARIOUS MPPT CONTROL TECHNIQUES

There are ample amount of MPPT techniques published in the literature. These techniques can be categorised into direct and indirect methods. Through the use of empirical data or mathematical equations, indirect methodologies track the maximum powerpoint, whereas the direct methods make use of I-V measurements for optimal tracking. The following list summarises the most standard and fundamental MPPT techniques used in the literature.

- Constant voltage [60]

- open-circuit voltage [61]

- short circuit pulse [62]

- Perturb and observe [63]

- Incremental conductance [64]

- Temperature method [65]

The constant voltage method uses the specifications of the PV array, like V_{mpp} to operate. The V_{mpp} at STC is hardcoded in the algorithm. It measures the current and the voltage of the modules and tweaks that towards the hardcoded V_{mpp}. It doesn't take into consideration the irradiance and temperature changes. So this method does not give accurate optimal power. To overcome such disadvantages, the open voltage method measures the open-circuit voltage and assumes that Vmpp always lies between 70% to 80% of the measured V_{oc}. To monitor the V_{oc} one of the cells is disconnected and hence no power will be delivered from that cell. The short circuit current pulse technique is analogous to open voltage technique but here instead of V_{oc}, I_{sc} is measured and I_{mpp} is considered to be around 92% of I_{sc}. It shares the same advantages and disadvantages as the previous method. Perturb and observe measure follows the PV curve and at every step the power is calculated and compared with the value obtained in previous step. If the control sees an increase in the power, the next perturbation will be on the positive side (in the increasing direction of voltage) and vice versa. This method tends to fluctuate around the MPP since the algorithm is not aware of the MPP. Temperature methods make use of the ambient temperature to calculate the V_{oc} and then similar to open voltage and short circuit pulse method V_{mpp} and I_{mpp} are calculated.

INCREMENTAL CONDUCTANCE:

The slope of the P-V curve at the maximum powerpoint is zero. To the left of the MPPP, the slope is positive and to the right it is negative. In the incremental conductance method, the transition in the slope of the P-V curve is used for tracking the MPP. The power from the modules can be calculates as $P = vi$. Upon derivating with v,

$$\frac{dp}{dv} = i + v \cdot \frac{di}{dv} \tag{2.4.5}$$

At maximum power point, $\frac{dp}{dv} = 0$, hence equation transforms into,

$$\frac{di}{dv}\bigg|_{P_{Mpp}} = -\frac{i}{v} \tag{2.4.6}$$

From the equation (2.4.5), it can be said that

$$\frac{di}{dv}\bigg|_{P<P_{Mpp}} > -\frac{i}{v} \tag{2.4.7}$$

$$\frac{di}{dv}\bigg|_{P>P_{Mpp}} < -\frac{i}{v} \tag{2.4.8}$$

The logic developed from the Eq. (2.4.6), (2.4.7) and (2.4.8) can be used to identify where the MPP lies. Thus, if $\frac{di}{dv} + \frac{i}{v} = \rho$ is exceeds zero, the operating point (OP) is located to the left of the MPP. If it equals zero, the OP is the same as the MPP; if it is below zero, the OP is to the right of the MPP. Now, the ρ can be used to find the duty cycle which determines the terminal resistance (Eq. (2.4.4)) as seen by the modules. Hence, the load line will be adjusted in such a way that it passes through the MPP. The following flowchart (figure 2.6) summarises the incremental conductance algorithm. The flow chart shown corresponds to positive ΔD, for negative ΔD the signs are reversed. MPPT model designed in [66] has been used in this thesis, which follows similar algorithm discussed above.
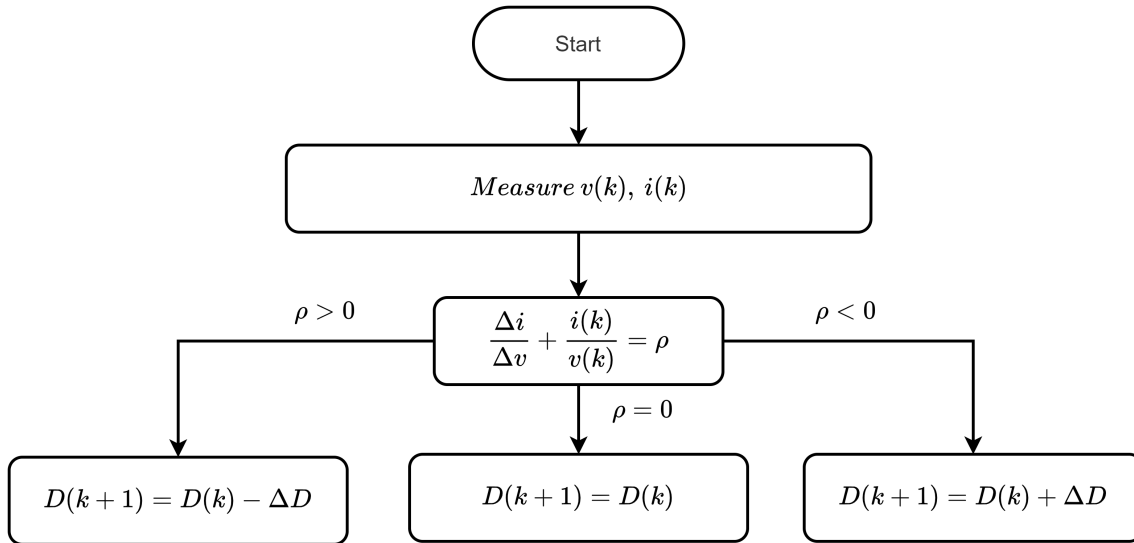
Figure 2.6: Flowchart of Incremental Conductance MPPT algorithm

2.5. INVERTER TOPOLOGY

Voltage source inverters can be categorized into two-level and multi-level (three or more levels) inverters. The 'level' of the inverter refers to the number of voltage levels generated at the AC terminal measured with respect to the midpoint voltage of two split DC link capacitors (in the literature, researchers also considered negative terminal as the reference).
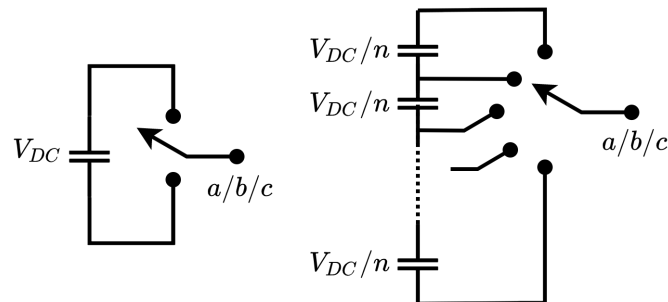
Figure 2.7: Schematic circuit diagrams of a Two level and a multilevel inverter

If the total DC link voltage is V_{DC}, a two-level three-phase inverter could generate either $+V_{DC}/2$ or $-V_{DC}/2$ per leg/phase. In contrast, a three-level (a multi-level inverter), three-phase inverter generates $+V_{DC}/2$, 0, $-V_{DC}/2$ per phase measured with respect to the DC-link midpoint voltage. The advantages of a three-level inverter include-

• Better output AC waveform quality - Since more voltage levels are available at the output, it is possible to follow the sinusoidal waveform much better. This eventually could reduce the size of the AC filter.

• Higher voltage handling capability - For a given voltage rating of the switches, a multi-level inverter can handle higher DC-link voltage compared to a two-level inverter. This is possible because the blocking voltage can be shared by the multiple switches in a multi-level inverter

• Lower switching losses- At higher frequencies, the switching losses incurred in a multi-level inverter are lower because oftentimes they are switched at lower voltage levels. In contrast, two-level inverters are always switched at either $+V_{DC}/2$ or $-V_{DC}/2$.

The disadvantages of multilevel inverters are more number of components, complex controlling techniques and unbalanced DC link voltages. The multilevel inverter comes in different sizes and types such
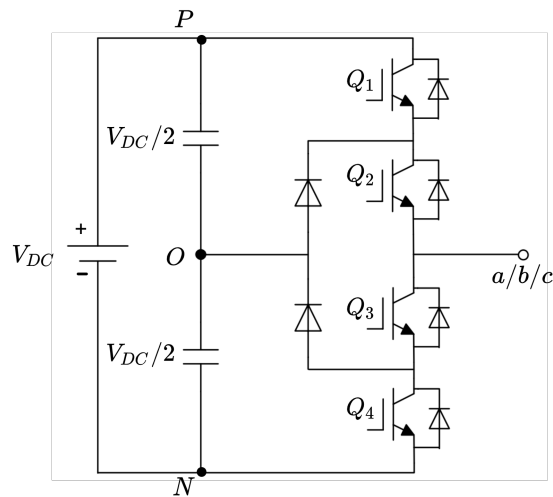
Figure 2.8: Schematic representation of one of the legs of a three-phase three-level inverter

Q_1	Q_2	Q_3	Q_4	$V_{(a/b/c)O}$
1	1	0	0	$V_{DC}/2$
0	1	1	0	0
0	0	1	1	$-V_{DC}/2$

Table 2.2: Switching logic for one of the legs of a three phase three level inverter

as three/four/five-level diode clamped multi-level inverter, three/four-level flying capacitor inverters, modular multilevel cascade inverters [3]. In the current study, a three-level diode clamped inverter has been chosen. The figure 2.8 shows a single leg circuit configuration of a three-level inverter and the corresponding switching logic is given in the table 2.2. The DC link voltage is divided into two equal parts by the two series capacitor. The terminals P, O, N corresponds to the positive, midpoint and negative DC bus terminals respectively. The a,b,c phase wires can be connected to any of the DC-bus terminals according to the control logic. As discussed earlier it can produce three voltage levels and when compared to a two-level inverter it can handle double the DC voltage with the same voltage rating of the active switches.

2.6. PWM TECHNIQUES

Typically, the controller in a power electronic converter defines the reference voltage that must be generated to meet the control requirements. The technique of generating this reference voltage on average throughout a specific interval, by performing a mixture of switching commutations is known as modulation [3]. This is a critical operation in a power electronic converter since the modulation technique applied significantly influences the resultant waveform quality and the performance of the converter.

In order to achieve objectives such as minimal harmonic content in output waveforms and power losses, each power converter configuration requires a distinct modulation approach depending upon the application. The complexity of the modulation schemes often grows as the number of power electronic switches increases. This is evident for the multilevel inverter family, in which the number of devices can be incredibly large in comparison to traditional two-level inverters.

In several settings, multilevel inverter modulation methods began as adaptations and enhancements of well known two-level inverter modulation methods. One such method is **In Phase Level-Shifted Sine Pulse Width** modulation technique which is the direct extension of sine PWM. In this method, for an N level inverter, the N-1 triangular wave carriers are distributed evenly across the voltage range of the multi-level inverter. Two triangular wave carriers, for example, are required for a three-level neutral
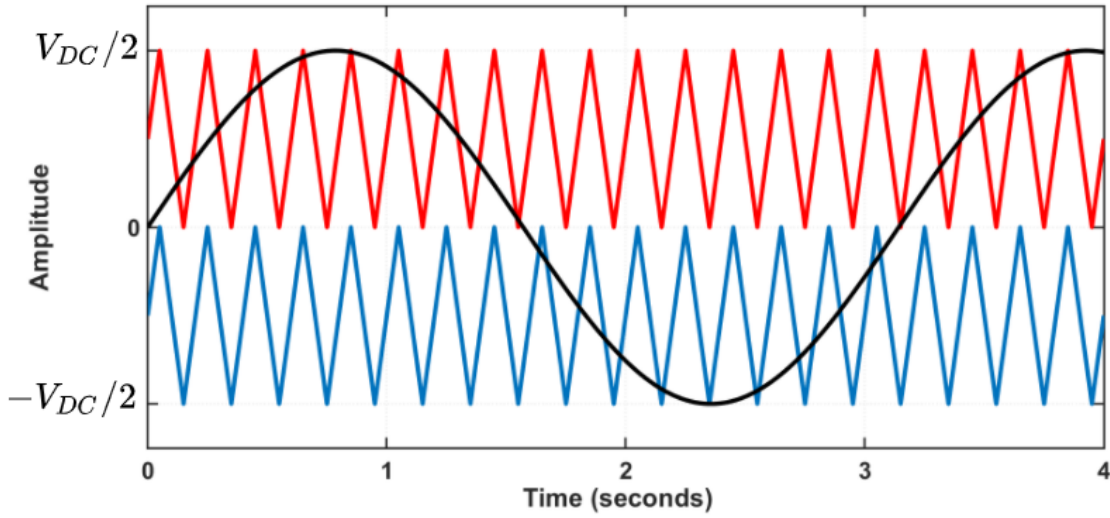
Figure 2.9: Pulse width modulation for a three level inverter

point clamped inverter. With a DC bus voltage equal to V_{DC}. The first carrier is in the range of zero to $+V_{DC}/2$, whereas the second carrier is in the range of zero to $-V_{DC}/2$ as shown in the figure [?]. The black curve is the modulating signal and the red and blue curves are carrier signals. To get the desired pulses the modulating (reference) voltage waveform is compared with the two carrier waves according to the following logic.

$$S_{y_1} = \begin{cases} 1 & \text{if } m_y \geq V_{cp} \\ 0 & \text{if } m_y < V_{cp} \end{cases} \tag{2.6.1}$$

$$S_{y_3} = \bar{S}_{y_1} \tag{2.6.2}$$

$$S_{y_4} = \begin{cases} 1 & \text{if } m_y < V_{cn} \\ 0 & \text{if } m_y \geq V_{cn} \end{cases} \tag{2.6.3}$$

$$S_{y_2} = \bar{S}_{y_4} \tag{2.6.4}$$

where, S are the gate signals for various switches (Q_1, Q_2, Q_3, Q_4) in a leg, $y \, \epsilon \, a$, b, c corresponds to the three phases, m_y are the modulating signals of all the phases and V_{cp} and V_{cn} are the two triangular carrier waves. Gate signals $S_{(y)_1}$ and $S_{(y)_3}$, and $S_{(y)_2}$ and $S_{(y)_4}$ are the complementary witching pairs (can also be viewed from the table). The modulating reference voltage waves are generated by the inverter control.

IPLS-PWM is one of the most straightforward and easily comprehensible techniques which is widely used in studies for three-level NPC inverters. There are other PWM techniques such as phase-shifted-PWM, where the phase of the carrier signals is different and hybrid PWM techniques which comprise the characteristics of both LS-PWM and PS-PWM [3]. However, they are more suited for higher-level inverters and CHB inverters [3].

3

MODELLING, DESIGN AND CONTROL

The previous chapter explored several distribution grids in detail, including the selected low voltage distribution network. This chapter begins with a discussion of the chosen network's modelling, followed by the presentation of the resulting voltage profiles. The following sections describe in depth the modelling and design of several pv system components, including photovoltaic modules, inverters, MPPT, boost converters, and LC filters, as well as irradiance calculations.

After that, a brief description of the control technique used in this thesis is provided. This section begins by discussing the grid connection principle. Then, the theory of DQ transformations and the per-unit system are discussed. Later in the chapter, the outer voltage control loop is explained in detail, and the plant transfer function is deduced. Similarly, the inner control is explained, and the plant model is generated from the appropriate dynamic equation on the AC side of the PV system. Finally, the entire control loop is presented, which comprises both the inner and outer control loops.

3.1. GRID MODELLING

The distribution network illustrated in the figure 3.1 has been modelled in Simulink. The network consists of 37 nodes and has been categorized into residential, industrial, and Commercial sub-networks. The loads are represented with arrows in the network model. The information regarding network is given in the appendix.

The normalized load profiles shown in the figure are taken from the CIGRE document. Each subnetwork has a different load profile, as shown in the figure 3.2. The load profiles correspond to the power absorbed by the loads over 24 hours in minute resolution. The shapes of the load profiles have been extracted from the CIGRE document using a web digitizer. The loads connected to a particular subnetwork follow an identical load profile but has different peak load consumption. For example, the load connected to the buses R15 and R16 of the residential subnetwork has the same load profile over a day, but the power they consume at a particular instant is different. A similar explanation can be given to the loads connected to the industrial and commercial subnetworks as well. The peak power consumption of every load is given in the table A.11 in appendix. The loads connected to the buses R1 and C1 are comparatively higher because they represent the cumulative loads from the other feeders connected to the transformer. Also, all the loads are operated at unity power factor.
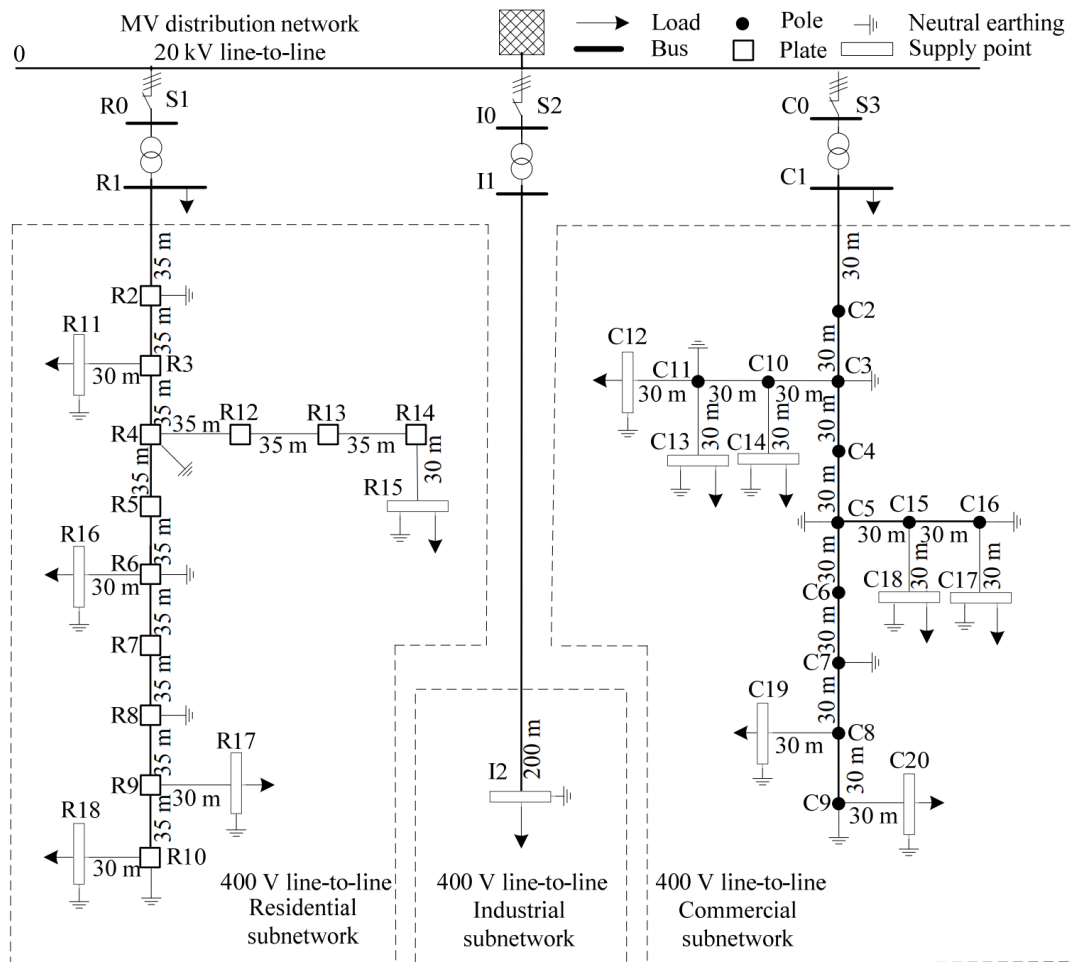
Figure 3.1: Line diagram of the European low voltage distribution network developed by CIGRE
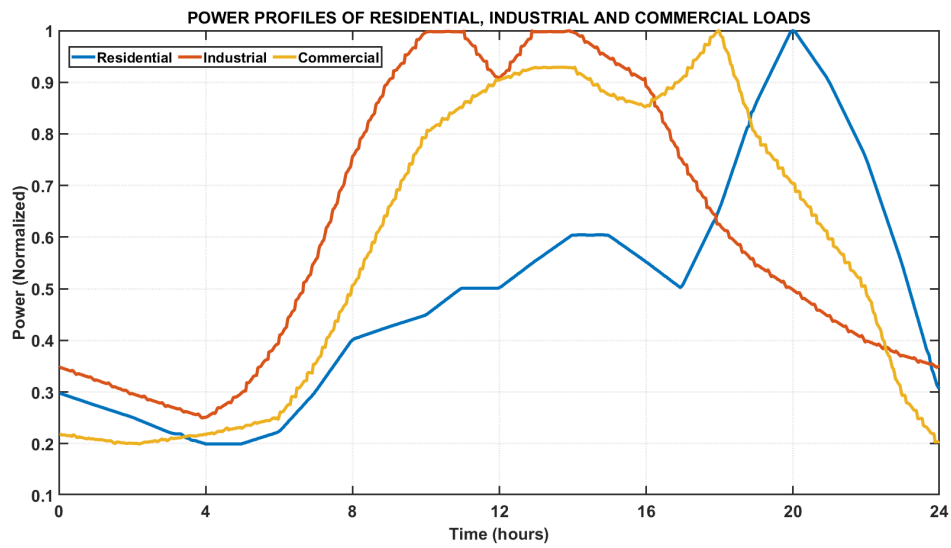
Figure 3.2: Load profiles of the residential,industrial and commercial subnetworks

3.2. Overview of the PV system components/ General arrangement of PV system

The PV systems' nominal power can range from hundreds of watts (Rooftop PV systems) to thousands of gigawatts (Large scale PV farm) depending on the requirement. Likewise, the PV system configuration varies according to their nominal power. However, regardless of its rating, the general structure of a PV system can be loosely explained. The general layout of a PV system is illustrated in the figure 3.3, where few components might be discarded based on the application (more on this later). The PV system as a whole can be segmented into three sections.

- DC

- AC

- Grid
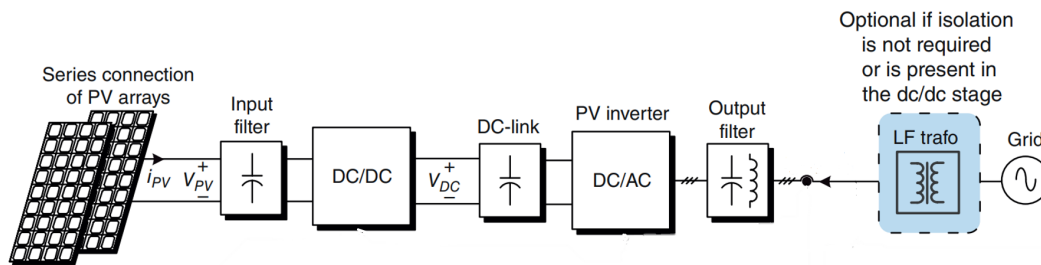
Figure 3.3: Overview of the PV system components [3]

The first section, referred to as the DC side, is composed of photovoltaic modules, a DC/DC converter with an MPPT controller, and a DC link capacitor. Solar photovoltaic modules capture solar energy and convert it to electricity. The panels are connected in a series or parallel configuration depending on the required voltage level. Generally, a boost Converter is utilised as a DC/DC converter in low power rating PV systems to increase the voltage to the optimal level for the inverter. For example, for a three-phase system, the voltage has to be boosted higher than the peak value of the phase to neutral voltage, depending upon the modulation index of the pulse width modulation method used. The DC/DC converter functions in conjunction with the MPPT controller. The MPPT ensures that the photovoltaic system is constantly operating at maximum powerpoint, producing the highest amount of power that the PV modules can generate under given irradiation conditions. Following that, the DC link capacitor filters out any ripple component present in the DC/DC converter's output. Additionally, it serves as a DC source for the subsequent system.

The AC side of the system comprises of inverter and an LC filter. The inverter converts DC components into AC components such that the output can be connected to the grid or AC loads. The AC output from the inverter contains higher harmonic content. The AC filter made up of inductors and capacitors filter out the harmonic content and delivers pure(almost) sine and cosine waves. On the grid side, the AC loads, grid and transformer (optional) are present. Depending on the amount of solar energy generated, a portion of the inverter's output power is transferred to the AC loads connected to the PV system, while the remainder is pumped into the grid (for the grid-connected PV system). Certain national rules mandate galvanic isolation in photovoltaic systems to avoid common mode voltage and curent. Therefore, it must be present at the DC/DC converter or via a transformer at the grid side.

3.3. Irradiance

Irradiance is defined as the power received from the sun, across all the wavelengths, per unit area. It determines the total energy falling on the PV modules in a particular interval of time. It is an essential parameter in energy yield calculations. Irradiance depends on the location, time and weather conditions.
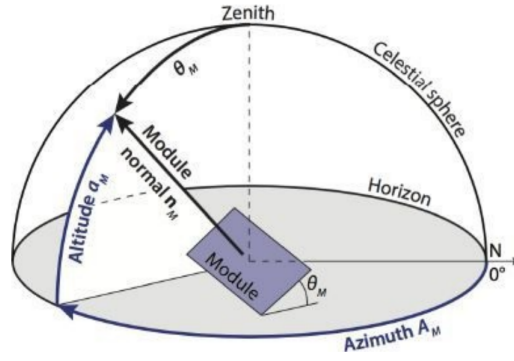
Figure 3.4: Orientation of a PV module in horizontal coordinate system [2]

The global irradiance from the sun can be defined as the sum of the diffuse and the direct components.

$$G_{global} = G_{diffuse} + G_{direct}$$

The above equation can also be written as

$$GHI = DHI + DNI\cos(\vartheta_z) \tag{3.3.1}$$

where GHI is Global horizontal irradiance, DHI is diffuse horizontal irradiance, and DNI is direct normal irradiance and ϑ_z is the angle between Zenith and sun position. GHI, DHI and DNI are measured using special hardware such as a pyranometer and pyrheliometer. Generally, the PV modules are not placed horizontally on the ground but rather tilted to increase the irradiance on the surface of the module. In that case, the irradiance falling on the modules can be divided into three components - Direct, Normal and albedo, as given in the following equation.

$$G_{Module} = G_{Direct} + G_{Diffuse} + G_{Albedo} \tag{3.3.2}$$

- Direct Irradiance (G_{Direct}) - It is the component that is directly incident on the PV module without suffering any reflections or scattering from the atmosphere and ground.

- Diffuse Irradiance ($G_{Diffuse}$) -This component is the amount of light that hits the module's surface after being scattered by the molecules in the atmosphere. Diffuse irradiance is incident on the PV modules from all the possible directions.

- Albedo (G_{Albedo}) - The albedo is the part of the irradiance that reaches the modules after reflection by the ground or neighbouring objects. This component is highly dependent on the type and nature of the surface on which PV modules are installed.

Consider a PV module tilted with respect to the ground at an angle theta, as shown in the figure 3.4. The position of the PV module with respect to its normal vector can be identified in a celestial sphere by defining two coordinates in the horizontal coordinate system. The first coordinate is the azimuth of the module, which is the angle between the true North and the normal of the module projected onto the horizontal plane. The second coordinate is the altitude of the module, which is the complementary angle of the module's tilt angle (90 - theta). To calculate the total irradiance impending on the module, the angle of incidence first needs to be calculated. It is defined as the angle between the module normal and the incident direction of the sunlight [2], as shown in the figure 3.5. The angle of incidence can be calculated from the Eq. (3.3.3).

$$AOI = \cos^{-1}\left[\cos(a_M)\cos(a_s)\cos(A_M - A_S) + \sin(a_M)\sin(a_s)\right] \tag{3.3.3}$$

It can be seen from the equation that AOI is the function module's altitude (a_m), azimuth (A_m) and sun's position (azimuth (A_s) and altitude (a_s) of the sun) in the celestial sphere.
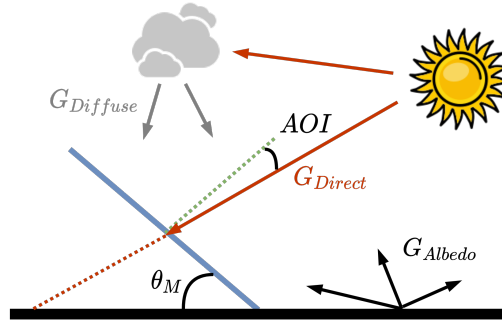
Figure 3.5: Angle of incidence

The direct component of the irradiance can be calculated using the Eq. (3.3.4), It can be seen that the direct irradiance is proportional to the direct normal incidence (DNI) and the cosine of AOI.

$$G_{\text{Direct}} = DNI \cdot \cos(\text{AOI}) \tag{3.3.4}$$

The calculation of diffuse component is not as straightforward as the calculation of direct component. In general, the diffuse irradiance is a function of DHI, AOI and sky view factor (SVF). SVF depends on the tilting of the module and is calculated by $SVF = \frac{1+\cos\theta_M}{2}$. SVF represents the portion of the sky seen by the PV modules when they are tilted at some angle. There are ample sky models available in the literature to calculate diffuse irradiance. Each model varies in the complexity and accuracy in the calculation of diffuse irradiance. A few of the sky models are -

- Isotropic sky model : $G_{\text{diffuse}} = SVF \cdot DHI$

- Sandia model: $G_{diffuse} = SVF \cdot DHI + f(GHI)$

- Hay and Davies: $G_{diffuse} = DHI \cdot f(SVF, AOI)$

- Riendl: $G_{diffuse} = f(SVF, AOI, GHI)$

The albedo component of the irradiance can be approximated using the Eq. (3.3.5) where α represents the reflections from the ground and environment. Albedo is the characteristic of a material. The higher the albedo higher will be the reflections from the surface. For example, the albedo of ice is 0.6, whereas the albedo of the forest is around 0.1. The albedo can be measured using albedometer.

$$G_{\text{Albedo}} = GHI \cdot \alpha \cdot (1 - \text{SVF}) \tag{3.3.5}$$

In this thesis, the irradiance data (DNI, GHI, DHI, Azimuth and Altitude of the sun) is obtained from METEONORM [67] for the location- station Delft in the Netherlands. The corresponding coordinates are 52.00754636426495 latitude and 4.357110169027999 longitude. The resolution of data is in minutes corresponding to a sunny day. The sky model used to calculate the diffuse component of the incident irradiance is the isotropic model. The total irradiance on the surface of the modules can be calculated by the equation

$$G_{Total} = DNI \cdot \cos(\text{AOI}) + SVF \cdot DHI + GHI \cdot \alpha \cdot (1 - \text{SVF}) \tag{3.3.6}$$

Module performance is highly dependent on the tilt angle and azimuth of the module, as they can affect the amount of direct and diffuse irradiance falling on the PV modules. Therefore, it is imperative to identify for which azimuth and tilt angle, the total irradiation on the module is maximum. The procedure involved in such optimization can be explained in the following steps-

1. The first step involves calculating the position (Azimuth and altitude) of the sun, with respect to the PV system, over a particular interval- a day in this case.

2. The second step involves setting the range for the tilt and azimuth angles. The considered range is $\theta_m \ \epsilon \ [0,90]$ & $A_m \ \epsilon \ [0,360]$

3. In the third step, the incident power is integrated over the interval (decided in the first step) for the full range of azimuth and tilt angles.

4. The output would be the energy yield over the specified interval for all the combinations of tilt and azimuth angles.
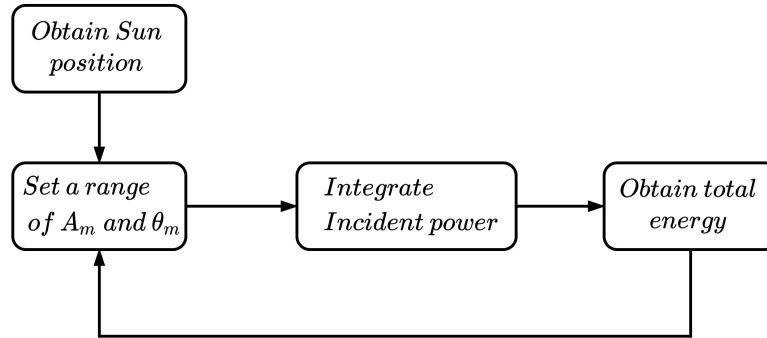
Figure 3.6: Steps involved in calculating optimal module configuration

The output results a contour plot, as shown in the figure 3.7. The horizontal axis represents the azimuth of the module, and the vertical axis represents the module's tilt. The contour plot is populated with the total amount of energy incident on the module over a day. The optimal tilt and azimuth are the ones for which the energy yield is the maximum. The optimal tilt is 16.2° and the optimal azimuth is 158.3° The figure 3.6 illustrates the steps in a flowchart. Using the optimal configuration of the PV modules, the irradiation plot over a day can be calculated using the Eq. (3.3.6). The corresponding irradiation plot is depicted in the figure 3.8.
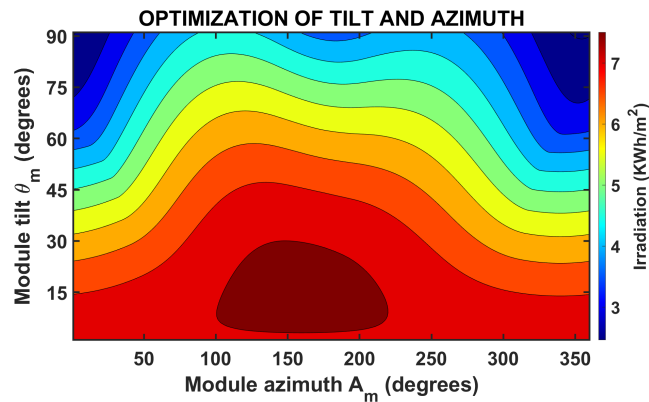
Figure 3.7: Contour plot depicting the total energy yield for all the tilt and azimuth combinations
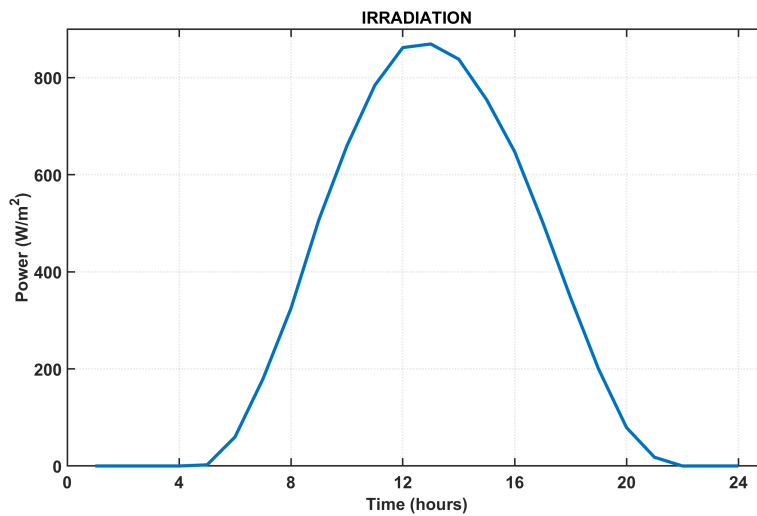
Figure 3.8: Irradiation falling on the PV module over a day

3.4. MODELLING OF PV CELL AND PV MODULE

Solar energy is omnipresent and can be harnessed using solar cells. Over the past decades extensive research has taken place to improve the efficiency of solar cells. Solar cells function based on the photovoltaic effect (called PV from now) i.e. generation of potential difference across the junction of absorbers due to incident irradiation. A single solar cell consists of an absorber which is fabricated on a substrate. The electrons in the absorber are excited to the higher energy levels upon the incident of solar radiation. The voids created due to the absence of electrons are called holes. They act as particles with positive charge. When the cell is connected to an external circuit, the electrons in the higher energy level flow through the external circuit, thus producing electrical energy. The working principle of a solar cell is shown in the figure 3.9. N-type and P-type semiconductors act as semipermeable membrane, where the generated electrons and holes are separated before they recombine and thus can pass through the external circuit. The efficiency of a solar cell is hugely dependent on the type of absorbers employed which depends on the material [2]. The maximum efficiency of different PV technologies ever recorded are mentioned in the appendix. The solar cells can be categorised in multiple ways depending upon their size, technology, flexibility, generation etc. However, in this report, the solar cells are classified into two technologies - thin film and wafer-based. They can be further categorised into flexible and non-flexible solar cells. The most common PV technologies used for rooftop PV applications are mono-crystalline silicon and poly-crystalline silicon whose maximum efficiencies ever recorded are 26.7% and 23.3% respectively. The I-V characteristics of an illuminated photovoltaic cell that performs like an ideal diode
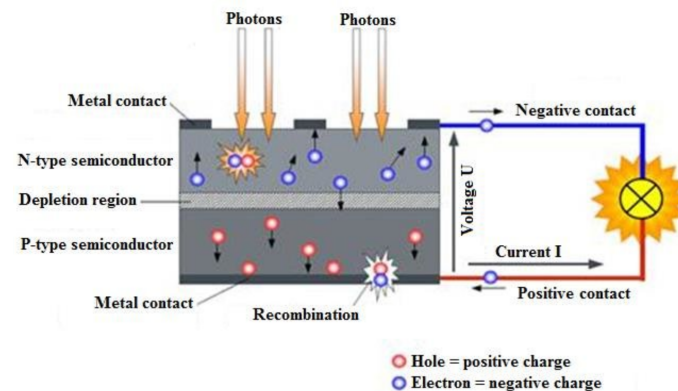
Figure 3.9: working principle of a solar cell [4]

can be characterised by a simple equivalent electric circuit consisting of a diode and a current source connected in parallel, as illustrated in the figure 3.10 . A diode is a physical representation of the development of a p-n junction. In actuality, a series resistance R_s and a shunt resistance R_p have an effect on the performance of a solar cell. The series resistance R_s represents the aggregate of a solar cell structural resistances. The junction's bulk resistance, the contact resistance between semiconductor and metal, and the electrodes' resistance contribute to the series resistance. Shunt resistance is caused by a parallel path for leakage current developed by local defects in the p-n junction and shunts near the PV cell's edges [2]. Hence, R_p strongly depends on the type of fabrication method employed to develop the solar cells. R_p has an effect on the slope of the I-V curve's initial section.
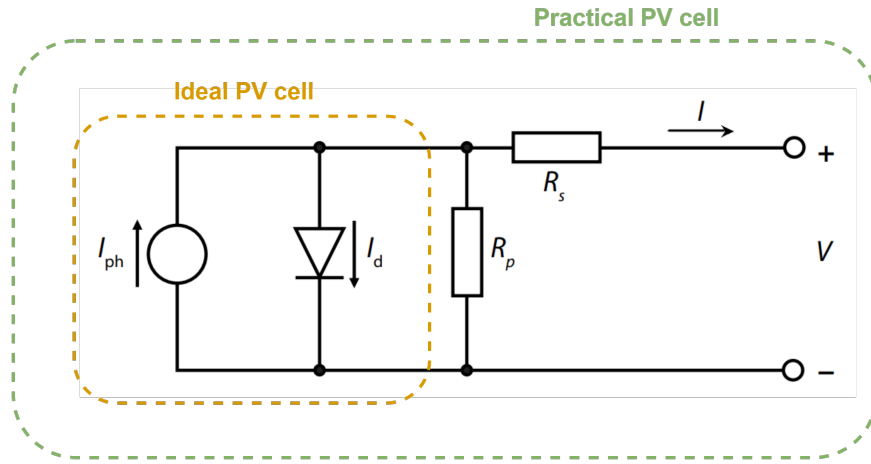
Figure 3.10: Equivalent circuit of an ideal and a practical solar cell

The mathematical expression governing the I-V characteristics of an ideal and practical solar cell are given in the Eq. 3.4.1 and 3.4.2 [2, 68, 69]. The resulting I vs V plot is illustrated in the figure 3.11

$$I = I_{ph} - I_0 \left\{ \exp\left[\frac{qV}{nk_B T} \right] - 1 \right\} \tag{3.4.1}$$

$$I = I_{ph} - I_0 \left\{ \exp\left[\frac{q(V - IR_s)}{nk_B T} \right] - 1 \right\} - \frac{V + IR_s}{R_p} \tag{3.4.2}$$

where,
I is the current flowing through the load
V is the voltage across the load
I_0 is the saturation current or dark current
R_s is the series resistance
R_p is the parallel resistance
n is the ideality factor
q is the charge of an electron
T is Temperature ($300k$)
K_B is the boltzman constant
I_{ph} is the photo-generated current
Saturation current or dark current is a material property. It is a measure of the degree of recombination occurring in a solar cell. Ideally, it must be kept as small as possible. I_0 largely depends on the doping of n-type and p-type semiconductors. Three crucial points can be drawn from the figure 3.11-

- Open circuit point (V_{oc},0)

- Short circuit point (0,I_{sc})

- Maximum power point (V_{MPP}, I_{MPP})
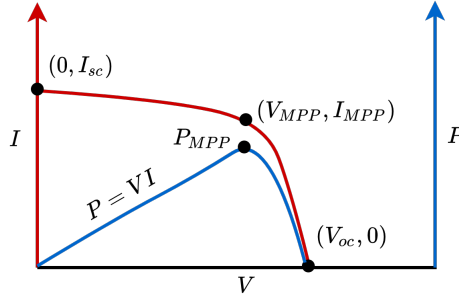
Figure 3.11: Charecterstic I-V curve of a PV cell

Both V_{oc} and I_{sc} can be calculated from ideal diode equivalent circuit Eq. (3.4.1). V_{oc} is obtained by taking $I = 0$ and I_{sc} can be derived by taking $V = 0$. The resulting equations are-

$$V_{oc} = \frac{k_B T}{q} \ln \left(\frac{I_{ph}}{I_0} + 1 \right) \tag{3.4.3}$$

$$I_{sc} = I_{ph} \tag{3.4.4}$$

The PV cell operates differently for different types/sizes of the loads connected to it. At open-circuit voltage (V_{oc}), no current flows through the load connected to it. It is equivalent to having an open circuit across the PV cell. V_{oc} is the maximum voltage a PV cell can support. The short circuit point occurs when the terminals of the solar cell are short-circuited. Thus, at this point, the voltage seen across the PV cell electrodes is zero. The corresponding current in the external circuit is called short circuit current (I_{sc}). It is the maximum current a solar cell can generate at a given Irradiance. I_{sc} depends on the incident photon flux and area of the PV cell. The output electrical power from a PV cell can be calculated as $P = VI$, where V and I are the output voltage and current. Thus obtained P-V curve is illustrated in the figure 3.11, where it can be observed that at a point called P_{MPP}, the power extracted from the PV cell is the maximum. The voltage and current corresponding to this point are denoted as V_{MPP} and I_{MPP}. Hence, to efficiently make use of a PV cell, the external circuit must be designed in such a way that the PV cell operates at MPP optimal point. The solar cell behaves as a current source before the MPP and acts as a voltage source after the MPP. When operating in the voltage source zone, the R_s has a greater impact, while the R_p has a bigger effect when working in the current source region.

To obtain credible I-V characteristics of a photovoltaic cell, measurements must be conducted under widely accepted industry-standard test conditions (STC). The STC conditions are-

- The total irradiance incident on a PV cell must be equal to 1000w/m2

- The incident photon flux should reflect that of AM 1.5 spectrum.

- PV cell's temperature should be maintained at 25°C

The solar cell efficiency is calculated by taking the ratio of maximum power produced and incident power. It is calculated at STC conditions at which the incident radiation (I_{in}) becomes 1000w/m2. The efficiency is given by,

$$\eta = \frac{P_{max}}{I_{in}} = \frac{J_{MPP} V_{MPP}}{I_{in}} \tag{3.4.5}$$

where J_{MPP} is the current density at MPP point. In summary, the peak power Pmax, the short-circuit current Isc, the open circuit voltage Voc, the maximum power point voltage (Vmpp), and current (Impp) are the primary metrics used to assess the performance of solar cells. As a result, these are the parameters (calculated at STC) that manufacturers include in the technical specifications of any photovoltaic module. For a PV modules, where the PV cells are connected in series and parallel combinations, the Eq. (3.4.2) [68] slightly changes into,

$$I = MI_{ph} - MI_0 \left\{ \exp \left[\frac{q(V - IR_s)}{Nnk_B T} \right] - 1 \right\} - \frac{MV + NIR_s}{NR_p} \tag{3.4.6}$$

where, M is the number of cells connected in parallel and N is the number of cells connected in series. In this work of thesis, the PV module developed by the company SunPower is used for modelling, whose specifications and model parameter are mentioned in the table 3.1-

Specifications	Value	The equivalent circuit parameters	Value
Rated maximum power P_{MPP} (W)	305	Photo-generated current I_{ph} (A)	6.0092
Open circuit voltage V_{oc} (V)	64	Saturation current I_0 (A)	6.3e-12
Short circuit current I_{sc} (A)	5.96	Diode ideality factor	1.1203
Voltage at maximum power point V_{MPP} (V)	54.7	Shunt resistance R_p (ohms)	269.5934
Current at maximum power point I_{MPP} (A)	5.58	Series resistance R_s (ohms)	0.37152
Cells per module (Ncell)	96		
Temperature coefficient of V_{oc}, α_V (%/deg.C)	-0.27269		
Temperature coefficient of I_{sc}, α_I (%/deg.C)	0.061745		

Table 3.1: List of PV module specifications and the equivalent circuit parameters

The equivalent circuit parameters are obtained from SIMULINK library and System Advisor Model (SAM) developed NREL [70, 71]. However, most of the time, manufacturers do not provide all the necessary data required to model a solar cell. Only the module specifications given in the table are made accessible. The equivalent circuit parameters like R_s, R_p, I_{ph}, I_0 and n are not available all the time and must be carefully selected by analysing the PV array characteristics and studying the literature. For, instance R_s and R_p can be calculated from I-V curves.

Oftentimes, PV modules do not operate at STC conditions. Irradiation varies with time and weather conditions, as stated in the previous section. Additionally, the temperature has a profound impact on a solar cell's performance [2]. A solar cell's temperature rises due to various factors, one of which is electron-hole pair recombination occurring at several sites within the semiconductor (not all recombination phenomena result in temperature increase). The temperature coefficients indicated in the table's 3.1 final two specifications dictate how V_{oc} or I_{sc} varies in response to a solar cell's temperature. The energy level of the electrons increases as the temperature of the solar cell increases, requiring less energy to transition from lower energy states to higher energy states. As a result of this, the semiconductor's bandgap narrows. Thus, a more significant number of electrons and holes will be able to reach the metal electrodes, resulting in an increase in output current. This accounts for Isc's positive temperature coefficient. The bandgap narrowing can be interpreted as a reduction in the open-circuit voltage V_{oc}. As a consequence, as the temperature rises, Voc lowers.

The photo-generated current I_{pv} of a photovoltaic cell has a linear relationship with the irradiation as per the following equation.

$$I_{ph} = \left(I_{ph,STC} + K_I \Delta T\right) \frac{G}{G_{STC}} \tag{3.4.7}$$

where,
$I_{ph,STC}$ is the photo generated current at STC conditions
$K_I = \frac{\alpha_I I_{ph,STC}}{100}$ (Another form of temperature coefficient)
$\Delta T = T - T_{STC}$ (Difference between actual temperature [K] and temperature [K] at STC)
G and G_{STC} are solar irradiance at non optimal conditions and STC ($1000 W/m^2$)

The diode saturation current also changes with temperature as given by the relation,

$$I_o = I_{o,STC} \left(\frac{T_{STC}}{T}\right)^3 \exp\left[\frac{qE_g}{nK_B}\left(\frac{1}{T_{STC}} - \frac{1}{T}\right)\right] \tag{3.4.8}$$

where, E_g is the bandgap of the semiconductor ($1.121 ev$ for silicon). $I_{o,STC}$ can be obtained by rearranging the Eq. (3.4.3)-

$$I_{o,STC} = \frac{I_{sc,STC}}{\exp\left(\frac{qV_{oc,STC}}{nK_B T_{STC}}\right) - 1} \tag{3.4.9}$$

Eq. (3.4.8) is quite famous and has been used in many journals and studies to model the temperature dependence of the diode current [72–75]. The equation assumes the bandgap E_g to be constant when the temperature changes. However, it has been already discussed that, with the increase in the temperature, the bandgap in a semiconductor narrows, leading to the lower V_{oc} values. To accommodate such phenomena, the bandgap can be considered a function that changes linearly with the temperature, as shown in the following equation.

$$E_g = E_{g,STC}(1 + K_{E_g}\Delta T) \tag{3.4.10}$$

where, K_{E_g} is the temperature dependence of the bandgap factor. Its value is taken to be -0.0002677 for silicon semiconductor in system advisor model by NREL [71, 76]. For accurate calculation of diode current, Eq. (3.4.10) is inserted in Eq. (3.4.8). The resulting relation would be-

$$I_o = I_{o,STC}\left(\frac{T_{STC}}{T}\right)^3 \exp\left[\frac{q(E_{g,STC}(1 + K_{E_g}\Delta T))}{nK_B}\left(\frac{1}{T_{STC}} - \frac{1}{T}\right)\right] \tag{3.4.11}$$

However, if the temperature coefficient for voltage α_V is given in the specification (table), the diode saturation current from the Eq. (3.4.8) [73, 77] can be modified into following equation-

$$I_o = \frac{I_{sc,STC} + K_I\Delta T}{\exp\left(\frac{q(V_{oc,STC} + K_V\Delta T)}{nK_B T_{STC}}\right) - 1} \tag{3.4.12}$$

Both the equations Eq. (3.4.12) and Eq.(3.4.11) can be used to calculate the diode current accurately as they both consider temperature dependence of the bandgap. To get the final expression governing the I-V characterstcis of a PV cell, Eq. (3.4.12), (3.4.11) and (3.4.7) must be inserted in (3.4.2). The either of the resulting equations (appendix) can be used to model a PV cell. To model a PV module, a simple insertions of number of cells in series and parallel in the final equations should work, similar to the Eq. (3.4.6). An analogous approach can be fllowed to model a PV array.

3.4.1. SIMULATION RESULTS

Multiple ways of modeling PV modules have been discussed in the previous section. However, in this work of thesis the SIMULINK block for the PV array [78] has been employed which use similar equations discussed above to model the PV array. The I-V and P-V characteristics of the selected PV modules at constant temperature but variable irradiation levels are illustrated in figures 3.12 and 3.13 respectively. Where as figures 3.14 and 3.15 depict The I-V and P-v characteristics respectively when the module is subjected to various temperatures.
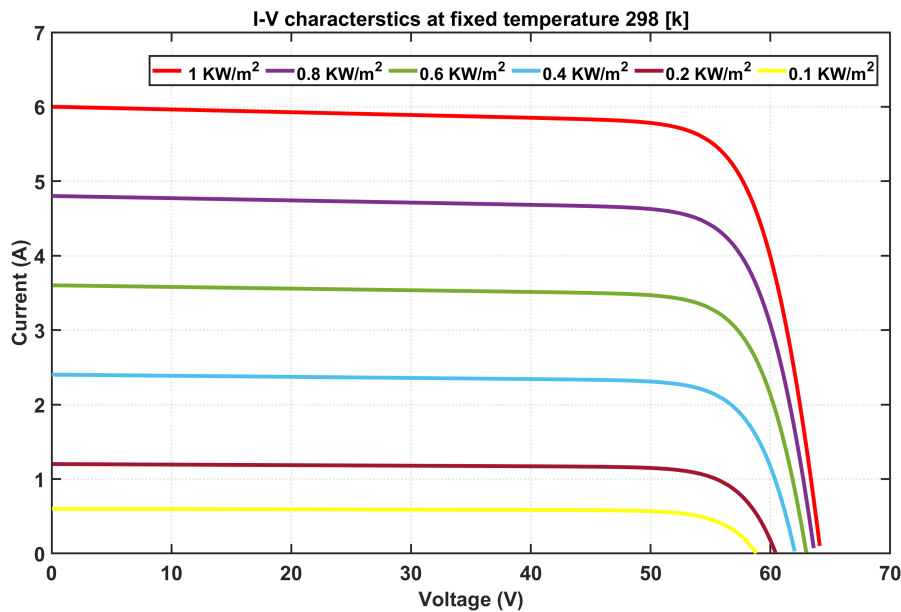
Figure 3.12: Current-Voltage characteristics of the PV module at various irradiation levels & at fixed temperature $(25°C)$

P-V curves at constant temperature 298 [k]
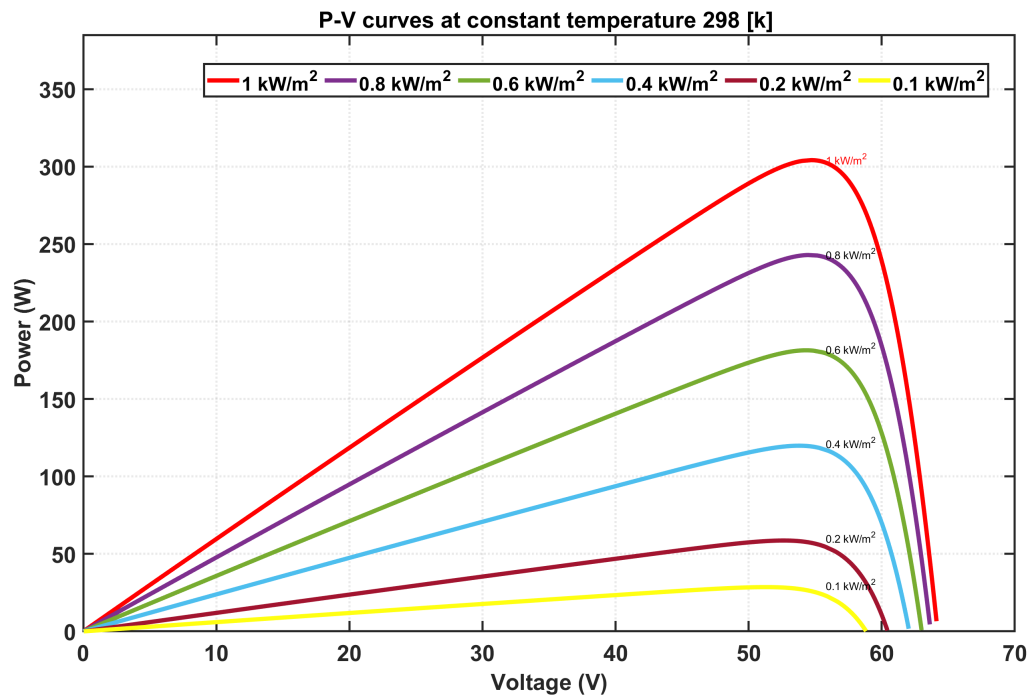
Figure 3.13: Power-Voltage characteristics of the PV module at various irradiation levels & at fixed temperature ($25°C$)

I-V characterstics at constant Irradiation 1000 W/m^2
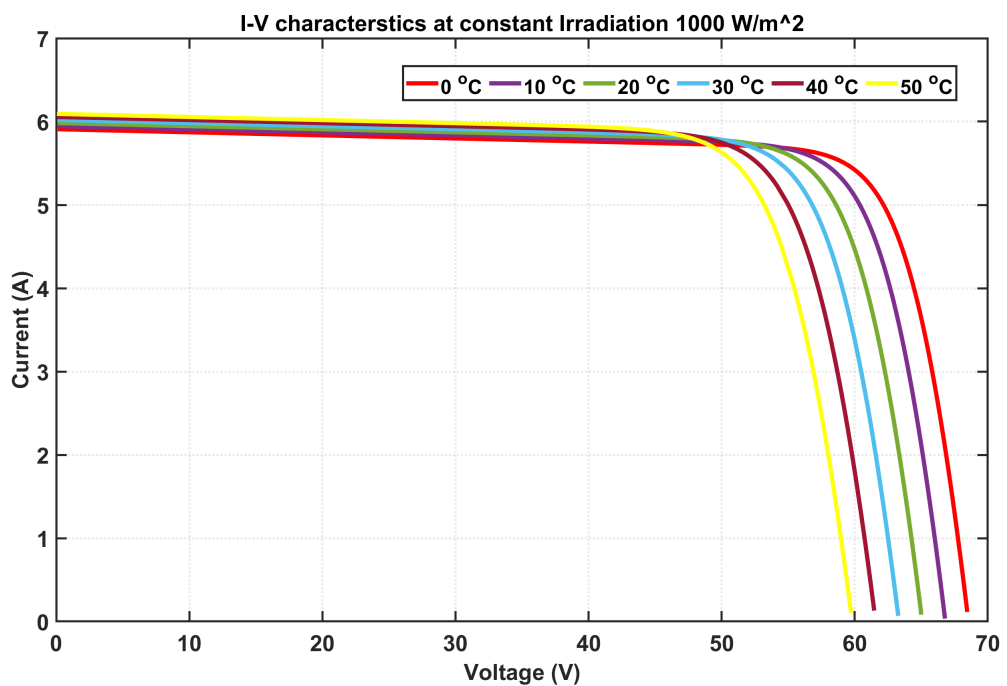
Figure 3.14: Current-Voltage characteristics of the PV module at constant irradiation level ($1000 W/m^2$) at different temperatures
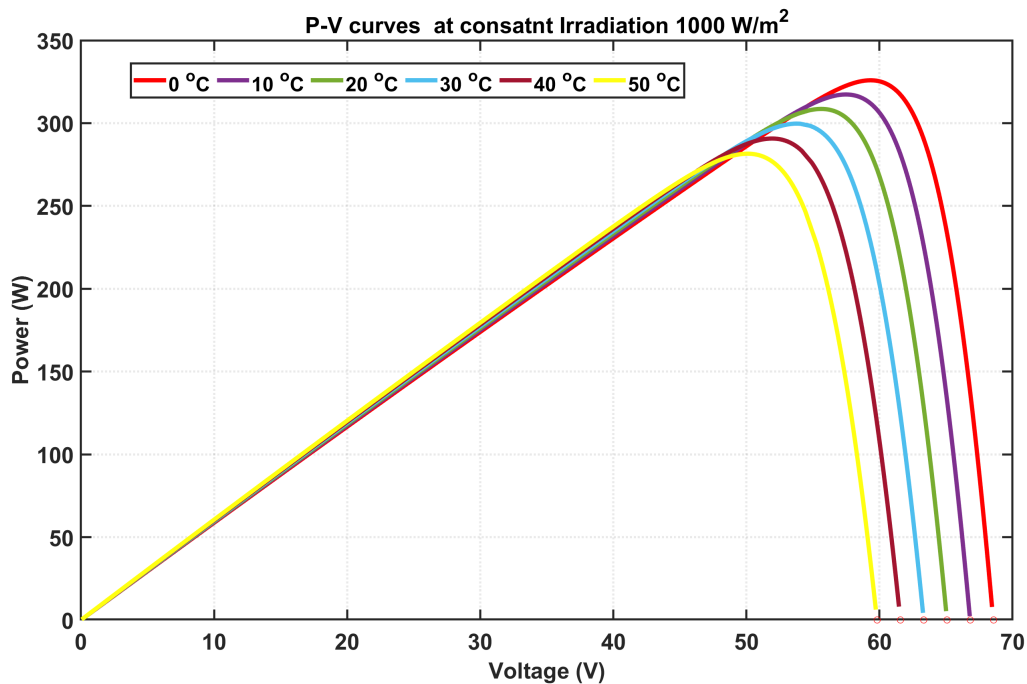
Figure 3.15: Power-Voltage characteristics of the PV module at constant irradiation level ($1000W/m^2$) at different temperature

3.4.2. CONCLUSIONS

Following conclusions can be drawn from the above figure-

- The performance of a photovoltaic module can vary significantly with regard to irradiance and temperature, resulting in fluctuations in power production.

- Increased irradiation results in an increase in electron-hole pair production, resulting in a greater output current (figure 3.12). When irradiation is reduced, the opposite occurs. Variations in irradiance have a minimal impact on the terminal voltages of photovoltaic modules in comparison to the output currents (figure 3.13). Thus, an increase in power production is achieved through an increase in irradiation.

- While the current generated increases slightly as the temperature rises, the decrease in voltages dominates, resulting in the reduced power output as the temperature rises (figures 3.14 and 3.15).

- Thus, maximum power can be extracted from the photovoltaic modules under circumstances of increased irradiation and reduced temperature.

The single diode model developed in this study is by far the most widely used model because it provides an excellent balance of practicality and simplicity. However, the single diode model is not ideal. Numerous approximations have been made in order to derive the mathematical expression describing the I-V characteristics. For example, it was presumed that no electron-hole pair generation or recombination occurs in the depletion zone, which is not the case in a true PN junction. Additionally, surface recombination is considered to be negligible, which is incorrect due to the finite thickness of a PN junction. To circumvent such approximations, researchers devised two- and even three-diode models with variable ideality factors. For more precise results, such models can be used in subsequent studies. Additionally, in reality, there are additional losses at the module level, such as shading losses caused by neighbouring objects and mismatches in the I-V characteristics of individual solar cells, which can result in bottlenecks in overall performance. Such losses have also not been considered in current study.

3.5. DESIGN OF PV SYSTEM COMPONENTS

This section briefly details several equations to design passive components of the PV system. Design of boost converter, LC filter and the DC link capacitor and in will be discussed. The values of all the

components and design parameters for all the PV systems are given in the appendix

3.5.1. DESIGN OF BOOST INDICATOR
The boost inductor is constructed with the limitation that the ripple current of the inductor is less than 15% of the maximum output current (I_{sc}) of the PV modules. Following equations [79] describe the calculation procedure for the inductance-

$$\Delta I < 15\% \tag{3.5.1}$$

$$\Delta I = \frac{V_{in}DT_s}{2L} \tag{3.5.2}$$

$$L > \frac{V_{in}DT_s}{2\Delta I} \tag{3.5.3}$$

where,
$\triangle I$ is the indicator ripple current.
T_s is the time interval between the switching cycles
D is the duty cycle V_{in} is equal to V_{oc} of the modules

3.5.2. INPUT FILTER CAPACITOR
The output of the PV modules is connected to a boost converter which is required to boost the voltage to the desired level. The input current to the the boost converter has a ripple at the switching frequency because of the presence of an inductor at its input. So a capacitor is necessary to provide high switching frequency ripple current, so that PV modules are not required to handle such high-frequency ripple current. Also, the performance of the maximum power point tracker might get affected in the absence of an input capacitor. In conclusion, the input filter capacitor is needed to filter out the high frequency ripple current such that the module sees a smooth current. The capacitance can be approximated by the following equation [73]-

$$C_{pv} \geq \frac{1}{8}\frac{T_s\Delta I}{\Delta V_{in}} \tag{3.5.4}$$

where, $\triangle V_{in}$ is the input voltage ripple. It is a design parameter and usually taken to be 1% of the output voltage of PV modules.

3.5.3. DC LINK CAPACITANCE
DC link capacitor is connected to the inverter input to smoothen out the input voltage ripple of the inverter. The inverter takes in DC quantities and outputs three-phase AC currents and voltages. When viewed from the three-phase AC to the DC side, the inverter can be seen as a three-phase rectifier (see figure 3.16). The output of a full-wave three-phase rectifier is depicted in the figure 3.17. Each diode in the rectifier conducts for one-third of the cycle (120°). However, for full current conduction, a pair of diodes must conduct simultaneously at the same instant. Therefore, effectively each diode pairs conducts only for one-sixth of the cycle. For instance, diode D1 conducts between 30° and 150° as depicted in the figure 3.17. But the diode pairs D1,2 and D1,6 conducts between 30° and 90°, and 90° and 150° respectively. Consequently, the frequency of the output DC ripple waveform is six times AC waveform. So the 50Hz AC waveform will have a reflection on the DC side as a sixth harmonic ripple (300Hz). So the capacitor has to be designed to handle the sixth harmonic ripple. Thus, the DC-link capacitor will experience charging and discharging cycles at 300Hz. The large capacitance value thus can be attributed to the low-frequency ripple. The actual design of DC link capacitor is challenging and tedious and it is beyond the scope of current thesis. Therefore, the DC link capacitor has been designed for a single phase system (EQ. 3.5.5 [80]) which experience two time the frequency of the AC waveforms at the DC side. Therefore, the designed capacitance should also work for the three phase system as well because if the capacitor is designed to handle 100Hz, it can easily handle 300Hz ripple.

$$C_{Dc-link} = \frac{3}{4}\frac{P}{2*f*V_{DC-link}^2} \tag{3.5.5}$$

where,
P is the nominal power of the system
$2*f$ corresponds to the 100Hz ripple and f is 50Hz
$V_{DC-link}$ is voltage across the DC link capacitor
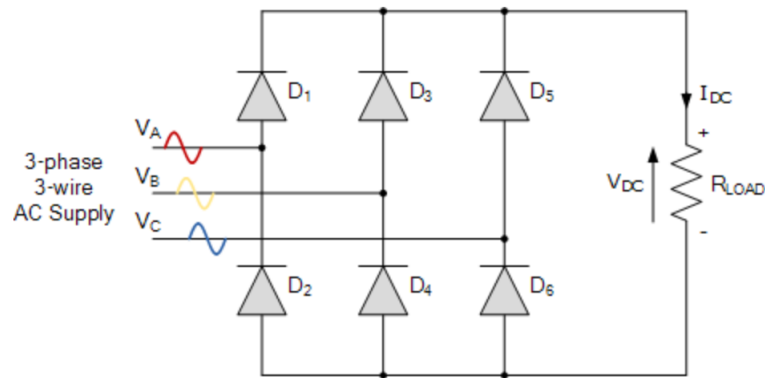
Figure 3.16: Circuit diagram of a diode based three phase full wave rectifier [5]
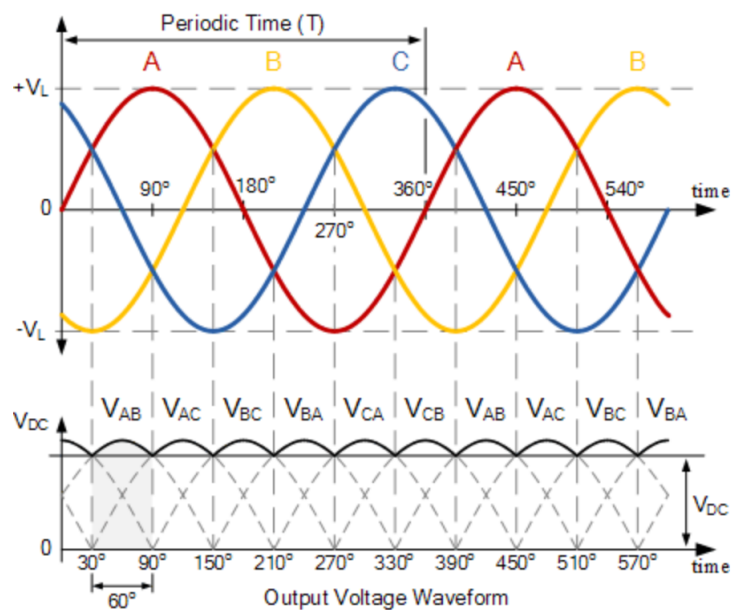
Figure 3.17: The DC voltage output of a diode based three phase rectifier [5]

3.5.4. Output AC filter

The output voltage and current of an inverter are pulsating waveforms with higher harmonic content close to the switching frequency. These high-frequency harmonics are attenuated using an LC filter. Over the course of a cycle, the average voltage across an inductor must be zero (from flux balance). As a result, the entire average voltage is applied across the filter's output. Inductance is a current stiff element as it does not allow a sudden change of current. Thus, an inductor smooths out the current waveform by introducing ripples. The capacitor now provides a parallel path for the inductor's ripple current.Due to the fact that the average current flowing through the capacitor is zero over a cycle (charge balance), the entire average current is directed via the load. Thus, an LC filter averages out current and voltage across a switching interval in this manner.

The figure 3.18 shows a schematic representation of an LC filter. R denotes the inductor coil's resistance (which is very small). The filter's transfer function is given by the equation,

$$\frac{V_o}{V_i} = \frac{1}{1 + sCR + s^2LC} \tag{3.5.6}$$

The LC filter is designed in the following steps.
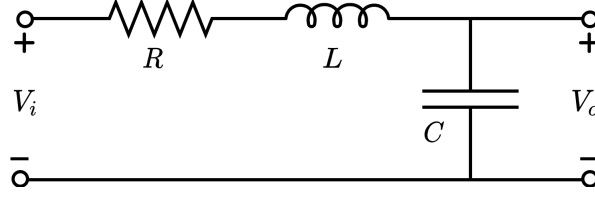
Figure 3.18: Schematic diagram of an LC filter

- To begin, a low resistance value is chosen.

- The second step is to select an inductance value, which is typically between 0.1 and 0.2 p.u. The real value of L is determined using the following equation.

$$L = \frac{L_{pu}V_b^2}{P_n 2\pi f} \tag{3.5.7}$$

where P_n is nominal power of the PV system, L_{pu} is the per unit value of the inductance, V_b is the base voltage and f is the frequency (50Hz)

- Third step involves deriving the capacitance from the Eq. (3.5.6) so that the filter provides at least -25dB (about 5% of the input magnitude) attenuation near the switching frequency.

- Finally, the R value is adjusted to obtain the appropriate quality factor (around 0.75). An online app is used to design LC filter [81]

3.6. GRID CONNECTION PRINCIPLE

Consider a grid, a single-phase grid, as shown in the figure (3.19). The voltage source V_i represents the output of the inverter, v_g is the grid voltage, and i_g is the current that is being injected into the grid. The inductance L represents the AC filter. It plays an integral part in reducing the harmonics generated by the inverter (also plays a role in removing circulating currents). To maximize the utilization of PV power, i_g should be in such a way that maximum active power is fed into the grid. In other words, the i_g waveform should be in phase with the grid voltage waveform v_g, at Unity power factor. Using KVL, the voltage equation of the loop can be written as $v_g + v_L = v_i$. Assuming $v_g = V_m \sin \omega t$ to be sinusoidal, the voltage across the inductor is $v_L = L \frac{di_g}{dt}$. Therefore,

$$v_i = L \frac{di_g}{dt} + v_g \tag{3.6.1}$$

Due to the unity power factor requirement, i_g should also be sinusoidal, similar to v_g. Hence, i_g can be written as $I_m \sin \omega t$. Now, The Eq. (3.6.1) becomes

$$v_i = V_m \sin \omega t + \omega L I_m \cos \omega t \tag{3.6.2}$$

The current flowing through the inductor is,

$$i_g = \frac{1}{L} \int (v_i - v_g) \, dt \tag{3.6.3}$$

The sinosoidal form grid current i_g can be obtained by replacing v_i in Eq. (3.6.3) with the Eq. (3.6.2). In other words, to obtian the unity power factor, the output voltage of the inverter v_i, must be equal to $L V_m \sin \omega t + \omega L I_m \cos \omega t$. The inverter, in this case, is modelled as a controlled voltage source. It can be controlled to obatain output voltage equal to Eq. (3.6.2). However, instead of controlling the output voltage of the inverter, the current i_g can be controlled by giving it as a feedback input signal to the current controller. The reference value of i_g must be set to achieve maximum PV power penetration. Now, the controller will do its job of appropriately giving the control input to the inverter such that the desire i_g will flow through the grid. The current controlled inverter, which works by taking the feedback signal of the measuring grid current and by setting the reference current according to the peak power of the photovoltaic module, is a very effective way of connecting the PV modules to the grid.
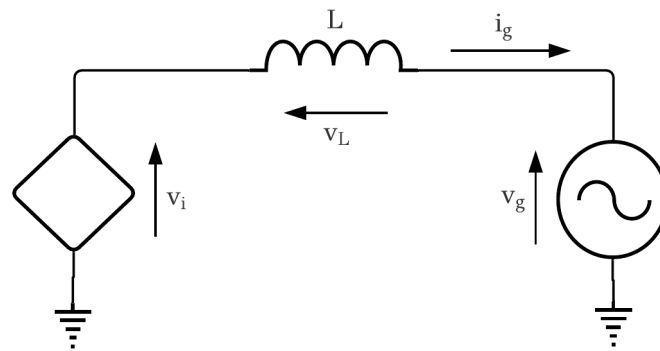
Figure 3.19: PV inverter connected to the grid

3.7. DQ TRANSFORMATION THEORY

In the last section, a brief introduction has been provided to the grid connection principle. In the control strategy, the currents are sensed, compared with a reference and based on the error the controller (including PWM) output will generate gate signals and inputs to each of the arms of the inverter. Due to the fact that grid voltages and currents are three-phase sinusoidal functions, the controller faces difficulty handling substantial signal deviations. Controllers that operate on AC quantities are referred to as tracking controllers. Furthermore, compared to setpoint controllers that operate on direct current values, tracking controllers have a smaller bandwidth and are more likely to produce steady-state errors. The design of a tracking controller is consequently far more sophisticated than a setpoint controller. So, to avoid such hassles, it is a common practice to convert the AC quantities to the DC values to design set point controllers, which are comparatively easier to design and implement. The AC quantities are converted to DC values by DQ transformation.

In the DQ axes theory, the time signals are transformed into space vectors in a spatial coordinate system that consists of rotating orthogonal axes. Consider sine and cosine waveforms as a function of time, as shown in the figure (3.20a). At each instant of time, the instantaneous amplitudes of sine and cosine waveforms can be projected into a spatial coordinate system comprising two orthogonal axes, alpha and Beta. This coordinate system is not connected with time, and hence both the axes are independent of time. The sine and cosine values are represented on alpha and beta axes, respectively. Consequently, a space vector from both the orthogonal components can be constructed, as shown in the figure (3.20b). As time evolves, the vector rotates along the locus of the circle. Every other intermediate point can be reached by the root of $\sin^2\theta + \cos^2\theta$ (if the max amplitude of sin and cos functions are one). So, once the sine (cosine) wave has progressed and completed one complete cycle, the space vector started from the α axis (β axis) and made a complete circle and came back to the α axis (β axis) again. The takeaway is that time signals are now converted into a space vector rotating in space. Now, this is the concept that would be used to convert AC signals to DC.

Consider another coordinate system called the DQ coordinate system, made up of d and q orthogonal axes, whose origin coincides with the $\alpha\beta$ coordinate system. The d and q axes are displaced from the α and β by an angle ρ, respectively, as shown in the figure (3.21). It is clear from the above discussion that the space vector formed from $\alpha\beta$ components rotates with time. In the DQ coordinate system, the d and q axes are synchronized with the space vector 'R', and the axes keep rotating at the same speed as 'R' as illustrated in the figure (3.21). Hence, the angle between the 'R' and d axis remains unchanged. Therefore, the orthogonal components thus projected onto the d and q axes are constant and do not change with time as long as the space vector 'R' do not change. In other words, it can be said that the d and q components are DC quantities. Because of this, all the controllers are designed in the d-q axis reference frame. Likewise, using a similar theory, the three-phase AC quantities can be converted into DC values in DQ coordinate system. The transformation matrix associated with such transformation is given in Eq. (3.7.1) [82], where the left-hand side variables represent DC values and right-hand side

(a) sin and cos functions in time domain

(b) sin and cos functions in $\alpha\beta$ coordinate system
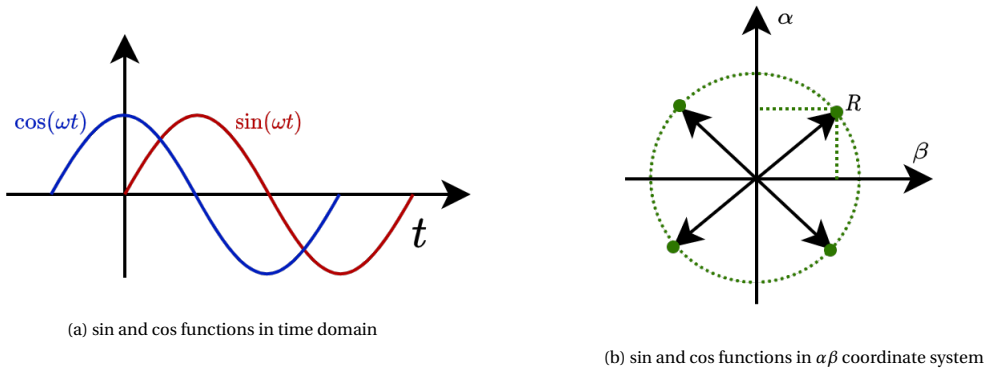
Figure 3.20: Transformation of sin and cosine time functions into $\alpha\beta$ coordinate system

variables represents three phase AC quantities. The active and reactive power in DQ coordinate system are given in Eq. (3.7.2) [82].
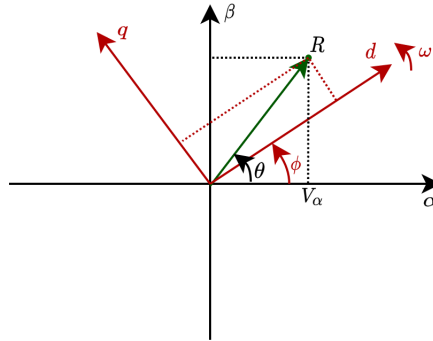
Figure 3.21: Representation of space vector in DQ coordinate system

$$
\begin{bmatrix} X_d \\ X_q \end{bmatrix} = \frac{2}{3} \begin{bmatrix} \cos(\omega t) & \cos(\omega t - 120°) & \cos(\omega t + 120°) \\ -\sin(\omega t) & -\sin(\omega t - 120°) & -\sin(\omega t + 120°) \end{bmatrix} \begin{bmatrix} X_a \\ X_b \\ X_c \end{bmatrix}
\tag{3.7.1}
$$

$$
P = \frac{3}{2}(V_d I_d + V_q I_q)
$$
$$
Q = \frac{3}{2}(V_d I_q - V_q I_d)
\tag{3.7.2}
$$

3.8. PER-UNIT SYSTEM

Often, power-electronic converter systems are convenient to design if expressed as per-unit quantities. Additionally, this project entails the implementation of multiple photovoltaic systems. If the per-unit technique is not adopted, it could be challenging to determine gain parameters for the controllers and reactive power control parameters in each photovoltaic system. So, to ease the design process, the per unit system has been used in this project. The following tables 3.2 and 3.3 contains the base values for the AC and DC side parameters of a voltage source inverter (VSI) system.

The tables 3.2 and 3.3 demonstrates that the base values for a VSI system which are considerably different from those for traditional power systems. For example, in typical power systems, the base value of the voltage is defined as the root mean square of the phase to neutral voltage. However, in the VSC system, the peak value of the phase to the neutral voltage at PCC is considered the base voltage. Regardless of whether the system is on DC or AC side, the base power remains constant. Nevertheless, the base

Quantity	Expression
Power	$P_{base-AC} = \frac{3}{2} V_{base-AC} I_{base-AC}$
Voltage	$V_{base-AC} = \widehat{V}_s$
Current	$I_{base-AC} = \frac{2P_{base-AC}}{3V_{base-AC}}$
Impedance	$Z_{base-AC} = \frac{V_{base-AC}}{I_{base-AC}}$
Inductance	$L_{base-AC} = \frac{Z_{base-AC}}{\omega_{base-AC}}$
Capacitance	$C_{base-AC} = \frac{1}{Z_{base-AC}\omega_{base}}$
Frequency	$\omega_{base-AC}$

Table 3.2: Base values for the AC side parameters [14]

Quantity	Expression
Power	$P_{base-DC} = V_{base-DC} I_{base-DC} = P_{base-AC}$
Voltage	$V_{base-DC} = 2V_{base-AC}$
Current	$I_{base-DC} = \frac{3}{4} I_{base-AC}$
Impedance	$R_{base-DC} = \frac{8}{3} Z_{base-AC}$
Inductance	$L_{base-DC} = \frac{8}{3} L_{base-AC}$
Capacitance	$C_{base-DC} = \frac{3}{8} C_{base-AC}$

Table 3.3: Base values for the DC side parameters [14]

voltage on the DC side relies on the PWM method employed. The DC side voltage base used in this case corresponds to the sine pulse width modulation technique.

3.9. Overview of the inverter control

The inverter control used in this thesis is **voltage oriented control** [3, 37, 72, 73, 82–88] which is a very established, matured and easily comprehensible control technique to employ grid connected PV system. The inverter control's general framework is illustrated in the figures 3.22 and 3.23. Prior to the first stage of control, grid currents and voltages and the DC link voltages are measured and converted into DC quantities. The outer voltage control loop is the initial step in the control scheme. It operates on
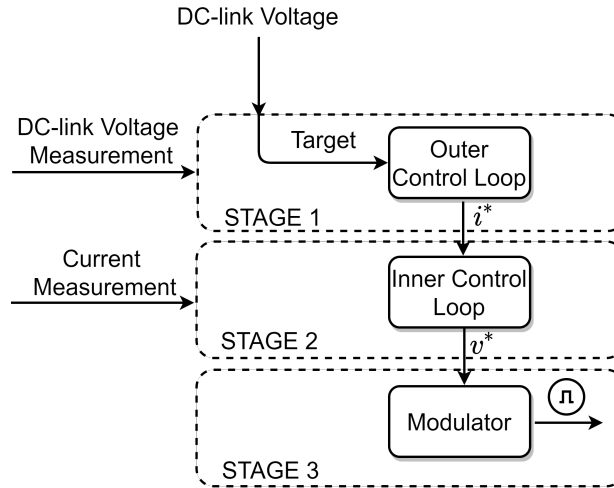
Figure 3.22: General control layout of an inverter
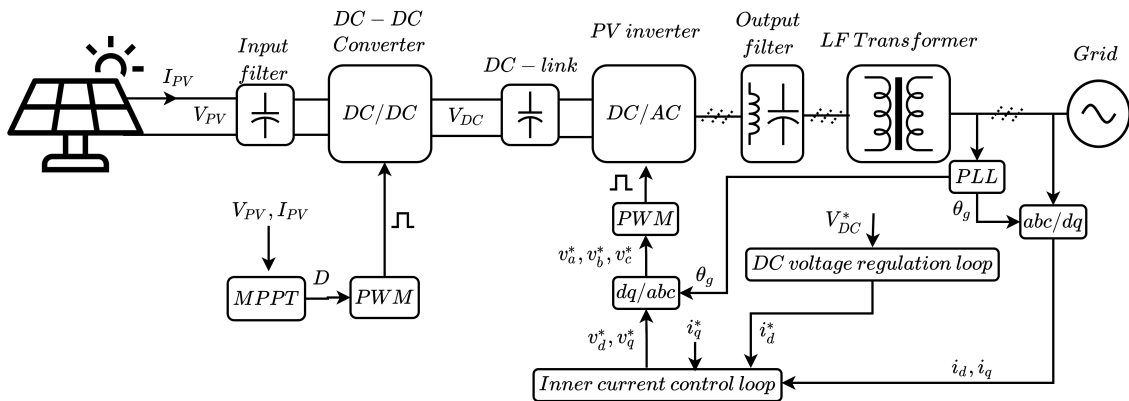
Figure 3.23: Detailed control layout of the PV system

user-defined targets such as maintaining a constant DC link voltage (by controlling the current being injected into the grid) and outputs the reference currents that the inverter must generate. The second stage of control employs the inner current control loop to generate reference voltages from the reference currents generated in the first stage. In the final stage of control, the modulator receives the reference voltage signals and generates appropriate firing pulses for the inverter's gate signal. This is how the inverter's output voltage is maintained the same as the reference voltage generated in the second stage. It is essential to note that the control mechanism used here is particularly unique to this project. FACTS devices such as STATCOM can be programmed to employ a similar control scheme; however, it incorporates an additional stage where the reference voltages are modified in further steps according to the requirement.

3.9.1. Outer control loop

The voltage at the DC link capacitor is referred to as the DC link voltage. The DC link voltage varies in response to the amount of energy generated by the PV modules. As PV power production grows, the

voltage overshoots; as it declines, the voltage undershoots. As a result, to compensate for such transient states, the DC voltage control seeks to maintain a constant voltage by driving the capacitor to charge and discharge in accordance to the generated power. DC link coltage regulation is achieved by adjusting the amount of power exchanged between the converter and the grid. For instance, if the voltage drops due to low PV power generated, the power exchanged with the grid declines to maintain a constant voltage at the DC link capacitor. When the DC link capacitor is subjected to a power surge, a similar rationale can be developed. Increasing or decreasing the current being injected into the grid can regulate the power flow into the grid. So, to summarise, the DC link voltage is maintained constant by managing the amount of current injected into the distribution network. The DC link voltage plant is shown in the figure 3.25. The plant transfer function can be obtained as follows, active power fed into the grid is,

$$P = \frac{3}{2}(e_d i_d + e_q i_q) \tag{3.9.1}$$

where e_d, e_q are the direct (d) and quadrature (q) components of grid voltages e_a, e_b and e_c and i_d, i_q are the direct (d) and quadrature (q) components of currents i_a, i_b and i_c being injected into the grid. Since the d axis coincides with the grid voltage space vector (more on this in later sections), $e_q = 0$ and e_d is equal to the peak value of the grid phase to neutral voltage. The Eq. (3.9.1) becomes,

$$P = \frac{3}{2}e_d i_d \tag{3.9.2}$$

So, the power injected into the grid can be controlled by controlling i_d. Therefore, the plant transfer function must be determined between DC link voltage and the grid current i_d. Assuming the voltages, across both the capacitors is balanced, the current equation at point P in the figure 3.25 can be written as,
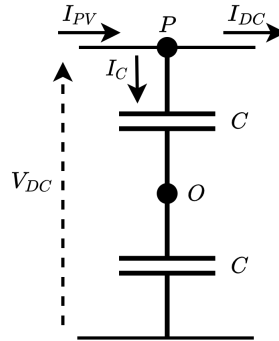
Figure 3.24: Equivalent circuit at the DC-link capacitor

$$i_c(t) = i_{PV}(t) - i_{DC}(t) \tag{3.9.3}$$

$$\frac{C}{2}\frac{dv_{DC}(t)}{dt} = i_{PV}(t) - i_{DC}(t) \tag{3.9.4}$$

Where, $C/2$ is the effective capacitance, v_{DC} is the total DC link voltage, i_{PV} is the current coming from the PV side, i_{DC} is the input current to the inverter. Since, the output and the input power of the inverter must be equal,

$$V_{DC} i_{DC}(t) = \frac{3}{2}e_d i_d(t) \tag{3.9.5}$$

$$i_{DC}(t) = \frac{3}{2}\frac{e_d i_d(t)}{V_{DC}} \tag{3.9.6}$$

$$\frac{C}{2}\frac{dv_{DC}(t)}{dt} = i_{PV}(t) - \frac{3}{2}\frac{e_d i_d(t)}{V_{DC}} \tag{3.9.7}$$

$i_{PV}(t)$ is a load element and can be considered as the disturbance. so Eq. (3.9.7) becomes

$$\frac{C}{2}\frac{dv_{DC}(t)}{dt} = -\frac{3}{2}\frac{e_d i_d(t)}{V_{DC}} \tag{3.9.8}$$

Due to the fact that the per unit model is used throughout the control, the equation must be converted to a per unit form. The base values from the tables 3.2 and 3.3 can be used. Dividing the Eq. (3.9.8) by $I_{base-dc}$, yields

$$\frac{C}{2I_{base-dc}} \frac{dv_{DC}(t)}{dt} = -\frac{3}{2} \frac{e_d i_d(t)}{I_{base-dc} V_{DC}} \tag{3.9.9}$$

$$\frac{C}{2} \frac{Z_{base-dc}}{V_{base-dc}} \frac{\omega_{base}}{\omega_{base}} \frac{dv_{DC}(t)}{dt} = -2 \frac{e_d i_d(t)}{I_{base} V_{DC}} \tag{3.9.10}$$

$$\frac{C}{2} \frac{V_{base-dc}}{I_{base-dc}} \omega_{base} \frac{dv'_{DC}(t)}{dt} = -2 \frac{e_d i'_d(t)}{V_{DC}} \tag{3.9.11}$$

$$\frac{C}{2} \frac{V^2_{base-dc}}{P_base} \omega_{base} \frac{dv'_{DC}(t)}{dt} = -2 \frac{e_d i'_d(t)}{V_{DC}} \tag{3.9.12}$$

Applying the Laplace transform and rearranging the terms, the plant transfer function can be obtained as follows,

$$\frac{V_{DC}(s)}{I_d(s)} = -\frac{4P_{base}e_d}{CV^3_{DC}\omega_{base}} \frac{1}{s} \tag{3.9.13}$$

$V_{DC}(s)$,$i_d(s)$ **are in per units**. The plant model and the closed loop control for the DC link is shown in figures 3.25 and 3.26 respectively.
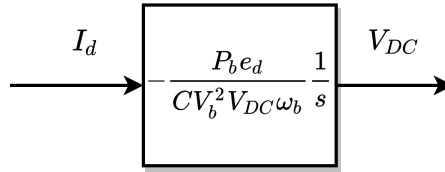
Figure 3.25: Transfer function of the Plant model for outer control loop
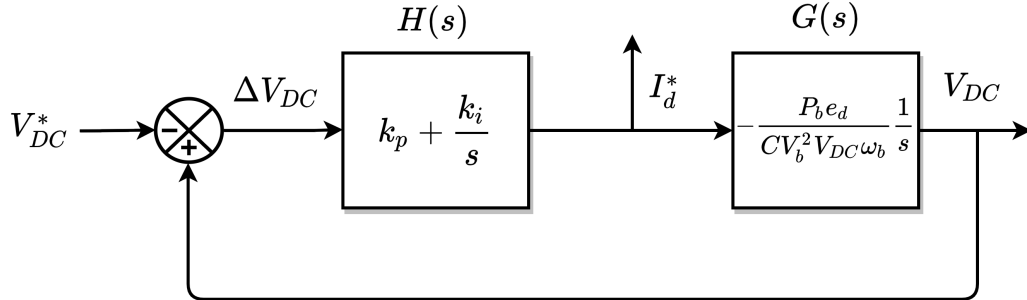
Figure 3.26: Closed loop control of the DC link voltage

3.9.2. INNER CONTROL LOOP

Earlier in the grid connection principle, it was commented that the inverter's output current is controlled to obtain the peak PV power injection. Therefore, to implement the inner current controller, the dynamic equations representing the inverter's output current must be known. Such equations can be derived by understanding what components are connected to the output terminals of the inverter. Figure 3.23 depicts the PV system structure employed in this project. The components connected to the inverter's output are an LC filter and a transformer. To simplify the design of the inner current control, the capacitor (part of the LC filter) and the magnetizing current component of the transformer are neglected. The resulting plant model is depicted in the figure 3.27. Using Kirchoff's law, the current equations of the plant are as follows.
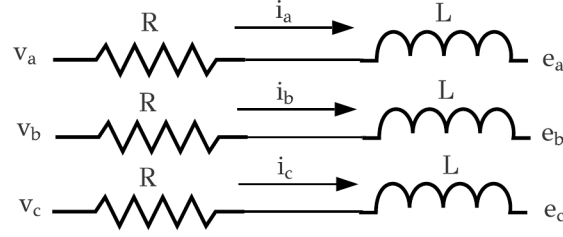
Figure 3.27: Circuit equation at the AC side

$$\frac{di_a}{dt} = \frac{1}{L}(-Ri_a + v_a - e_a)$$
$$\frac{di_b}{dt} = \frac{1}{L}(-Ri_b + v_b - e_b) \qquad (3.9.14)$$
$$\frac{di_c}{dt} = \frac{1}{L}(-Ri_c + v_c - e_c)$$

where, v_a, v_b, v_c and e_a, e_b, e_c represents the phase to neutral voltage of the inverter output and the grid. i_a, i_b, i_c are the currents flowing into the grid. All these variables are functions of time. L and R represent the sum of the AC filter's and transformer's primary and secondary windings inductance and resistance respectively. Writing all the Eq. (3.9.14) in a single equation yield,

$$\frac{di_{abc}}{dt} = \frac{1}{L}(-Ri_{abc} + v_{abc} - e_{abc}) \qquad (3.9.15)$$

Since the per unit system is being followed in designing the control system, the per unit values of all the variables in the Eq. (3.9.15) can be defined as,

$$L' = \frac{\omega L}{z_{\text{base}}} \quad R' = \frac{R}{z_{\text{base}}} \quad i'_x = \frac{i_x}{i_{\text{base}}} \quad v'_x = \frac{v_x}{v_{\text{base}}} \quad e'_x = \frac{e_x}{v_{\text{base}}} \quad z_{\text{base}} = \frac{v_{\text{base}}}{i_{\text{base}}} \qquad (3.9.16)$$

where, the prime quantities denote per-unit value, x represents abc phases and ω is grid frequency in radians. Now, the per-unitized AC side equation can be written in matrix form as,

$$\frac{d}{dt}\begin{bmatrix} i'_a \\ i'_b \\ i'_c \end{bmatrix} = \begin{bmatrix} \frac{-R'\omega}{L'} & 0 & 0 \\ 0 & \frac{-R'\omega}{L'} & 0 \\ 0 & 0 & \frac{-R'\omega}{L'} \end{bmatrix}\begin{bmatrix} i'_a \\ i'_b \\ i'_c \end{bmatrix} + \frac{\omega}{L'}\begin{bmatrix} (v'_a - e'_a) \\ (v'_b - e'_b) \\ (v'_c - e'_c) \end{bmatrix} \qquad (3.9.17)$$

The AC quantities in Eq. (3.9.17) will be converted into DC quantities using DQ transformation theory. So the matrix associated to the DQ transformation is given by,

$$\begin{bmatrix} X_d \\ X_q \end{bmatrix} = \frac{2}{3}\begin{bmatrix} \cos(\omega t) & \cos(\omega t - 120°) & \cos(\omega t + 120°) \\ -\sin(\omega t) & -\sin(\omega t - 120°) & -\sin(\omega t + 120°) \end{bmatrix}\begin{bmatrix} X_a \\ X_b \\ X_c \end{bmatrix} \qquad (3.9.18)$$

After applying the DQ transformation using the Eq (3.9.18), the resulting matrix in DQ domain [89] is given as follows,

$$\frac{d}{dt}\begin{bmatrix} i'_d \\ i'_q \end{bmatrix} = \begin{bmatrix} \frac{-R'\omega}{L'} & \omega \\ -\omega & \frac{-R'\omega}{L} \end{bmatrix}\begin{bmatrix} i'_d \\ i'_q \end{bmatrix} + \frac{\omega_b}{L'}\begin{bmatrix} (v'_d - |e'_d|) \\ (v'_d - |e'_q|) \end{bmatrix} \qquad (3.9.19)$$

Rearranging the terms after applying the laplace transform on both the sides, the direct and quadrature components of output voltage of the inverter, are given by,

$$V_d = \frac{sLI_d}{\omega_{base}} + RI_d - LI_q + E_d \qquad (3.9.20)$$

$$V_q = \frac{sLI_q}{\omega_{base}} + RI_q + LI_d + E_q \tag{3.9.21}$$

Except the base value of ω, all the quantities are in per-units and the time variables are converted to laplace domain in the Eq. (3.9.20) and (3.9.21). Eq (3.9.19) represent Multiple Input Multiple Output system (MIMO) where the inputs and the outputs are,

$$[u] = \begin{bmatrix} v_d \\ v_q \end{bmatrix}, [y] = \begin{bmatrix} i_d \\ i_q \end{bmatrix} \tag{3.9.22}$$

The controller for the aforementioned system can be designed in two ways. A multi variable control strategy can be adopted. The other technique aims to dissociate the equations for the d and q axes, converting the MIMO system to two discrete Single Input Single Output (SISO) systems [90]. The present work takes the second strategy, which is discussed below. If the configuration of the control inputs V_d and V_q is as follows,

$$\begin{aligned} V_d &= V_d' - LI_q + E_d \\ V_q &= V_q' + LI_d + E_q \end{aligned} \tag{3.9.23}$$

equations Eq. (3.9.20) and Eq. (3.9.21) can be written as,

$$\begin{aligned} V_d' &= \frac{sLI_d}{\omega_{base}} + RI_d \\ V_q' &= \frac{sLI_q}{\omega_{base}} + RI_q \end{aligned} \tag{3.9.24}$$

Each of the aforementioned equations in Eq (3.9.24) are independent of one another, resulting in an independent SISO system. Current control can now be implemented simply using conventional frequency domain strategies. By rearranging the terms, the transfer function for both the system can be given as,

$$\begin{aligned} G_d &= \frac{I_d}{V_d'} = \frac{1}{R + s\frac{L}{\omega_{base}}} \\ G_q &= \frac{I_q}{V_q'} = \frac{1}{R + s\frac{L}{\omega_{base}}} \end{aligned} \tag{3.9.25}$$

The plant model for d and q components are shown in figure 3.28. The current control loops in d and q axes including feed forward terms are shown in figures 3.29 and 3.30
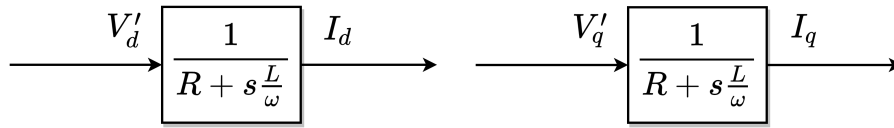
Figure 3.28: Plant model for d and q axes of the inner control loop

The inner current control acquires the reference current I_d^* from the outer voltage control at each sample period. The reference currents correspond to the current fed by the inverter into the grid. The PI controller has been used here to drive the error signal ΔI_d to zero. The derivation of the gain parameters, k_p and k_i has been given in appendix. The pulse width monitor receives the reference voltages in abc domain and generates gate pulses for the inverter. The inner control's function is to generate such reference voltages (V_d and V_q) so that the inverter's output current has the same shape as reference currents in the abc domain. The full control, including inner and outer control loops, is illustrated in figure 3.31
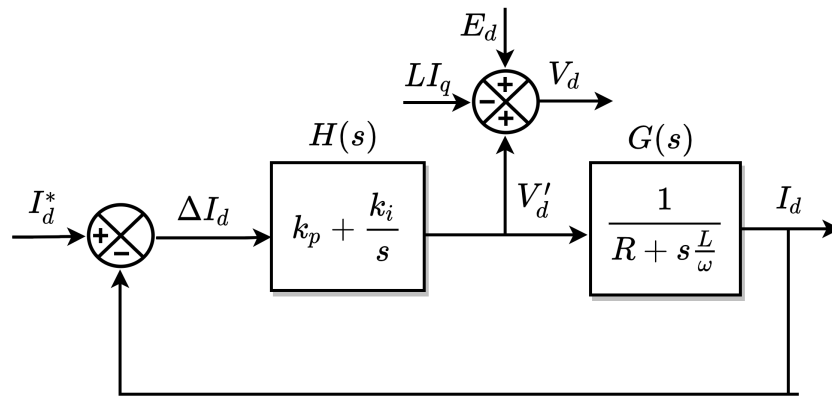
Figure 3.29: Closed loop control of d axes component of grid current
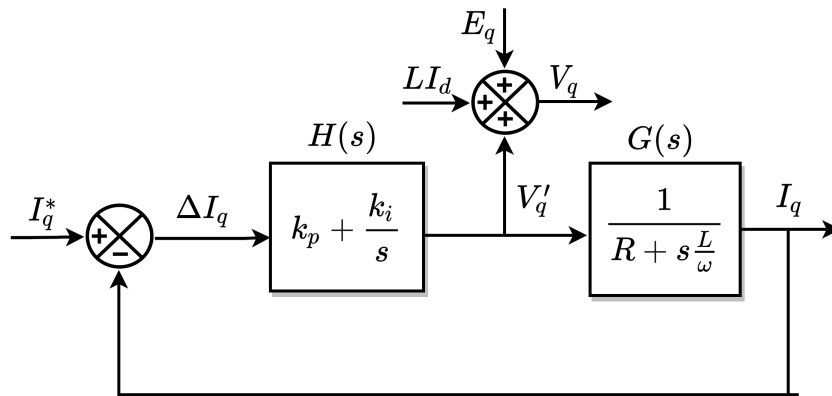
Figure 3.30: Closed loop control of q axes component of grid current
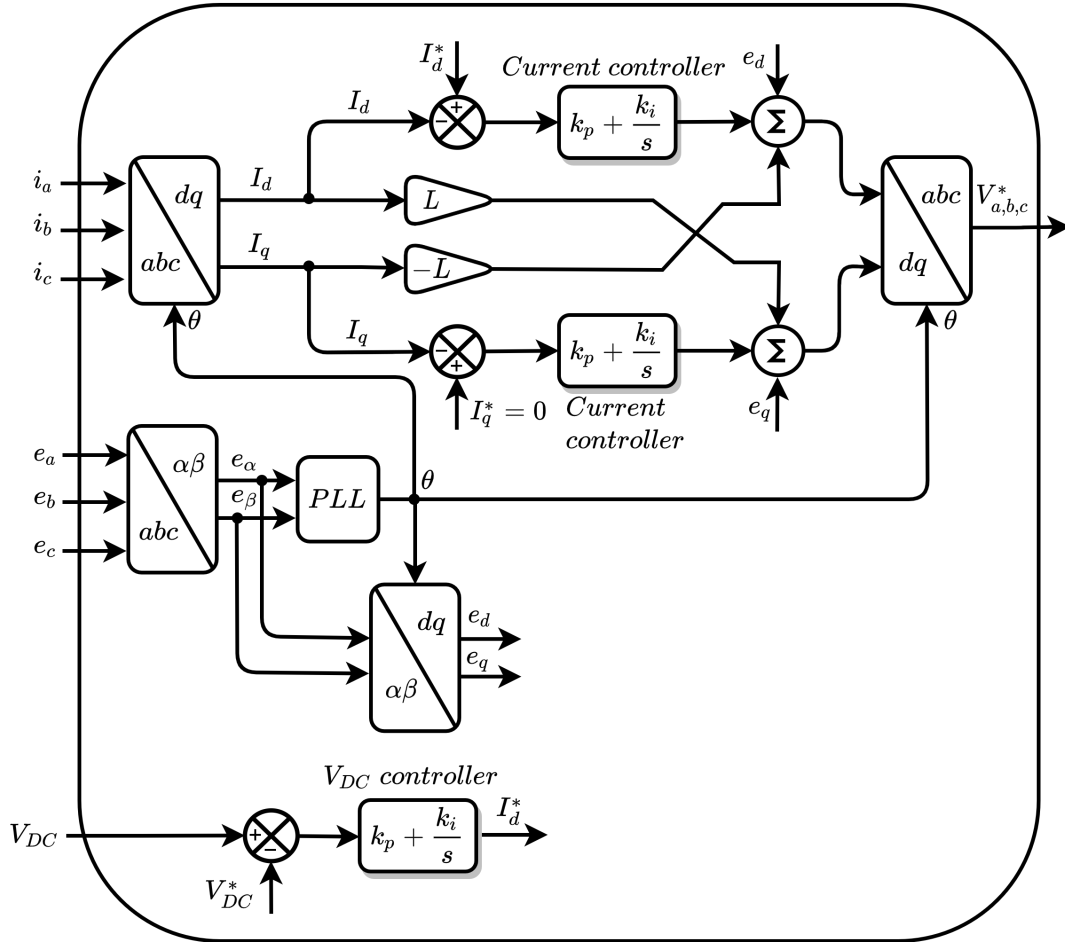
Figure 3.31: Schematic representaion of control scheme of the inverter

3.10. PHASE LOCKED LOOPS (PLL)

In the grid connection principle section, it has been discussed that the inverter should convert the DC power it receives to the three-phase active power for the maximum utilization of power produced by the PV modules. In other words, the inverter must operate at a unity power factor, resulting in zero reactive power injection into the grid. DQ transformation theory has been clearly discussed in the previous sections. In that theory, the grid's AC currents and voltages are measured and converted into the direct (d) and quadrature (q) DC components to simplify the controller design. The direct component corresponds to active power, and the quadrature component corresponds to reactive power. The active and reactive power generated by the inverter can be represented in dq quantities by the Eq. (3.9.1)

$$P = \frac{3}{2}(V_d I_d + V_q I_q)$$
$$Q = \frac{3}{2}(V_d I_q - V_q I_d)$$

(3.10.1)

Under unity power factor conditions, the quadrature component of grid current and voltage must be zero from the equations. Therefore, the I_q is set to zero in the inner current control block. To make the quadrature component of the voltage (V_q) zero, the d axis coincides with the voltage space vector as shown in the figure 3.32

So the device that ensures such synchronization all the time is the Phase Locked Loop (PLL). PLL is a closed-loop control system that maintains the same phase and frequency between the output and input signals, like sinusoidal signals, by tracking them using an internal frequency oscillator. The outputs of the PLL are the phase and frequency of the input signal. The output phase, thus used by the DQ
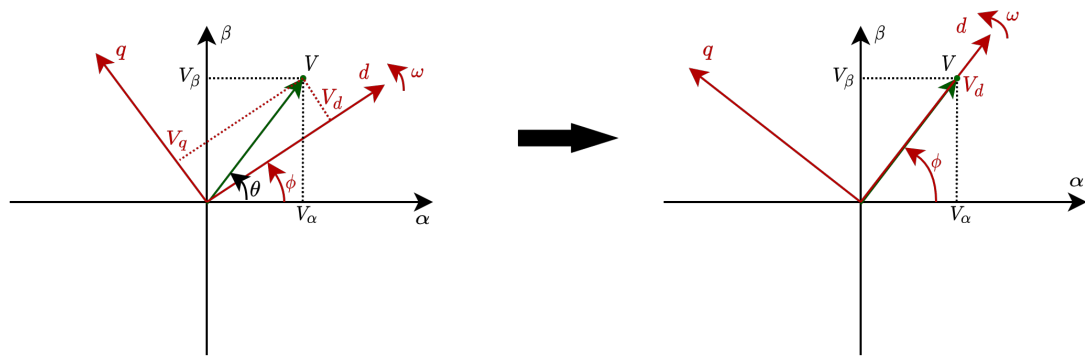
Figure 3.32: Transformation of d and q components of voltage space vector

transformation equations to synchronize the d axis to the voltage space vector. A typical PLL used in the PV systems' control is illustrated in the figure 3.33.
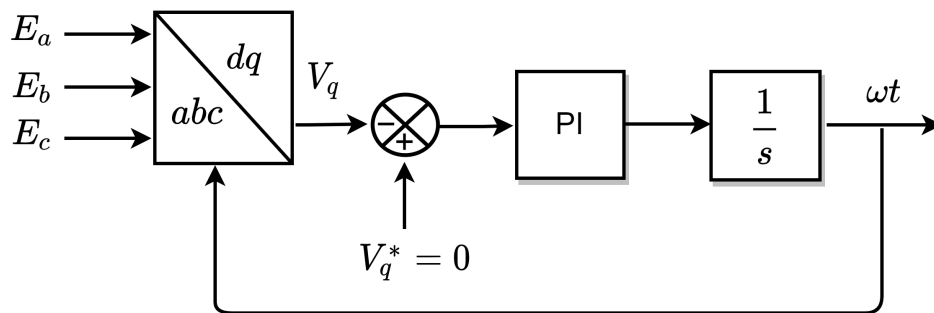
Figure 3.33: PLL control scheme

Where E_a, E_b, E_c are the three phase grid voltages. The control loop in PLL drives the difference between measured V_q and reference V_q to zero. To obtain unity power factor, the reference V_q must be set to zero. So the appropriate phase is obtained for which quadrature component of the voltage vector is zero. The Simulink library consists of a similar PLL but more advanced. The suitable gain parameters have already been established in the block. So, to ease the design process, the mentioned PLL block is considered in this thesis.

4
PROBLEM FORMULATION

The previous chapter thoroughly discussed the design of the photovoltaic system, as well as the control strategy implemented. in this and the subsequent chapter the designed photovoltaic systems are connected to the grid at various locations . The resulting network is simulated, and the consequent behaviour is analyzed. Maximum voltage and PV penetration investigations are carried out on the chosen low voltage distribution network at varying distances between the source and the loads. Finally, pertinent conclusions are deduced, paving the way for the subsequent chapters.

PV systems of various configurations are integrated into the low voltage distribution network. There are a total of six loads connected to the various buses in the residential subnetwork (refer to figure 2.1). Among these, the load connected to bus R1 indicates the effective load of other feeders connected to the residential sub-network (not depicted in the diagram). The remaining loads represent the cluster of residential houses/buildings connected to the residential network. Therefore, except for the load connected to bus R1, the PV systems have been connected to all other loads (connected to the buses R11, R15, R16, R17 and R18 in the figure 2.1). A similar approach is followed for the commercial subnetwork. The PV penetration is defined as the ratio of the peak PV power produced to the peak load power consumption, as seen in the Eq. 4.0.1.

$$PV\ Penetration = \frac{Peak\ PV\ power}{Peak\ load\ power} \qquad (4.0.1)$$

This concept was derived from the National Renewable Energy Laboratory's projects [36] . For the 100% PV penetration, the photovoltaic systems have been constructed in such a way that the maximum power generated by the modules at peak irradiation is equal to the maximum power consumed by the loads on a given day. The resulting residential network model was simulated, and the following results were obtained. The figure **??** clearly shows that the voltages at various PCCs are between 0.95 and 1.1 p.u (0.95 p.u. and 1.1 p.u. are chosen as the lower and upper voltage limits in this project).
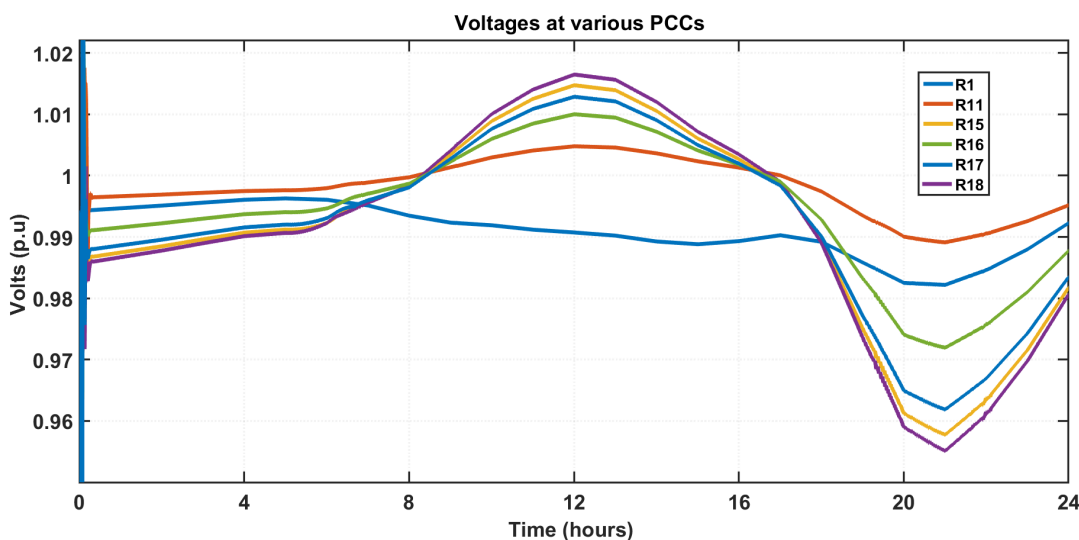
Figure 4.1: Caption

As a result, 100 percent PV penetration for the residential subnetwork is feasible without violating grid voltage constraints. This, however, may not be the case when the distance between the source and the loads' increases. The voltages at the PCCs and the network parameters are related as follows:

$$\Delta V = \frac{PR_{line} + QX_{line}}{|V_{Pcc}|} \tag{4.0.2}$$

where P and Q signify the active and reactive power fed into the grid, R and X denote the distribution line's resistance and inductance, and ΔV denotes the voltage rise. According to the equation, the ΔV rises as the R and X of the line increase. When the distance between the source and load increases, the LV distribution line's resistance and inductance increase as well. As a result, the PCC voltages continue to rise. To simulate this phenomena, the length of the residential subnetwork was increased in several increments from its initial length to twenty times its original length. The figure 4.2a depicts the outcomes. The same figure illustrates the highest voltage recorded at various buses (to which photovoltaic systems are connected) throughout a range of feeder lengths. The voltage rise is maximum at bus R18 owing to the highest rating of the PV system and longer distance connected to that bus. On the bus R11, the opposite happens. After a certain distance, the voltages at the buses exceed 1.1 p.u., which is not desirable, as previously mentioned. However, if the same analysis is done for the commercial or industrial subnetwork, there will not be any severe voltage rise because the peak load consumption of the commercial and industrial loads coincides with the peak PV power production as seen in the figure 3.2. Therefore, there would not be large amounts of reverse power flowing into the grid. The severity of the voltage rise problem is minimal. Therefore, penetration levels could be maximum in those cases. Figure 4.3 shows the voltages obtained at various load buses (or PCC) in the residential and commercial subnetwork, during good irradiance period between 8:00 and 16:00 hours, for the distance factor 20 times. Clearly, the figure 4.3b illustrates the maximum voltages recorded at commercial loads are well below 1.1 p.u. Similar results can be obtained for industrial network as well. Hence, no voltage control methods are required for the industrial and commercial loads.

(a) The maximum voltages recorded at various buses at various distances

(b) Decrease of PV penetration with the increase in feeder length
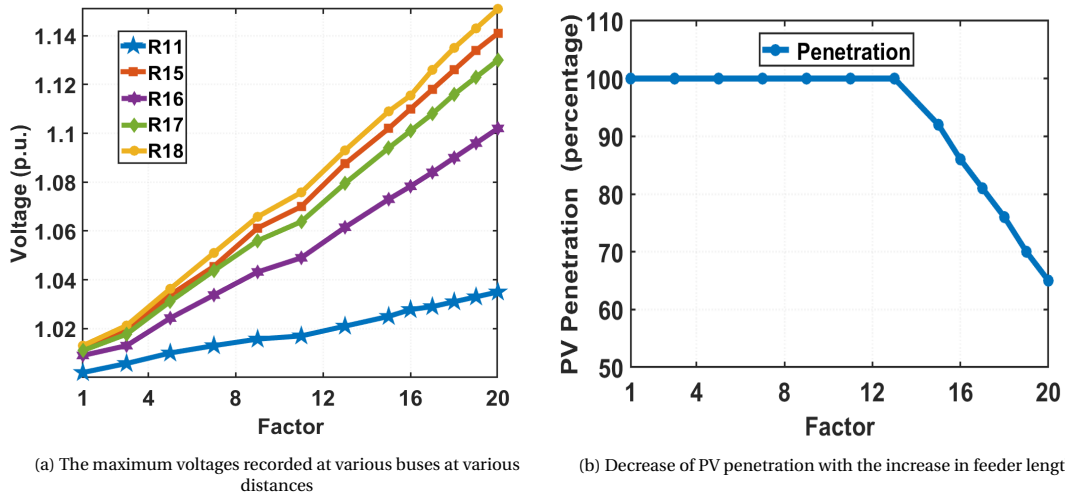
Figure 4.2: PV Penetration analysis

(a) Voltages at various PCCs in the residential subnetwork

(b) Voltages at various PCCs in the commercial subnetwork
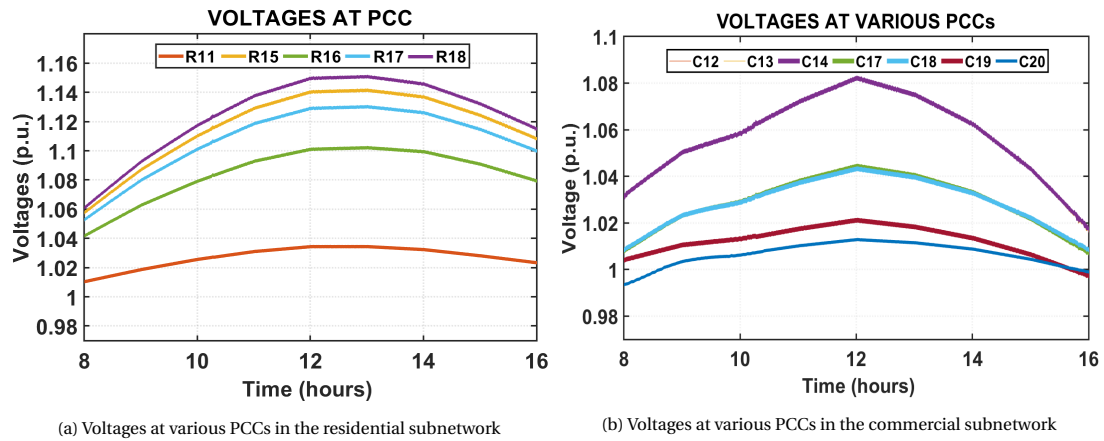
Figure 4.3: Voltages at various PCC in residential and commercial network

The PV penetration is affected by the increase in the length of the network. Because of the voltage rise problem, PV systems have to be designed at lower ratings to curtail the power produced. The figure 4.2b depicts the penetration levels at various distance factors. For a particular distance, the lowest of all the penetration levels obtained at various buses is considered to be the penetration level of the residential subnetwork. For example, if the PV penetration is 65 percent at bus R18 and greater at other buses, the PV penetration of the residential network is considered as 65 percent, the same as at bus R18. If the average PV penetration is used as the penetration level for the entire network, even if the PV system is constructed at the average PV penetration level, a voltage rise may still occur. The figure 4.2b depicts that after a certain distance, the penetration decreases and reaches 65% for the length 20 times. The worst-case (20 times the original length with 65% penetration) has been selected for further studies to improve the penetration levels. Also to account for the losses due to higher distances reactive power is injected into the grid to bring the voltages within limits. Various solutions as to how to increase the PV penetration have been discussed in the next chapter.

<div align="right">

5

</div>

<div align="right">

SOLUTIONS

</div>

This chapter begins with an overview of the effect of reactive power on voltages. Then it is explained how reactive power can be absorbed and injected via the inverter control. Two strategies are proposed to improve pv penetration. The first category is reactive power control methods, whereas the second category is active power control methods. In the first method, the reactive power is absorbed by the PV system so that voltages at the PCCs are within the grid voltage limit. The second way is based on active power control, in which the voltages are controlled by a battery/electrolyzer.

5.1. BACKGROUND ON THE INFLUENCE OF REACTIVE POWER INJECTION/ABSORPTION ON VOLTAGES

Voltages at the consumer end should be kept in required limits as much as possible because most devices, apparatus, and machines are designed to operate at their rated value. If the voltage varies significantly from the rated value, the device's performance may be adversely affected. Therefore specific techniques must be used to regulate the voltages. Voltage sags can occur for a variety of causes. One such factor is escalating consumer demand for power (both active and reactive). The relationship between voltage sag and reactive power is not as straightforward as the relationship between active power and voltage sag as it can be said that higher active power consumption can be attributed to I^2R losses (grid). The relationship between reactive power and voltage can be determined by considering a two-bus system, as illustrated in the figure 5.1
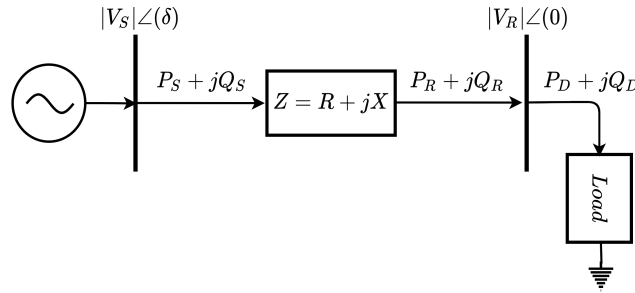
Figure 5.1: Line diagram of a two bus system

Where P_S, P_R, P_D are the active powers at the sending end, receiving end and load respectively. Similarly Q_S, Q_R, Q_D are the reactive powers at the sending end, receiving end and load respectively. Assuming the line to be a short line (just like in distribution lines), the receiving end active and reactive power can be written as,

$$P_R = \frac{|V_s||V_R|}{|z|}\cos(\theta - \delta) - \frac{|V_R|^2}{|Z|}\cos\theta \tag{5.1.1}$$

$$Q_R = \frac{|V_s||V_R|}{|z|}\sin(\theta - \delta) - \frac{|V_R|^2}{|z|}\sin\theta \tag{5.1.2}$$

Where θ is the impedance angle. Assuming the line to be highly resistive, to get the maximum receiving

end power, the Eq. (5.1.1) and (5.1.2) become,

$$P_R = \frac{|V_S||V_R|}{X} \sin\delta$$

$$Q_R = \frac{|V_s||V_R|}{X} \cos\delta - \frac{|V_R|^2}{X}$$

(5.1.3)

The reactive power equation in Eq. (5.1.3) can be further simplified by considering the δ to be small as power system normally operate in linear region in power angle curve.

$$Q_R = \frac{|V_R|}{X}(|V_S| - |V_R|) = \frac{|V_R|}{X}|\Delta V|$$

(5.1.4)

On rearranging the terms in Eq. (5.1.4), a quadratic equation will be obtained whose roots can be given as,

$$|V_R| = \frac{1}{2}|V_s| + \frac{1}{2}|V_S|\left(1 - 4 \times Q_R/|V_S|^2\right)^{1/2}$$

(5.1.5)

The Eq. 5.1.5 [37, 91] clearly gives the inverse relation between receiving end voltage and reactive power. Hence, if Q_D increases, the Q_R increases resulting in the decrease of receiving end voltage V_R. In general, the sending end voltage V_S is always maintained at the constant level. So, Q_R is the only variable affecting V_R. This principle is primarily used in reactive power control in PV system. As previously stated in the problem description, the PV system results in voltage rise problems due to reverse power flow. Therefore, the inverter control can be designed to absorb the reactive power to bring down the voltages at PCC.

5.2. Overview of reactive power control in inverter

One approach to reducing the PCC voltages is to employ PV power curtailment techniques where the MPPT is forced to operate at the non-optimal point. This method can control the voltages, but the PV modules operate at a capacity lower than their rated capacity. Hence it is a sub-optimal control, unlike reactive power control, as it enables PV systems to operate at their rated capacity during peak irradiaiton. The inverters' reactive power absorption/injection is restricted by the maximum current supported by semiconductor switches. Therefore, by increasing the rating of the inverter, the power handling capacity of the inverter increases. If the supply of PV power into the grid is less than the inverter's maximum capacity, the remaining capacity can be used for reactive power applications either for consumption or injection, depending on the necessity [6, 92–95]. For example Consider a photovoltaic system rated at 100 kilowatts (KW), which indicates that the maximum power generated by the photovoltaic modules is 100 kilowatts (at 1000 W/m^2 input irradiance). As a result, the inverter is rated at 100 KVA, with the entire capacity being used for active power. By increasing the inverter's rating by 10% to 110 KVA, the reactive power handling capacity increases to $\sqrt{110^2 - 100^2}KVAR = 45.6KVAR$ or 45.6% (figure 5.2 during peak penetration.
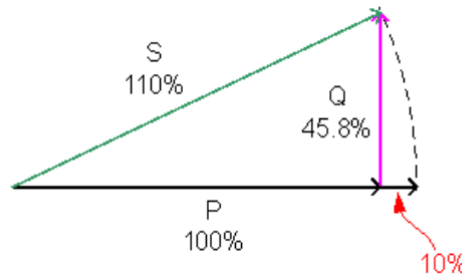
Figure 5.2: Increase in reactive power capability of inverter [6]

According to the Eq. (3.10.1), reactive power depends on two variables: I_q and V_q, which represent the quadrature components of grid current and voltage, respectively. Thus, either I_q or V_q, or both, must be non-zero in order to acquire reactive power. Designing the control can be tricky if both values are non-zero. As a result, either I_q or V_q must be greater than zero. There are two methods for establishing
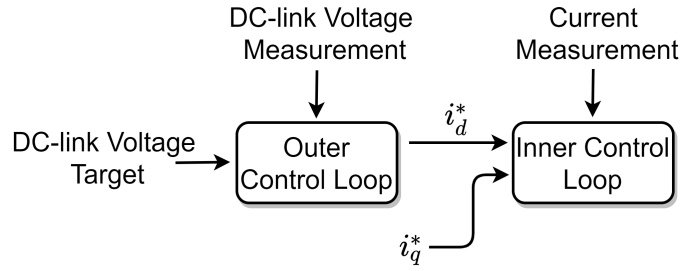
Figure 5.3: The point where i_q is fed

reactive power regulation. The first method generates a non-zero value for V_q by not aligning the d axis with the grid voltage space vector. As a result, the angle between the d axis and the space vector fluctuates with the degree of reactive power injected/absorbed. The alternative is to supply the inner current loop with a non-zero I_q reference current. The first technique is often more complex to realize than the second since it requires updating the PLL architecture, which is a challenging assignment. In contrast, the second strategy requires only slight modifications to meet the optimal performance level. Therefore the second approach is employed to reactive power control.
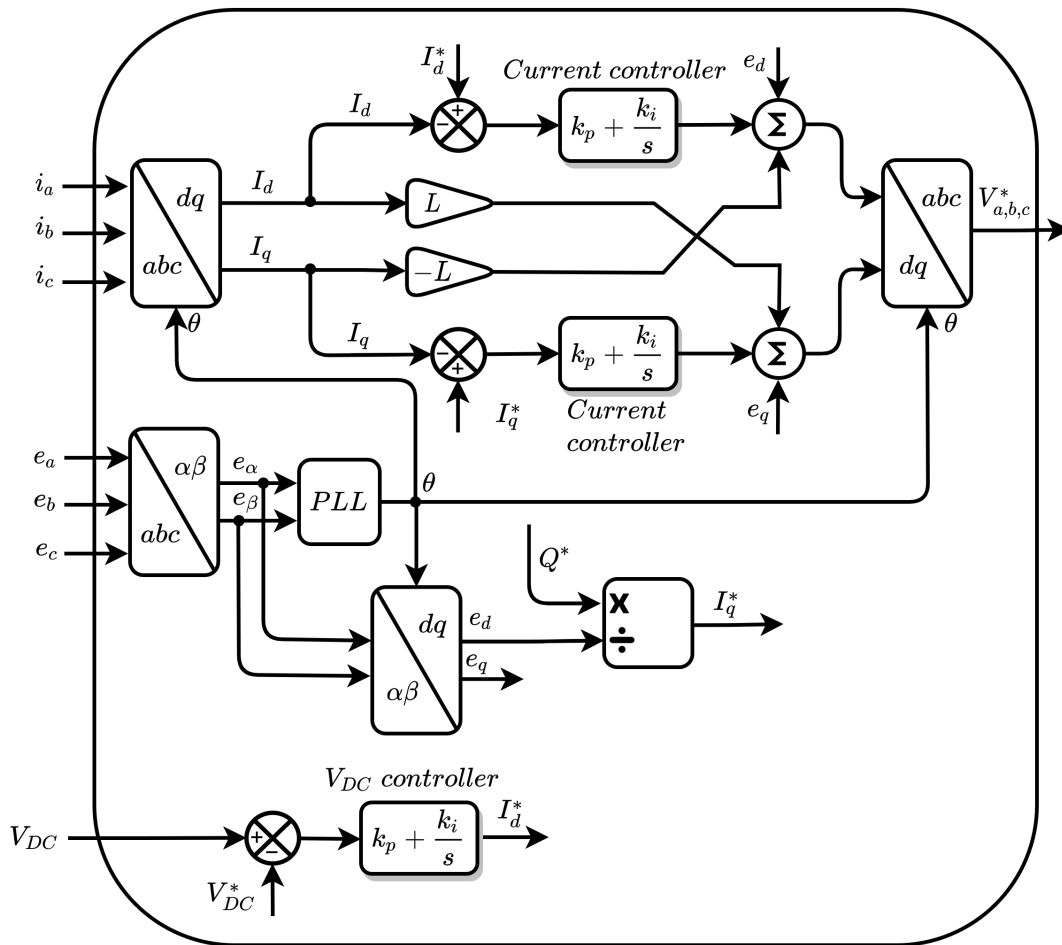
Figure 5.4: updated inverter control scheme with the reactive power reference

Figure 5.3 depicts the point where reference current i_q is fed. The updated reactive power equation in

per units is,

$$Q = e_d i_q \tag{5.2.1}$$

$$i_q = Q/e_d \tag{5.2.2}$$

The updated inverter control is illustrated in figure 5.4 where Q^* denote the reactive power reference that must be controlled by the inverter. The output of the inverter is connected to an inductor whose state variable is the current flowing through it. The state is something that can be controlled. The inverter's control attempts to control its output current, which is the same current flowing through the inductor. Now, there are two independent variables, amplitude and phase of the current, that can be controlled independently. Such control is possible as there are two decoupled current loops for I_d and I_q. Selection of I_d and I_q enables a selection of the amplitude and phase of the current. However, the amplitude is determined by the amount of power that is being pumped into the grid. So, I_d is dictated by the outer control loop for the maximum power transfer. Consequently, the phase of output current from the inverter is controlled by I_q. The generated output is in such a way that the current which is fed into the grid has the required phase angle with respect to voltage. The control of the phase accounts for the control of reactive power. So the current will be in such a way that it will have the desired phase difference with respect to the grid voltage and that phase difference determines the amount of reactive power being absorbed or injected. So the reactive power generation comes from the control mechanism itself.

5.3. REACTIVE POWER CONTROL METHODS

There are ample of reactive power control based voltage control methods are published in the literature [38, 39, 92–101]. This section discusses four most fundamental reactive power control strategies [39, 92, 93, 96–98] used in the thesis. In all of these techniques, active power resulting from the PV modules is not sacrificed. The four methods are-

- Constant power factor (PF)

- variable power factor (VPF)

- Reactive power absorption based on the voltage (Q(V))

- Constant reactive power absorption (CRP)

In the subsequent sections, each of the methods will be explained in great details.

5.3.1. CONSTANT POWER FACTOR METHOD (CPF)

As the name implies, the constant power factor approach maintains a constant power factor at the PCC regardless of the voltages recorded at the PCC. As a result, the reactive power is always proportional to the active power generated by the photovoltaic modules, as the Eq. (A.5.1) indicate. Thus, when there is inclement weather that results in low irradiance, the reactive power absorbed will be minimal since the PV power output will likewise be small. As a result, this technique eliminates the need to monitor PCC voltages.

$$\cos(\phi) = C \ (constant) \tag{5.3.1}$$

$$\phi = \arccos(c) \tag{5.3.2}$$

$$\tan(\phi) = Q/P \tag{5.3.3}$$

$$\tan(\arccos(C)) = Q/P \tag{5.3.4}$$

$$Q = \tan(\arccos(C)) * P \tag{5.3.5}$$
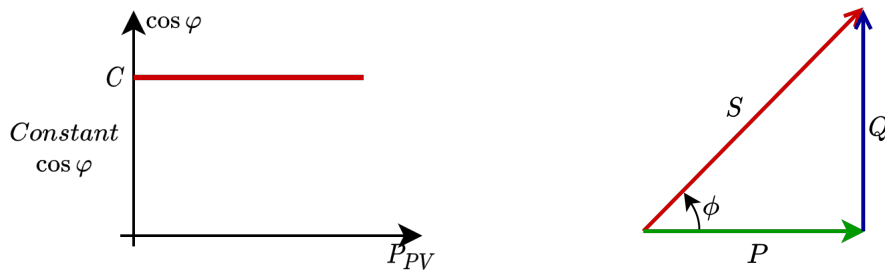
Figure 5.5: Constant $\cos\varphi$ reactive power method

The benefits of this method include ease of implementation, as no-load consumption data. Due to the fact that this method does not monitor the PCC voltages, the primary disadvantage is that the PV system consumes reactive power unnecessarily even when the voltages are between permissible limits (0.95 and 1.05 per unit). This could result in unintended additional losses. Figure 5.6 illustrates how this technique is implemented in the inverter control.
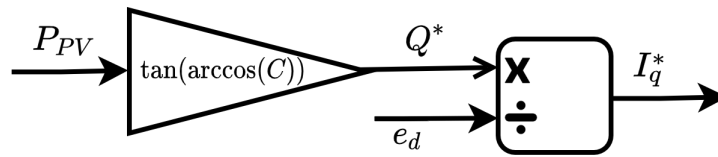
Figure 5.6: Implementation of constant PF in inverter control

5.3.2. VARIABLE POWER FACTOR METHOD (VPF)

In contrast to the constant power factor approach, the variable power factor control has a linear relationship with the power generated by the photovoltaic modules as depicted in the figure 5.7. The power factor does not remain constant throughout time. Thus, it is reduced during peak irradiance, as there is a potential of voltages at the PCC exceeding the prescribed limits due to significant PV power injection into the grid. The converse occurs at low irradiation levels. As with the constant PF technique, this technique eliminates the need to monitor PCC voltages. Figure 5.8 illustrates how this technique is implemented in the inverter control.

$$\cos\varphi = \begin{cases} C1, & P < P1 \\ \frac{C1-C2}{P1-P2}(P-P1)+C1, & P1 \leq P \leq P2 \\ C2, & P > P2 \end{cases} \tag{5.3.6}$$

$$Q = \tan(\arccos(C)) * P \tag{5.3.7}$$
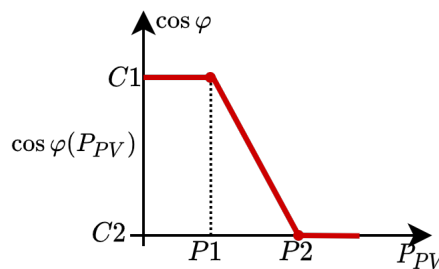
Figure 5.7: $\cos\varphi(P_{PV})$ reactive power method

Where $C1$, $C2$ are maximum and minimum power factors respectively and $P1$, $P2$ are minimum and maximum threshold limits of PV power produced, respectively. The variable PF approach has all of the benefits associated with the constant PF method, including ease of installation, as no load consumption data. Additionally, because the power factor is dynamically adjusted in response to the photovoltaic power, there will be no unnecessary reactive power consumption by the photovoltaic system. As a result, the power losses in this scenario are smaller than those in the constant PF technique.
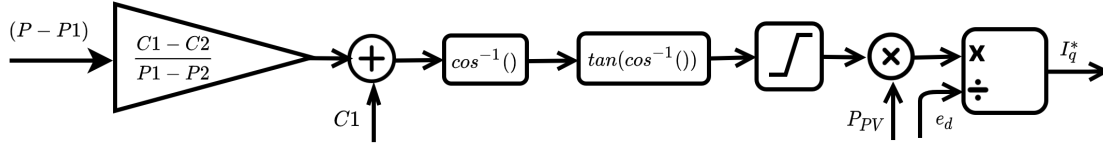
Figure 5.8: Implementation of constant VPF in inverter control

5.3.3. Reactive power absorption as a function of PCC voltage Q(V)

The solutions presented thus far implicitly maintain the voltage at PCC by utilising only PV power measurements as input. These strategies are built on the premise that the PCC voltage increases proportionally to the real power generated by the PV system, irrespective of changes in load. Even under these conditions, when irradiation levels are high, the voltage could only increase so far before hitting the threshold if the electricity demand, coincidentally, is at its peak. This technique takes into consideration the voltage at PCC, to implement the control, which is directly correlated to the generation and consumption of power in the vicinity. Consequently, in comparison to the first two approaches, the total reactive power consumption of the inverters can be drastically lowered. In that regard, weak voltage support is required which signifies that when the measured PCC voltages at the inverters are lower the reactive power absorption from these inverters is minimal. The reactive power follows a linear relationship with voltage, as shown in the figure 5.9. The Eq. A.5.3 are utilised to establish such a linear relationship. According to the formulae, the reactive power absorption steadily increases as the PCC voltages grow within a specific voltage interval. Figure 5.10 illustrates how this technique is implemented in the inverter control. The control is analogous to inverter droop control, in which the inverter's output voltage is linearly determined by the input reactive power.

$$Q = \begin{cases} Q_1, & V < V_1 \\ \frac{Q_2 - Q_1}{V_2 - V_1}(V - V_1) + Q_1, & V_1 \leq V \leq V_2 \\ Q_2, & V > V_2 \end{cases} \qquad (5.3.8)$$
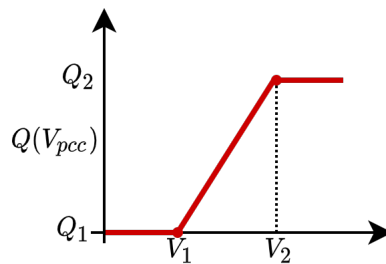
Figure 5.9: Reactive power absorption as a function of pcc voltage
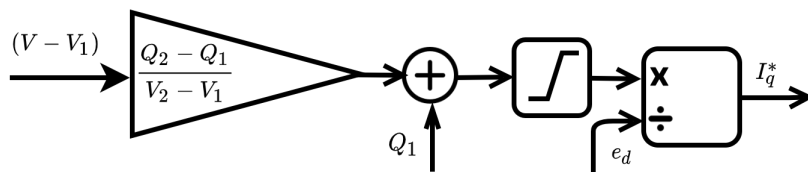
Figure 5.10: Implementation of $Q(V_{pcc})$ in inverter control

5.3.4. CONSTANT REACTIVE POWER METHOD (CRP)

When the voltages at PCC exceed particular threshold limits, the control is constructed so that the inverter absorbs constant reactive power as shown in figure 5.11. As a result, the inverter's reactive power control is strongly coupled to the PCC voltages. Thus, during the summer season, when irradiation is at its peak, the control detects when voltages above the optimal operation conditions and sends a signal to the inverter to absorb constant reactive power. The control, on the other hand, necessitates monitoring PCC voltages at the appropriate sample time. Additionally, because the inverter absorbs constant reactive power, this solution results in more considerable losses. Figure 5.12 illustrates how this technique is implemented in the inverter control.
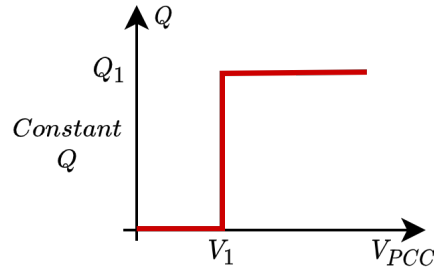
Figure 5.11: Constant reactive power method
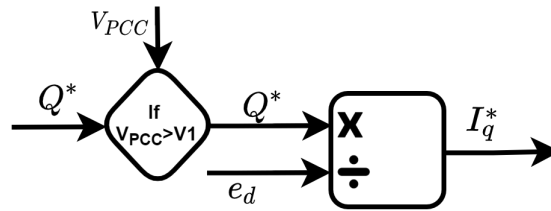
Figure 5.12: Implementation of constant reactive power method in inverter control

5.4. ELECTROLYSER AND BATTERY APPLICATIONS IN VOLTAGE CONTROL

Numerous reactive power control techniques have been explored thus far to maintain the voltages at the PCC. Unfortunately, these techniques could result in some technical losses (more on this later section). Active power control methods, on the other hand, could also be used to regulate the voltages. A distribution line's impedance characteristics indicate whether the voltages are more or less sensitive to active or reactive power flow. Low voltage distribution lines are, in general, more resistive than inductive in nature. As a result, the R/X ratio is rather high in comparison to the transmission line network [37–39]. As a result, the voltages at the buses are least influenced by the reactive power flow in the network. As a result, active power curtailment techniques, where PV modules are forced to operate at a non-MPPT point, are frequently employed in several published studies [33–35] to enhance controllability. On the other hand, Curtailment measures should be utilized rarely in the case of rooftop photovoltaic systems to maximize the utilization of the PV modules' capacity.

This is where energy storage technologies such as batteries and electrolyzers come into play. In energy storage devices, there is no concept of reactive power. They operate solely on active power flow. Batteries and electrolyzers can be configured to absorb excess power (more than the load consumption) generated by the PV systems by means of proper control mechanisms. In this manner, no energy is injected into the grid and is instead used by the household's storage elements. Two problems are addressed by adopting such active power-based voltage control techniques. One is the voltage increase problem, and the other is the losses suffered when reactive power control methods are used in place of active power control methods. In addition, batteries can be utilized to deliver electricity when demand is at its highest during evenings, and hydrogen produced by electrolysis could be used as a long-term energy-storing

fuel. Therefore, it seems there are no substantial problems associated with this method. However, the financial viability of employing batteries and electrolyzers is one of the key challenges. In most nations, battery prices are quite high, and employing electrolysers at homes does not appear to be practical at this moment.

In this thesis, electrolyzer/battery is modelled as a dynamic load and connected to the same PCC where PV system and load are connected as illustrated in the figure 5.13. The control has been designed so that the controller directs the additional power to the electrolyzer/battery when PV power exceeds load consumption. Two cases will be simulated. In the first case, all the reactive power control measures will be replaced with electrolyser/battery systems. In the second case, only at the two of the buses near the loads, the reactive power control methods are replaced by electrolyser/battery system. The results from the second case give a proper idea as to by what percentage the losses were reduced compared to the case where all the PV systems employ reactive power control methods.
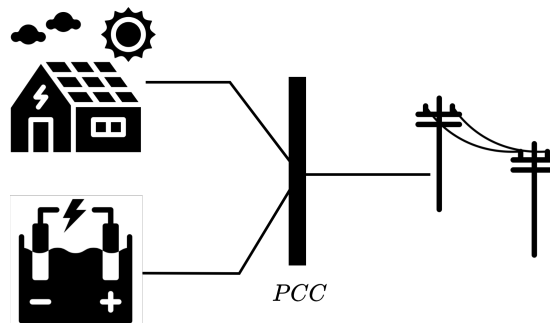
Figure 5.13: Electrolyser connected at the PCC

RESULTS AND DISCUSSION

This chapter presents the simulated results of all the methods that have been discussed in the previous chapter. Then, the chapter concludes with a brief discussion on the obtained outcomes. The figure 6.1 represents the base case, where multiple PV systems are connected without any voltage control strategies. In all the reactive power control strategies the sign convention followed is the power injection is considered to be positive, while absorption is considered to be negative.
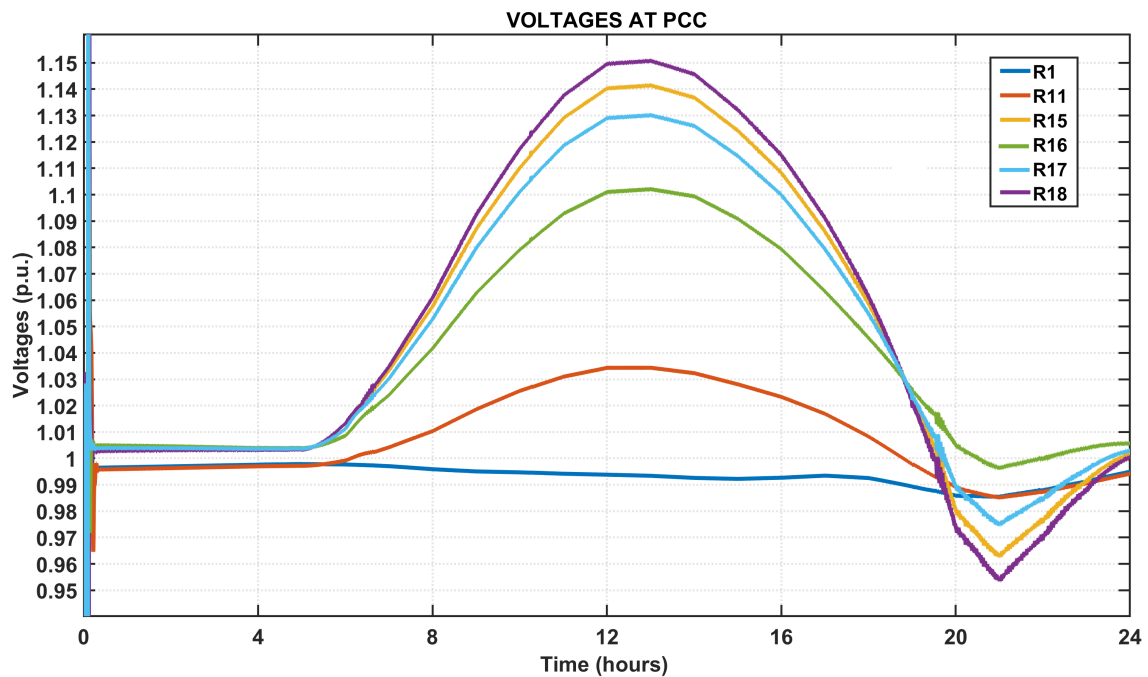
Figure 6.1: Voltage profiles across various load buses before implementing voltage control strategies

6.1. CONSTANT POWER FACTOR METHOD

To support the reactive power absorption, the inverter's rating is augmented by 20% in this method. In the constant power factor method, the power factor at PCC remains constant over time at 0.832, as depicted in the figure 6.5 to bring down the voltages below 1.1 p.u. The PF is registered as soon as the PV modules commence generating power. This could result in a small number of transients, as seen in the same figure. Because Q absorbed is directly proportional to the real power produced by the PV array (constant PF), Q is higher for higher-rated PV systems. As a result, the PV system connected to bus R18 absorbs significantly more Q as depicted in the figure 6.2. Because of reactive power absorption, the voltages are dropped down below 1.1 p.u (figure 6.3).
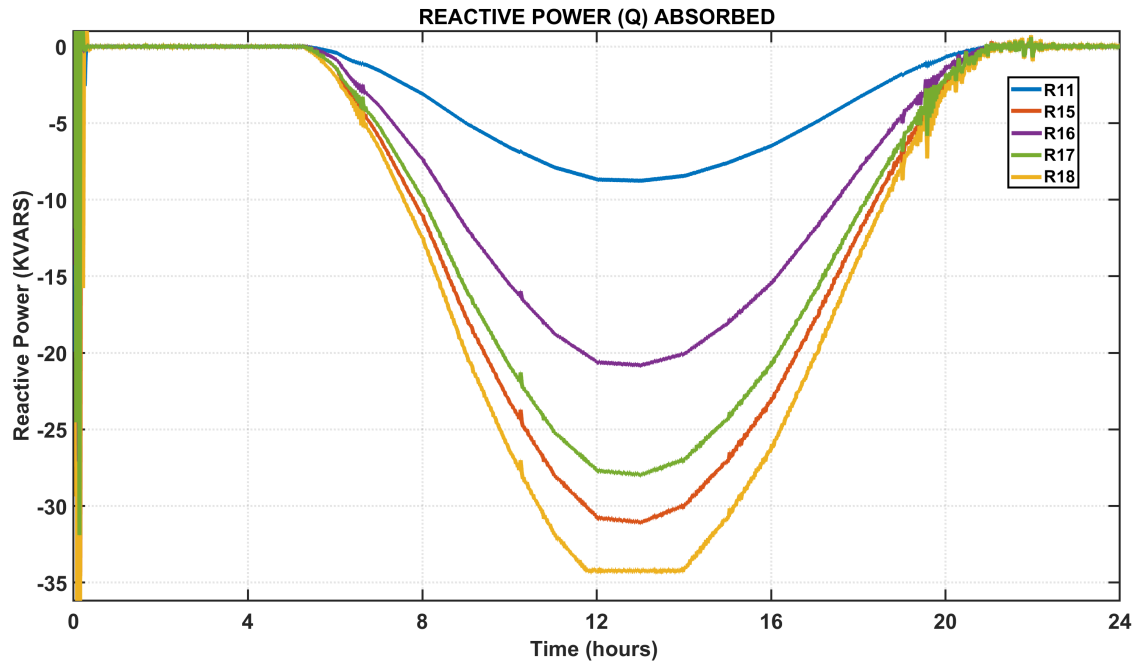
Figure 6.2: Reactive power absorbed by the inverters in CPF method
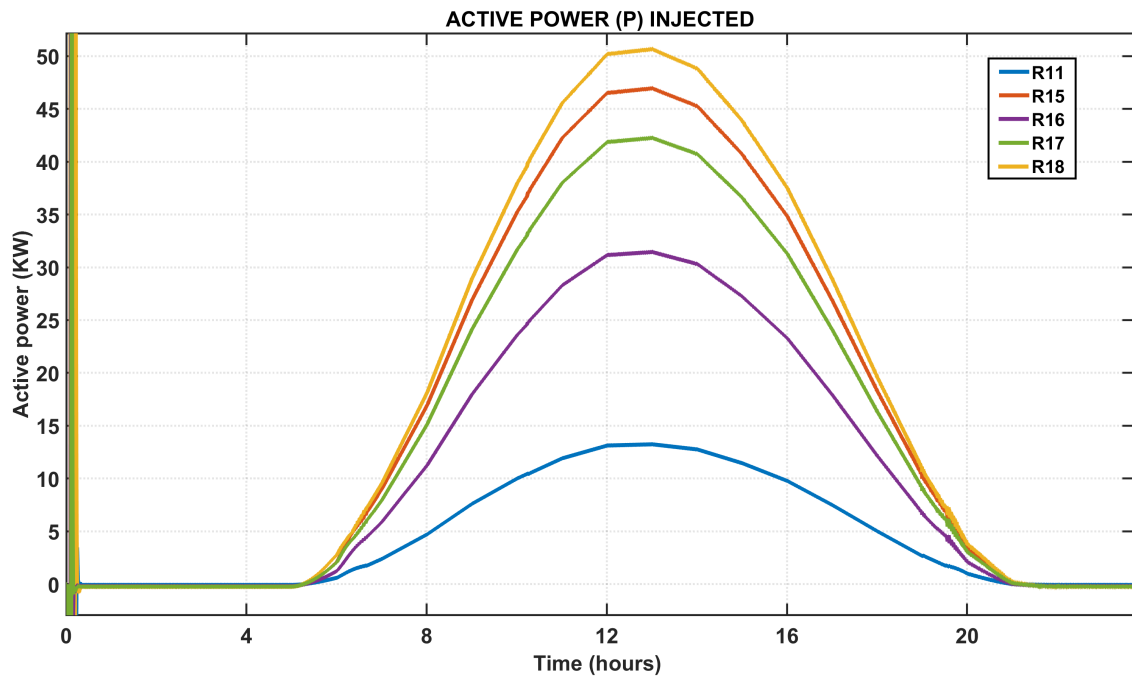
Figure 6.4: Real power injected in CPF method
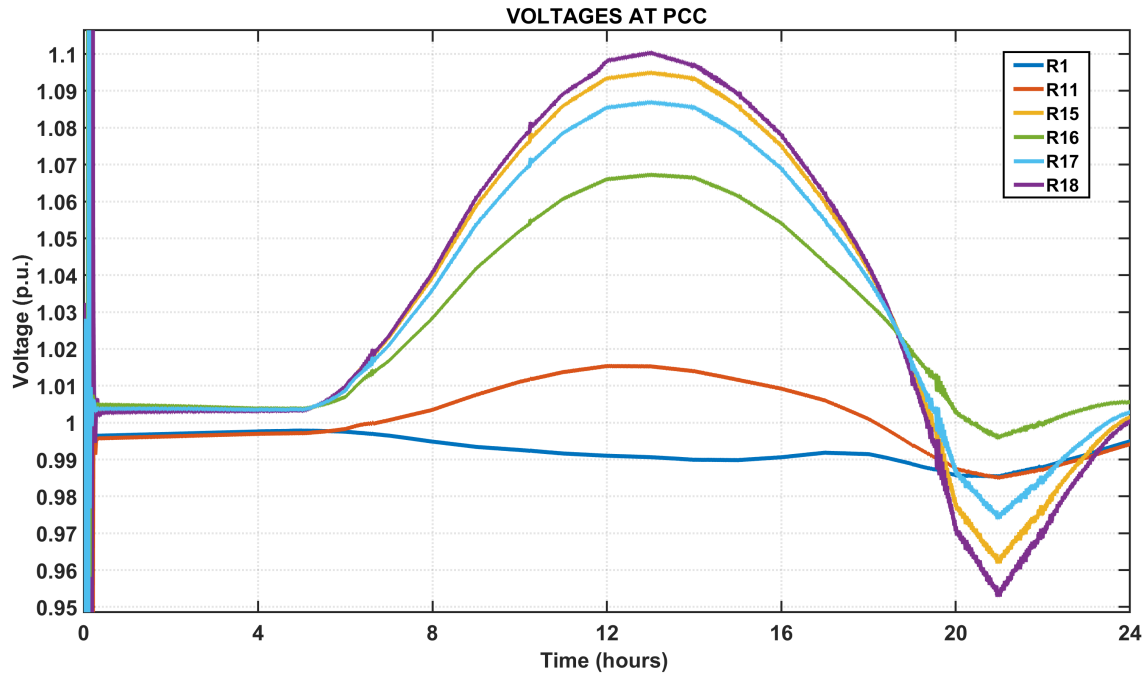
Figure 6.3: Voltage profiles obtained across various load buses in CPF method
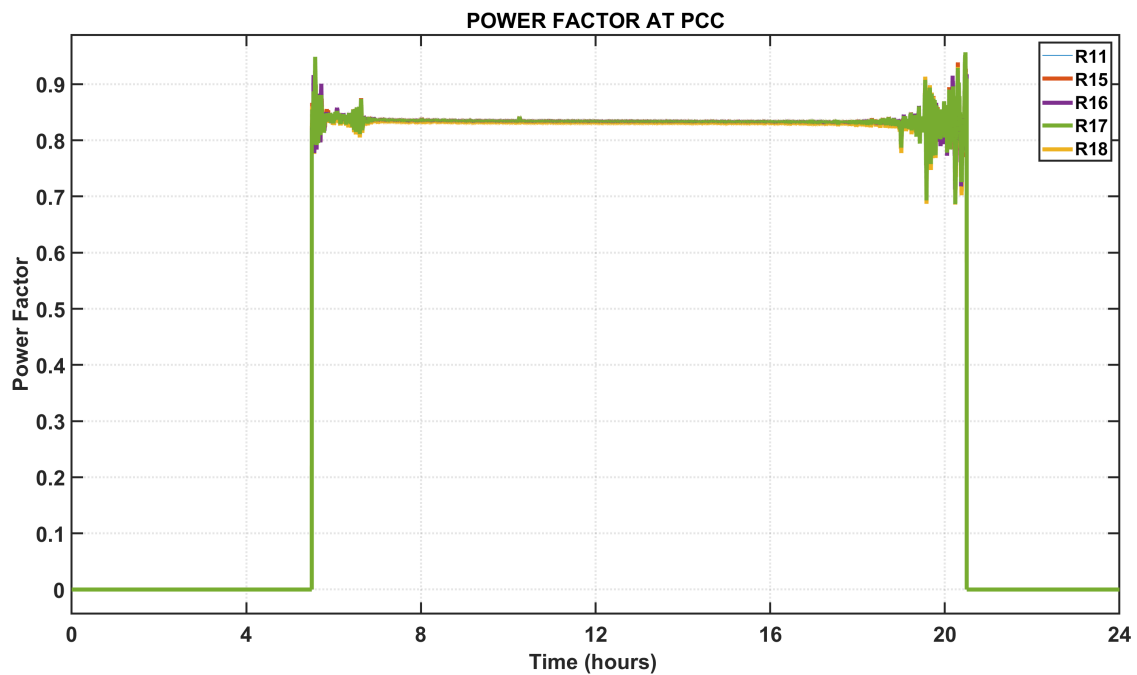
Figure 6.5: Power Factor measured at various PCCs in CPF method

6.2. VARIABLE POWER FACTOR METHOD

In this method all the invertes rating is increased by 20% except for the PV system connected to R18. Since the PV system connected to the bus R18 generates, comparatively, more power, the inverter rating has to be increased slightly above 20%. As previously stated, the variable power factor approach (VPF) differs slightly from the constant power factor method (CPF). In VPF, the power factor is assumed to have a linear relationship with generated real PV power. No two PV systems are the same in terms of their ratings. As a result, the slopes resulting from the linear relationship for each PV system are distinct.

As a consequence, the PV system with the highest rating has a greater slope in comparison. The detailed calculations of the parameters C_1, C_2, P_1, P_2 are given in the appendix. The figure 6.9 depicts the PF at PCCs. When there is no sunlight, the power factor is represented as zero, suggesting that no PV power is generated. Additionally, this control is designed to initiate absorbing reactive power when the real power supplied equals 35% of the maximum photovoltaic power output. Consequently , once they reach this threshold, the power factor begins to fall. Therefore, the reactive power absorption begins to rise from this point as shown in the figure 6.6. The corresponding voltage curves are presented in the figure 6.7. The voltages at all the PCCs are below 1.1 p.u. The real power injected is shown in the figure 6.8.
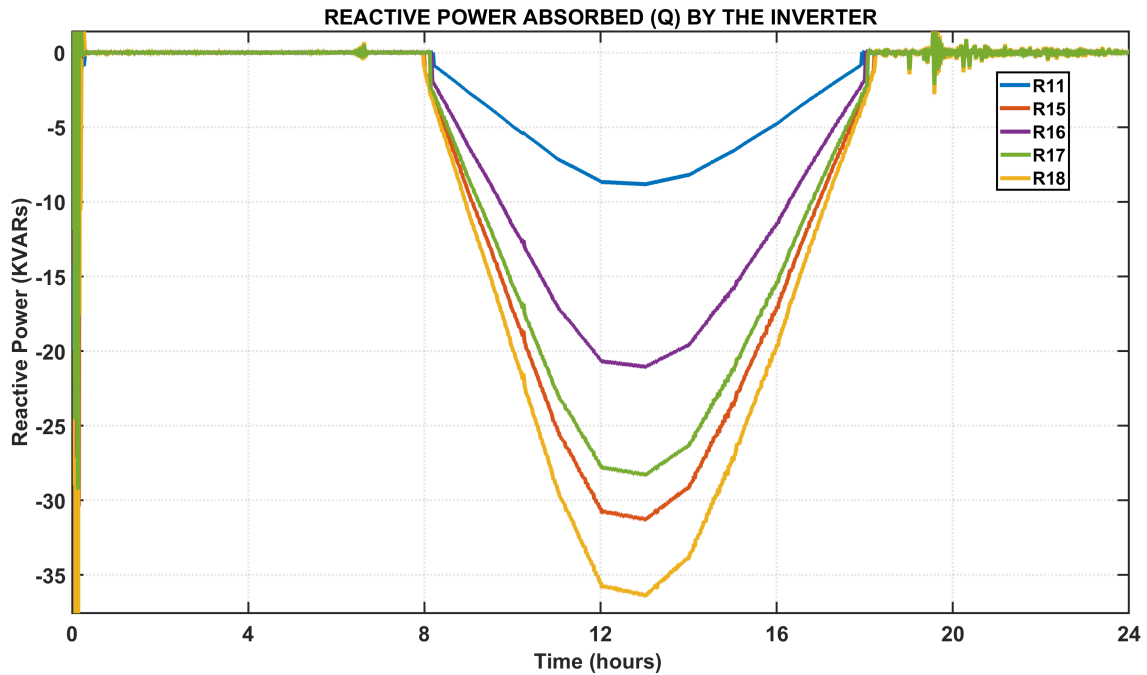
Figure 6.6: Reactive power absorbed by the inverter in VPF method
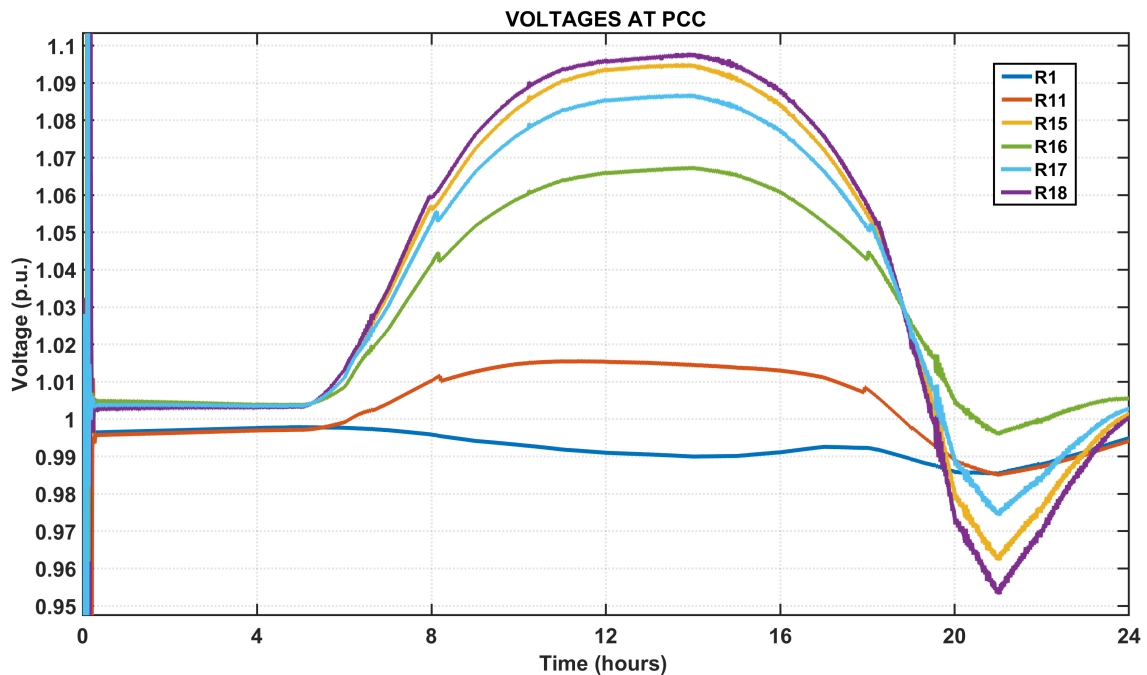
Figure 6.7: Voltage profiles obtained across various load buses in VPF method
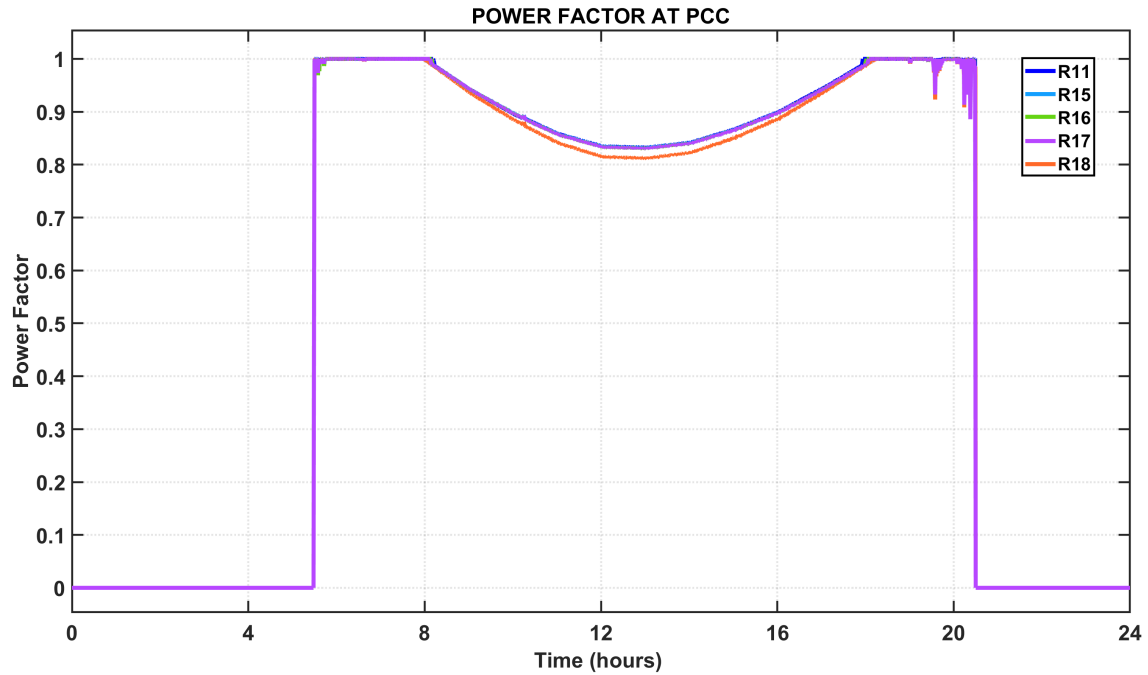
Figure 6.9: Power Factor measured at various PCCs in VPF method
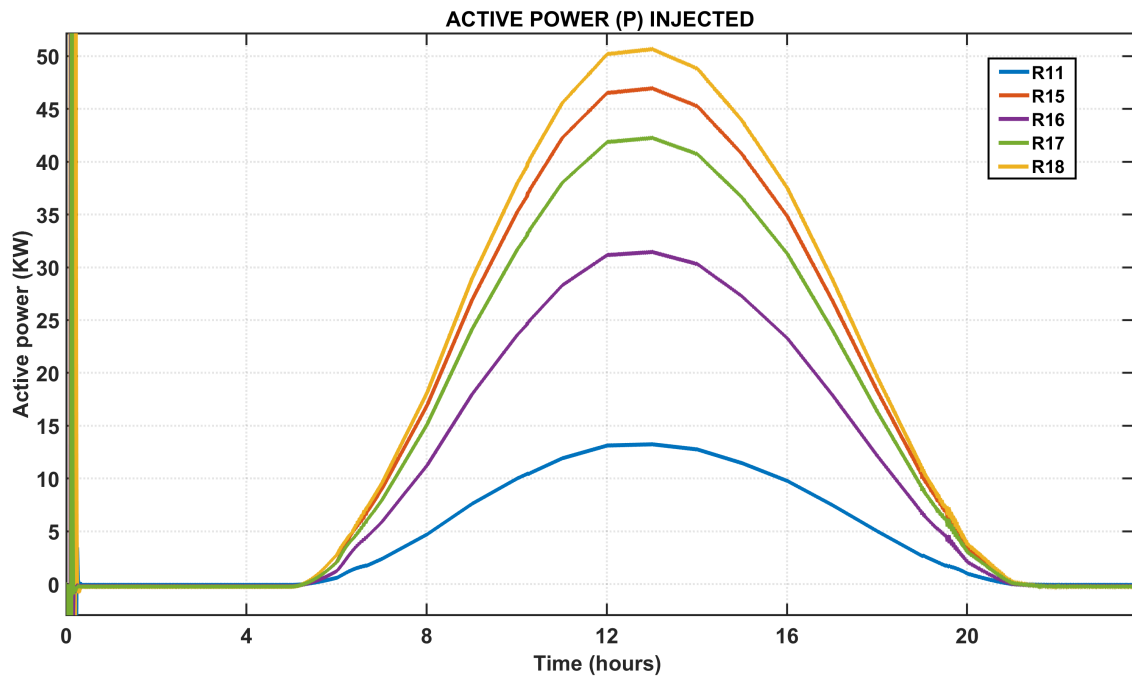
Figure 6.8: Real power injected in VPF method

6.3. REACTIVE POWER AS A FUNCTION OF VOLTAGES AT PCC

Both methods, constant Q and Q(V), are similar as they can be designed to absorb reactive power only when voltages surpass a specified threshold. This number is considered as 1.05 p.u. in Q and Q(V) techniques. Similar to VPF approach, the Q(V) method establishes linear correlations between PCC voltages and reactive power consumption, as illustrated in the figure 6.13. The slopes in that figure are chosen in accordance with the maximum reactive power that an inverter can sustain in a photovoltaic

system, analogous to the VPF approach. The detailed calculations of the design parameters V_1, V_2, Q_1, Q_2 are given in the appendix. When voltages exceed 1.1 p.u., the grid's highest permissible voltage level, the reactive power absorption is maintained constant at the inverter's maximum capacity. The figure 6.11 shows that, even this method successfully maintains voltages in limits. The amount of resulting reactive power consumed and active power injected are shown in the figures 6.10 and 6.12 respectively. The inverters rating is increased by 20% in this method as well.
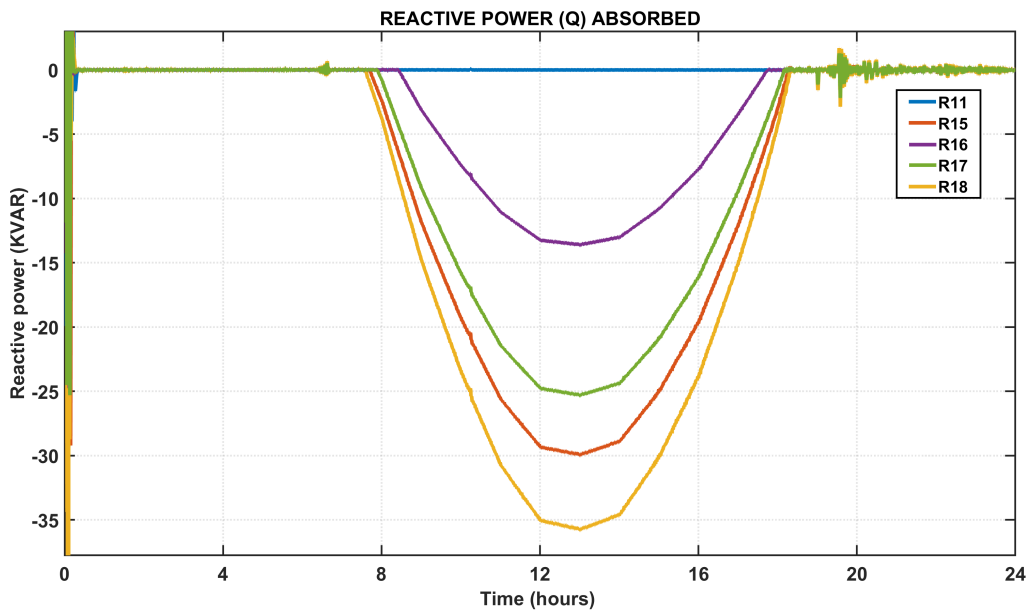
Figure 6.10: Reactive power absorbed by the inverters in Q(v) method
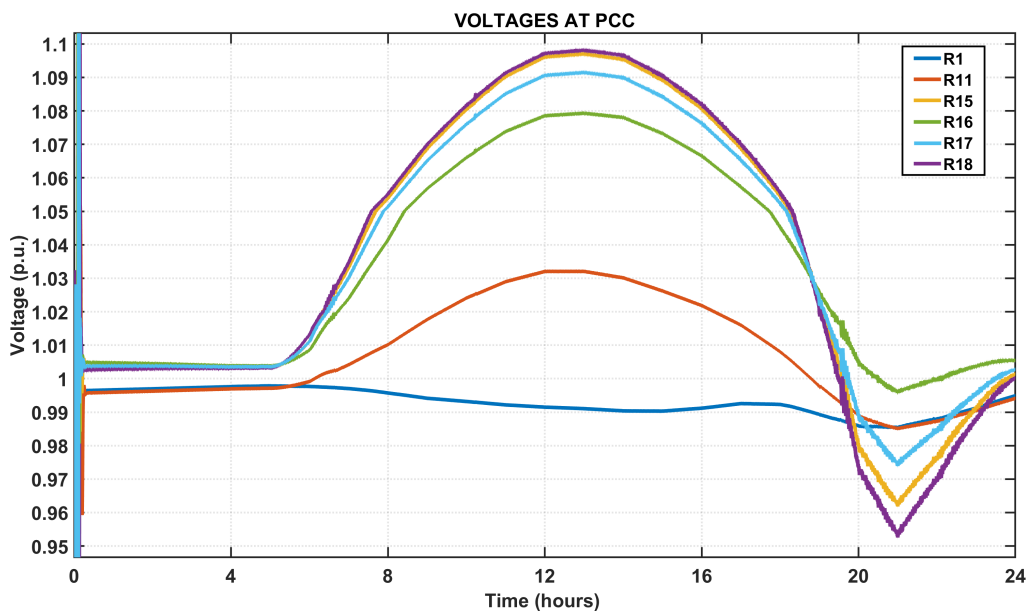
Figure 6.11: Voltage profiles obtained across various load buses in Q(V) method
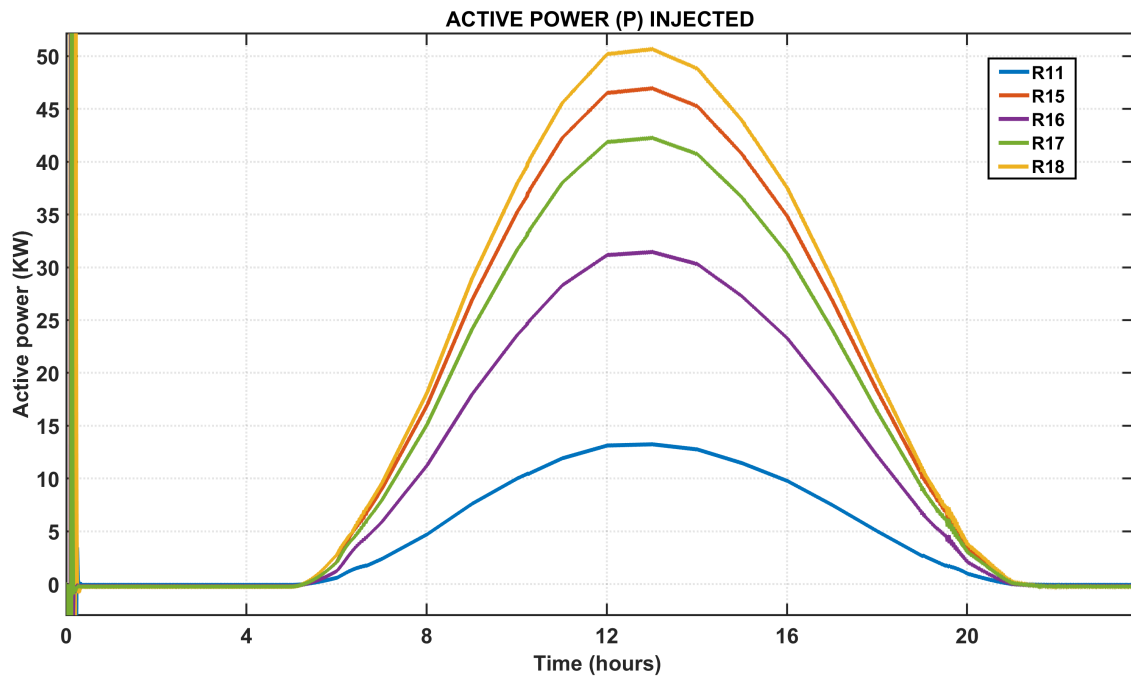
Figure 6.12: Real power injected in Q(v) method
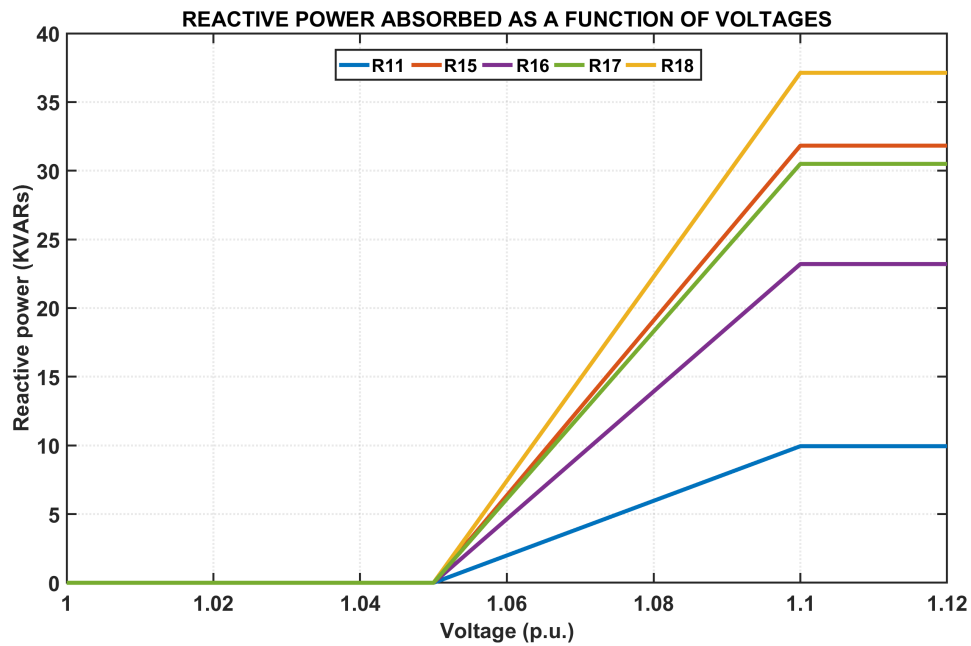
Figure 6.13: Relation between reactive power absorbed and the voltages at PCC

6.4. CONSTANT REACTIVE POWER METHOD

It has already been mentioned that both the Q(V) and Q have a significant controllability advantage over the other two approaches since they may be programmed to absorb reactive power only when voltages surpass a predetermined threshold. This number is considered to be 1.05 p.u. The reactive power consumption is kept constant, for a given PV system, at the maximum amount of reactive power the inverter is capable of handling during peak irradiance in order to bring down the voltages below 1.1 p.u, however, between the PV systems the maximum reactive power consumed varies according to the rating of the photovoltaic system. Therefore the PV system connected to bus R18 absorbs significantly more Q. The figure 6.14 eloquently illustrates these aspects. The resulting voltage curves are shown in 6.15. Corresponding active power injected is illustrated in the figure 6.16. Similar to all the previous methods, the inverter rating is increased to 120% of the original, to accommodate the reactive power absorption.
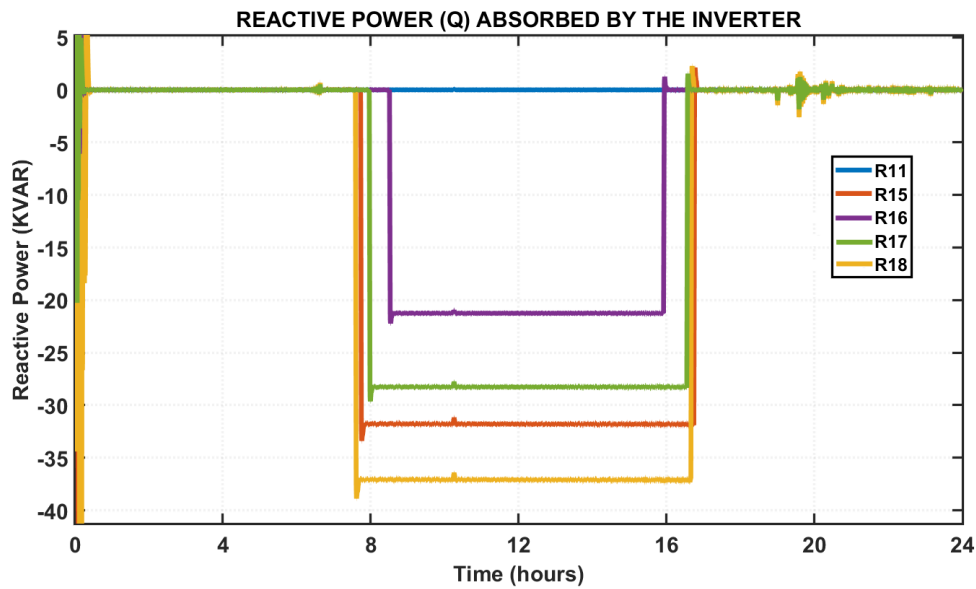
Figure 6.14: Reactive power absorbed by the inverters in CRP method
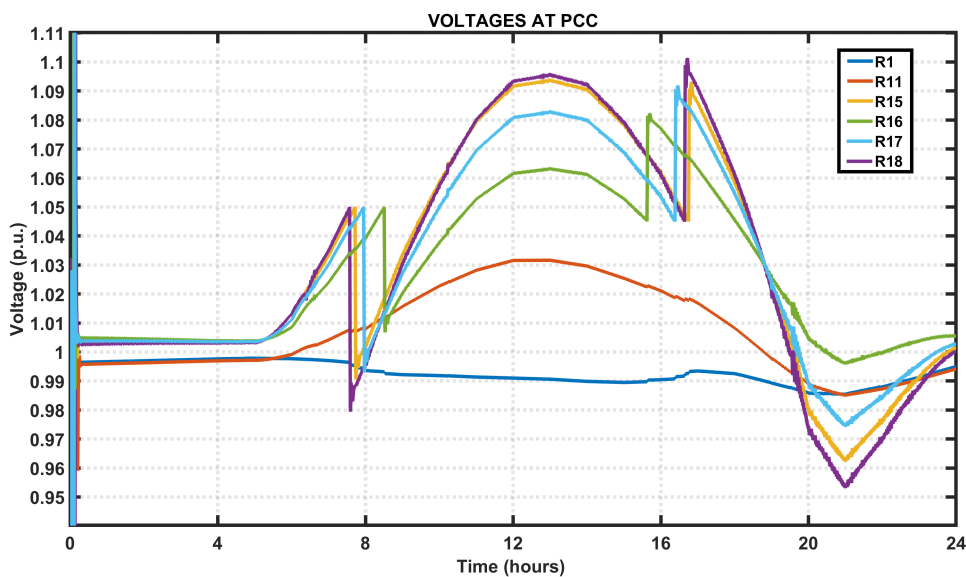
Figure 6.15: Voltage profiles obtained across various load buses in CRP method
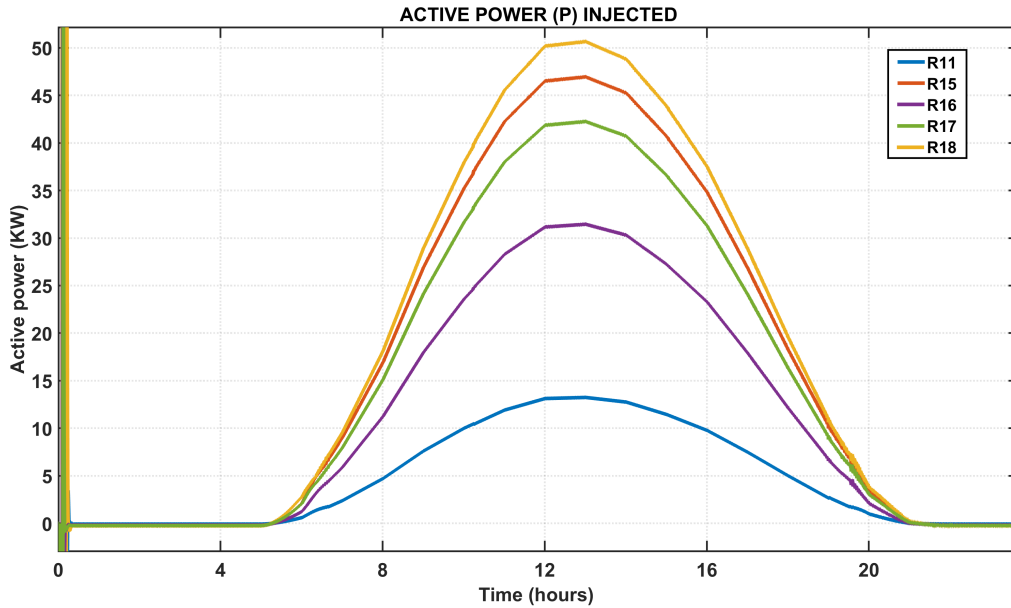
Figure 6.16: Real power injected in CRP method

6.5. Electrolyser/Battery system

When coupled to rooftop photovoltaic systems, electrolysers/batteries can assist in sustaining grid voltage. The figure illustrates PCC voltages when an Electrolyser / Battery System substitutes for all reactive power control measures at each load. When the photovoltaic energy generated exceeds the loads', the surplus is absorbed by the electrolyser/battery. Due to the fact that no power is injected into the grid, the voltages at PCC remain strictly at one volt per unit until the load starts to accept power from the grid. This occurrence is depicted in the figure 6.18. The figure 6.17 illustrates the surplus power consumed by the electrolyser/battery systems. Since the irradiance and load profiles of all PV systems and loads are identical, the voltage reaches one p.u precisely at the exact moment. Also, during the early hours, the voltages rise slowly because the PV power gradually increases and eventually matches the loads' consumption.
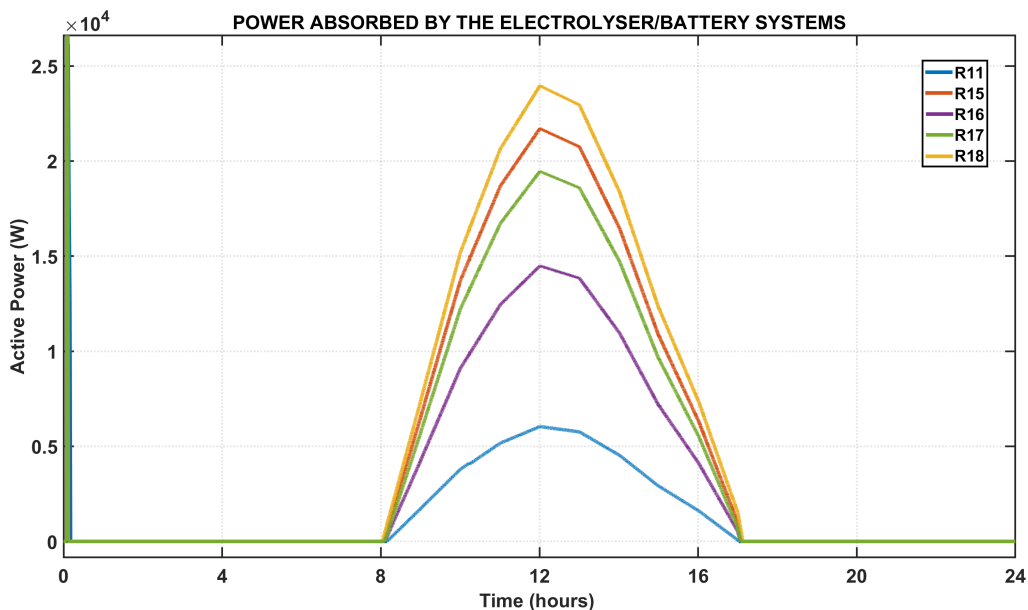
Figure 6.17: Real power absorbed by the electrolyser/battery systems
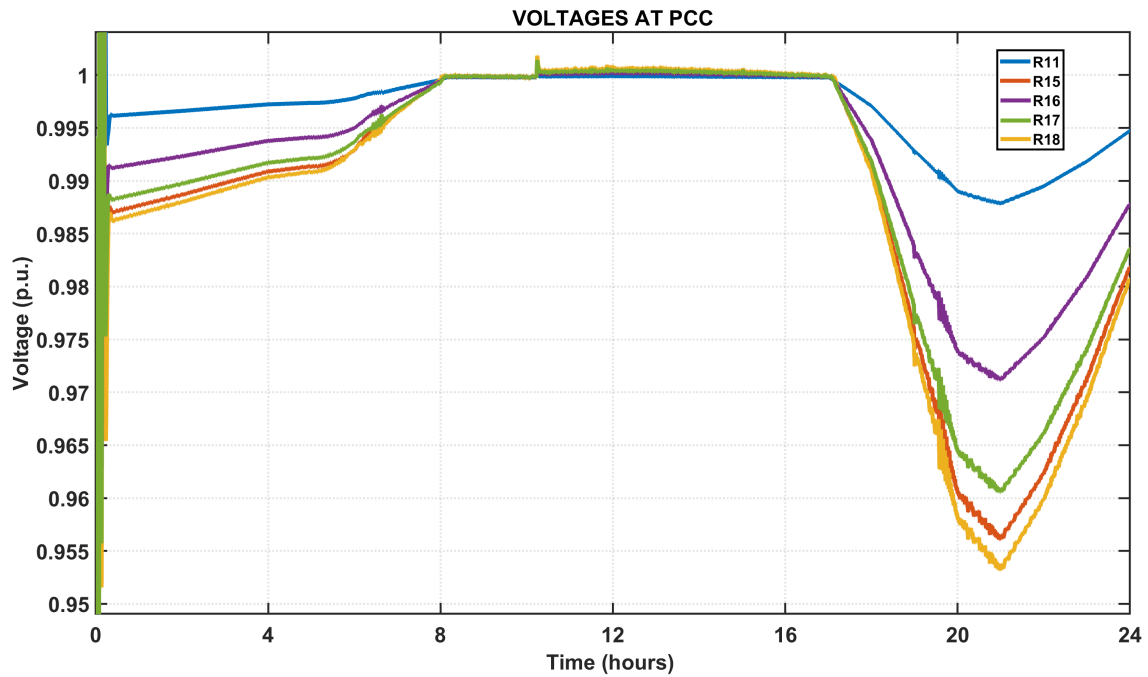
Figure 6.18: Voltage profiles obtained across various load buses for the case 1

In the second scenario, where the reactive power regulation methods have been replaced with an electrolyser/battery system exclusively on the two buses R17 and R18, the voltage curves are as indicated in the figure 6.19. As a result, the voltages across R17 and R18 remain unchanged at one p.u during peak irradiance, analogous to the earlier case. Voltage spikes on the remaining buses as a result of PV penetration into the grid.
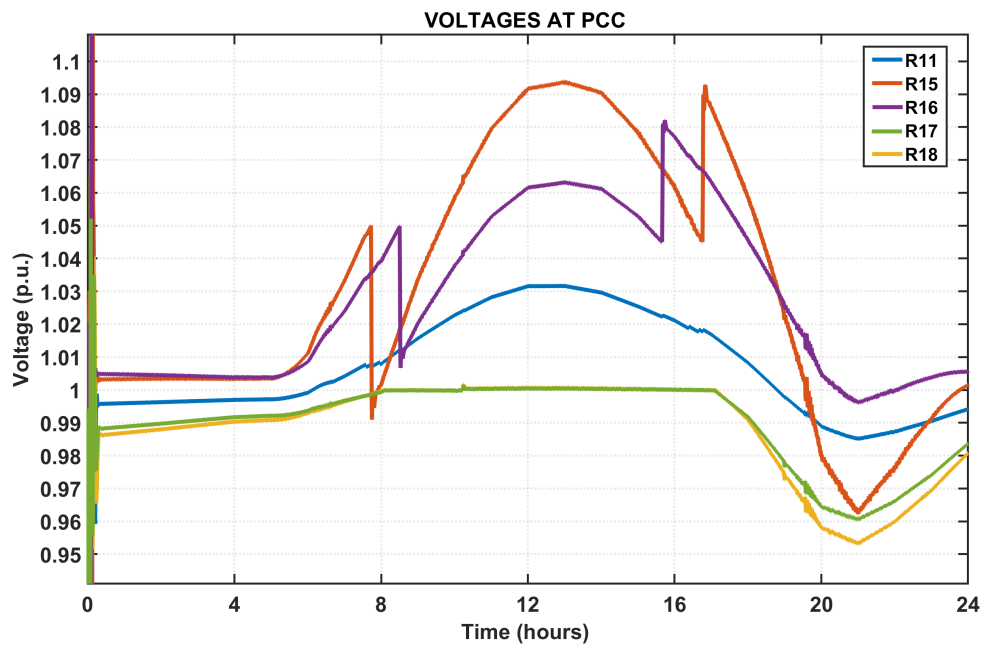
Figure 6.19: Voltage profiles obtained across various load buses for the for the case 2

6.6. DISCUSSIONS

In the preceding section, the results of all reactive power control approaches have been published. Each technique is distinctive in its own way, although they all share some overlapping characteristics. For example, with the exception of the constant reactive power technique, the reactive power absorbed in all control methods takes the same shape as shown in the figures 6.2, 6.6 and 6.10. The voltages at the bus R18 is highest in all the methods because the PV system's rating connected at that bus is maximum and also due to the fact that the line impedance is maximum when viewed from the bus R18. This is why the reactive power consumption is the highest PV system connected to that bus. Similar explanation can be given to the other buses as well. Also, no reactive power is absorbed at bus R11 in both the Q and Q(V) methods because the voltage at the corresponding PCC has never reached 1.05pu, as illustrated by the voltage curves in the figure 6.15 and 6.11. All reactive power control techniques are designed to maintain peak penetration regardless of reactive power(Q) consumption. Therefore, these control strategies should not influence the PV system's maximum PV power injection. The active power injected is thus utterly identical in all techniques, as observed in the figures 6.4, 6.8, 6.12 and 6.16. Hence, no PV power is curtailed to bring down the voltages below 1.1 p.u.

So far, the advantages of the methods have been discussed. All the methods have successfully kept the voltages under 1.1 p.u. By doing so, a significant amount of reactive power has been introduced into the system. Having more power in the system could always result in more losses in the grid. Due to the presence of more reactive power in the system, the total current or, in other words, the RMS value of the current in the system increases. The distribution lines are inductive and resistive in nature. They offer impedance to the current flowing through them. Moreover, the R/X ratio is higher in distribution lines. Consequently, the system suffers increased I^2R losses. Losses due to reactive power for all the control strategies are calculated and presented in the figure 6.20. These methods are compared with the base case, where electrolyser/battery systems are used as they do not cause any additional losses.
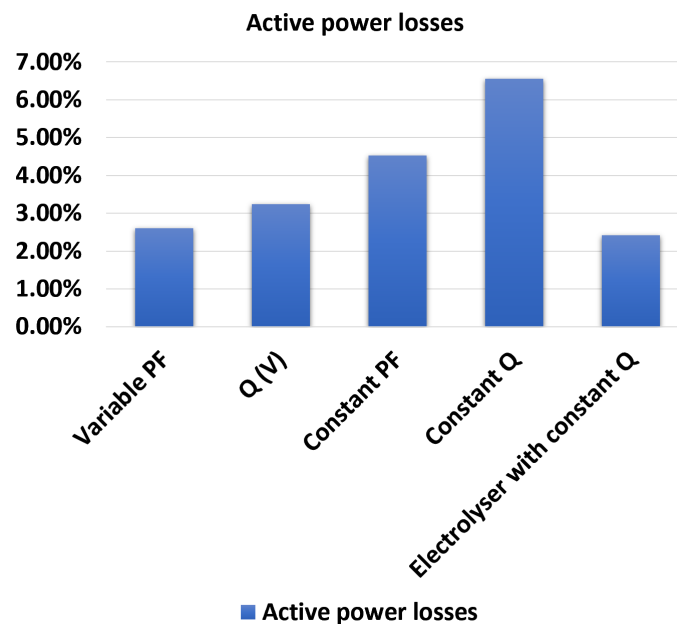
Figure 6.20: Losses due to reactive power consumption

From the figure 6.20, it is clear that the constant Q and constant power factor methods cause more losses when adopted. It does make sense because even during the minimal requirement of reactive power, the inverter is forced to consume significantly more reactive power. This is the case when the PCC voltages just reach the lower threshold limit (1.05 p.u.). Whereas, in VPF and Q(V) methods, the losses are lower as the reactive power is gradually absorbed. Nevertheless, that does not explain why VPF method offers lower losses than the Q(V) method even when the reactive power absorbed by the

pv system connected to the bus R11 is zero. Also, it has been mentioned multiple times that the Q(V) method is better than the VPF as it directly monitors the voltages. Even so, VPF surprisingly caused lower losses. The possible occurrence of such a phenomenon is due to the fact that the design parameters such as the slopes and threshold limit in both techniques are not chosen semi-optimally. For example, in the VPF method, if the control has been configured in such a way that it starts absorbing Q at 25% rather than at 35% of the PV system rating, then the control may absorb more reactive power and causes even more loss than Q(V) method. A rigorous approach of optimally choosing the design parameters is presented in the next chapter. The use of an active power voltage control strategy could decrease the losses incurred significantly. When the constant Q max control method is used in conjunction with the battery/electrolyser systems, the losses are reduced less than 50%, as shown in the last bar chart.

7

CONCLUSIONS

This chapter describes the final conclusions drawn from the findings of this thesis. Additionally, the limitations and future recommendations are discussed in detail.

7.1. CONCLUSIONS

The primary objective of this study is to achieve 100% PV penetration in a low voltage distribution network while maintaining voltages within the grid constraints. With a rising number of PV systems connected to LV grids, there will be a significant amount of reverse power flow, particularly as PV power penetration increases. This reversal of current flow may cause a variety of power quality issues, including an increase in voltage along the feeder. To avoid such an increase in voltage above the grid limit, numerous voltage control schemes based on active and reactive power control techniques have been employed. The European low-voltage distribution benchmark network built by CIGRE was chosen for penetration research because of its relatively simple architecture (and hence easier to model), support for DER integration, and availability of network-related data. The various components of the photovoltaic system have been meticulously designed in accordance with the PV systems' capacity. For inverter control, a voltage-oriented control mechanism is implemented, in which the amount of current injected into the grid is controlled by maintaining a constant voltage at the DC-link capacitor. This in turn regulates the amount of active and reactive power delivered to/absorbed by the grid.

The designed PV systems is connected to the grid to perform PV penetration studies. The PV penetration is defined as the ratio of the peak PV power production to the peak load power consumption over a particular period, a day in this case. The PV systems have been constructed in such a way that the maximum power generated by the modules at peak irradiation is equal to the maximum power consumed by the loads on a given day. This is done to determine whether the chosen network can support 100 percent PV penetration without exceeding grid voltage constraints (0.95 and 1.1 p.u.). The results suggest that the network is perfectly capable of achieving 100 percent photovoltaic penetration. However, as the length of the LV network is increased, the voltage rises more rapidly due to the network's higher resistance and inductance. Therefore, to simulate such an event, the length of the residential subnetwork has increased in several increments from its initial length to twenty times its original length. The results, just like the theory, clearly demonstrates such voltage increase phenomena at the points of common coupling (PCCs) when the distance between the load and the source increases. For a distance of 20 times the original length, the voltage at bus R18 reaches around 1.15p.u. Nonetheless, for the commercial and industrial subnetworks, even with enormous feeder lengths, the tremendous surge in voltages near the PCCs do not occur. This is due to the fact that the peak load consumption of commercial and industrial loads coincides with the peak PV power generation. Consequently, there will be little or no power flow into the grid. Hence, penetration levels could be at their maximum. Because of this reason, commercial and industrial subnetworks are excluded from voltage control studies.

To alleviate the voltage rise problem, the penetration levels must be drastically reduced to decrease the reverse power flow. The results indicate that when the residential feeder length is increased to twenty times the initial length, the PV penetration decreases to 65 percent. In other words, a penetration level of 65 percent ensures that the voltages at the PCCs remain within grid voltage restrictions. This particular scenario has been chosen to demonstrate the application of voltage control techniques in order to maximise the penetration of photovoltaics to 100 percent.

Two strategies have been used to improve pv penetration. The first category is reactive power control methods, whereas the second category is active power control methods. In the first method, the reactive power is absorbed by the PV system so that voltages at the PCCs are within the grid voltage limit. The second way is based on active power control, in which the voltages are controlled by a battery/electrolyzer. Four different reactive power control strategies have been implemented. They are summarised as follows-

- Constant power factor (PF)

- variable power factor (VPF)

- Reactive power absorption based on the voltage (Q(V))

- Constant reactive power absorption (CRP)

All of these solutions have been simulated on the residential network, and the results demonstrate that they are effective at keeping voltages under limits even with 100 percent PV penetration. Additionally, the active power injected in each of these techniques is identical. As a result, it can be inferred that the four reactive power control approaches described above are capable of increasing PV penetration to 100

In the second approach, where batteries/electrolysers are utilised, the control has been constructed in such a way that when PV power exceeds load consumption, the controller redirects the excess power to the electrolyzer/battery. Two cases are simulated. In the first case, all the reactive power control measures will be replaced with electrolyser/battery systems. In the second case, only at the two of the buses near the loads, the reactive power control methods are replaced by electrolyser/battery system. The simulated results reveal that the voltages at PCC remain strictly at one volt per unit because no power is injected into the grid. Hence, these methods also proved to increase PV penetration to 100%.

Due to the presence of more reactive power into the system by various reactive power control methods, the total current or, in other words, the RMS value of the current in the system increases leading to increased I^2R losses. These losses are calculated and compared with the base case, in which electrolyser/battery systems are used. as they do not cause any additional losses. The results show that the CRP method introduces more losses comparitively because even during the minimal requirement of reactive power, the inverter is forced to consume significantly more reactive power. VPF method surprisingly cause lower losses than Q(v) method even though it is superior. This is because of sub-optimal design of the control paramters. An in depth way to design these paramters will be discussed in the next section.

Low voltage distribution lines are, in general, more resistive than inductive in nature. As a result, the R/X ratio is rather high in comparison to the transmission line network. Therefore, the voltages at the buses are highly influenced by the active power flow in the network than the reactive power flow. As a result, batteries/electrolyser systems are more effective way of controlling voltages at the PCCs. All the reactive power techniques are barely able to maintain the voltages under 1.1 p.u beacuse the voltages are not highly responsive to the reactive power flow. On the other side, the battery/electrolyser systems maintain voltages exactly at 1 p.u which is the optimal point. By doing so, they donot even cause additional losses since no reactive power is being introduced in to the system. Additinally, batteries can be utilized to deliver energy when demand is at its highest during evenings, and hydrogen produced by electrolysis could be used as a long-term energy-storing fuel or for hybrid cars and fuel cell cars in future. So, the batteries and electrolysers not only solve the problem but also offer additional advantages.

To conclude, both the active and reactive power control methods can be used to increase the PV penetration to 100%. However, active power control techniques like batteries/electrolyzer systems provide better value in terms of effectiveness in solving the voltage rise issue.They also offers lower losses, and multiple-use cases.

7.2. FUTURE RECOMMENDATION

Achieving an efficient overall performance level requires careful attention to design factors, especially the values of C1, C2, P1, and P2 in the VPF method, and V1, V2, Q1, and Q2 in the Q(V) method. The

tuning of these design parameters in this project is semi optimal. Increased losses owing to unnecessary reactive power consumption could emerge from such a design flaw. As a result, an appropriate procedure for determining such parameters must be devised and made a standard. This chapter will explore one of these procedures briefly.

7.2.1. VOLTAGE SENSITIVITY ANALYSIS

In any system, it is just not sufficient to obtain the crucial point of operation. It is also vital to understand how various operating factors influence this critical point. Information on characteristics and controls that can affect a system's performance should be collected to comprehend the sensitivity to a particular variable. Incorporating sensitivity analysis in the design process is the key to developing efficient systems. The voltage at any bus is sensitive to the active and reactive power flowing through the bus. Voltage sensitivity analysis determines the extent to which the active and reactive power passing through a bus influences the voltage at that bus. As a result, it can identify the most efficient regions for reactive power regulation. This information is valuable for determining the control settings and the volume of minimal reactive power expected to maintain the voltages within limits with . The voltage sensitivity at a bus, to the active and reactive power fluctuations can be determined using power flow solutions. The generated matrices could highlight the strategic locations to consider the voltage support either through active or reactive power regulation. The load flow equations for a two bus distribution line are Eq. (7.2.1) and Eq. (7.2.2) [93] . These two equations are iteratively solved using newton-raphson or gauss sidel methods to obtain the system Jacobian matrix (Eq. **??**. The inverse of the jacobian matrix yields the voltage sensitivity matrix.
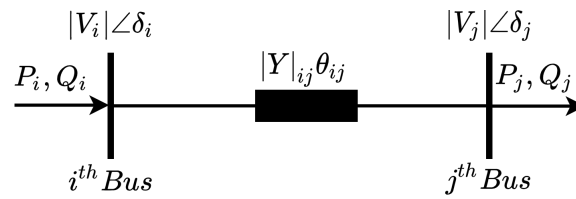
Figure 7.1: Two bus network

$$P_i = |V_i| \sum_{j=1}^{n} |V_j| |Y_{ij}| \cos\left(\theta_{ij} - \delta_i + \delta_j\right)$$
$$Q_i = -|V_i| \sum_{j=1}^{n} |V_j| |Y_{ij}| \sin\left(\theta_{ij} - \delta_i + \delta_j\right)$$
(7.2.1)

$$\begin{bmatrix} \Delta\theta \\ \Delta U \end{bmatrix} = \underbrace{\begin{bmatrix} \frac{d\delta}{dP} & \frac{d\delta}{dQ} \\ \frac{dV}{dP} & \frac{dV}{dQ} \end{bmatrix}}_{J^{-1}=S} \begin{bmatrix} \Delta P \\ \Delta Q \end{bmatrix}$$
(7.2.2)

The sensitivity matrix is composed of four submatrices. The first row matrices provide information on the fluctuation of the voltage angle when the active or reactive power changes. A similar interpretation is possible in regard to the second-row matrices, which depict how much voltage is changed by active and reactive power variation. Therefore, sensitivity matrix S can be used to calculate the design variables in reactive power control methods. For example in [93] Eq. (7.2.1) is used to calculate power factor at the PCCs and also S matrix can be utilised to calculate the dead band region. Moreover, the electrolysers and batteries can be employed strategically at crucial buses according to the values in the first two matrices.

When the impedance is increased, both P and Q variations exert a stronger influence on the voltage. Due to the transformer windings, inverters connected closer to the transformer experience greater inductance than resistance. Consequently, the R/X ratio is lower, and in such instances, the $\frac{dV}{dQ}$ dominates the $\frac{dV}{dP}$. As the distance between the transformer and the PV inverter increases, the line's effective resistance becomes dominant. As a result, active power control provides superior voltage control across long distances in a distribution network compared to reactive power control approaches.Not only are

reactive power regulation systems used to lower voltages during peak irradiance, but they can also be configured to increase voltages during peak load demand. This additional step does not necessitate the establishment of any additional infrastructure. Additionally, as noted previously, in the dominating resistance situation, the energy supplied to the load by the batteries can greatly lower the voltage drop. A comprehensive deployment of all these these solutions could lower the overall cost and losses in the system. So further studies in this regard should be widely encouraged.

This project assumes a balanced three-phase system, and all the controllers and devices have been designed accordingly. However, due to single-phase connections and faults in existing distribution networks, there may be a greater likelihood of voltage imbalances. In that circumstances, voltages and currents must first be converted to positive, negative, and zero sequence components, and appropriate controllers for each sequence must be built for all loads. Such an approach closely reflects real-world settings; thus, further improvements in such studies is highly recommended.

Appendices

A

APPENDIX

A.1. SOLAR CELL TECHNOLOGIES

WAFER BASED SOLAR CELLS

Wafer-based solar cells are fabricated from the slices of crystals of the same material type. Currently, in the market, wafer-based solar cells hold the position for highest efficiency solar cells available [102]. The most popular and efficient cell types can be seen below.

Single crystalline silicon: Made from a single crystal of silicon. It is formed into bars and later cut into wafers. Maximum efficiency reached with this technology is 26.7% [20]. Commercially available crystalline silicon solar modules have lesser efficiencies varying from 15% to 22%[103]. Crystalline silicon modules accounted for 32% [103] of the total PV modules manufactured in the year 2017. This technology is highly matured, hence the silicon usage (g/Wp) has reduced drastically along with the wafer thickness. The theoretical maximum efficiency that can be reached with this technology is 29.4% [104]. Comparing this figure with the current maximum efficiency, it can be said that c-Si technology is very close to its saturation level. In figure A.3, the leftmost picture shows a single crystalline silicon solar panel.

Polycrystalline silicon: Unlike crystalline silicon, poly-crystalline silicon is made from multiple crystals of silicon. These wafers are cut from cast silicon ingots, produced by the cooling of molten silicon [105]. This results in polycrystalline silicon wafers. Due to the presence of a large number of defects at the grain boundaries because of multiple crystals, the efficiencies of Polycrystalline silicon cells are lower compared to crystalline silicon cells [104]. Maximum (lab) efficiency of this technology is around 23.3% [20]. Commercially available modules have lower efficiency between 15% and 18% [103]. Due to their cheaper prices and higher strength, polycrystalline silicon modules account for 60% [103] of the total PV modules manufactured annually. In figure A.3 in the middle a polycrystalline solar panel can be seen.

III-V group solar cells: These cells are made by merging 3rd and 5th group elements in the periodic table. A few examples are Gallium arsenide (GaAs) and Indium phosphide (InP). Therefore, GaAs solar cells have higher efficiencies comparatively. Maximum efficiency recorded is around 27.8% [20] for single-junction GaAs solar cell, however efficiencies of multi-junction GaAs cells can reach higher. GaAs is the preferred technology for outer space application due to its high efficiencies. The only downside of this technology is its price, due to this it is not widely available. In figure A.3 on the right a III-V group solar cell or multi-junction solar cell can be seen.

THIN FILM SOLAR CELLS

Amorphous silicon solar cells (a-Si): Amorphous silicon is a type of silicon which is not crystalline in nature. It has a continuous random network of silicon atoms with no long-range order. In this material, not all Si atoms have 4 Si neighbours. This results in higher defect density hence, increasing recombination of charge carriers [104]. Therefore, a-Si solar cells have lower efficiencies. Nonetheless, with cell efficiencies ranging between 5–7%, it is the most widely used thin-film technology. [20]. a-Si solar cells can also be made flexible and transparent, thus perfect for windows or railings. Due to the development of CdTe and CIGS thin-film technologies, the market share of a-Si has lessened [103].

Figure A.1: Monocrystalline, polycrystalline solar panel and a multi-junction solar cell [7]

Chalcogenides – Copper Indium Gallium Selenide solar cells (CIGS) : Chalcogenide is a chemical term that refers to all compounds that contain chalcogen anions from group VI in the periodic table. This material has a high absorption coefficient, high flexibility and diffusion length, which makes it an ideal material for thin-film applications. Maximum efficiency ever recorded is 23.4% [20]. Commercially available cells, on the other hand, are inefficient and more expensive than CdTe solar cells. Another difficulty with this technology is that Indium is a scarce metal that is mostly sourced from China. Although CIGS has a couple of disadvantages over CdTe, it has a lesser environmental impact than CdTe. This speciality has attracted many researchers and companies, leading to the rapid development of CIGS cells which further increased its market share in recent years [103].

Chalcogenides - Cadmium Telluride (CdTe) : This solar cell technology is the second most matured and widely available technology next to amorphous silicon . CdTe has a zinc-blend crystal structure. Cadmium telluride thin-films have higher efficiencies up to 22.1% [20]. They are also less expensive compared to standard silicon counterpart. CdTe technology has seen a tremendous boost in development over the past 15 years. However, due to the growing concerns over the environmental impacts of CdTe modules and also due to the increasing popularity of CIGS technology, the market share of CdTe technology is decreasing rapidly [103]. Nevertheless, CdTe cell efficiencies will continue to improve in the upcoming decades as a result of the increased rate of research and development.

Gallium arsenide (GaAs) : It is a semiconductor composed of two primary components: gallium and arsenic. GaAs is a direct bandgap material (ideal for thin-film applications). Hence they have very high efficiencies. As a result, multi-junctions based on III-V strongly outperforms all other PV technologies [20]. Few of the disadvantages of GaAs cells are toxicity and higher prices. Therefore the high-cost, high-performance GaAs technology is attractive for a niche market where very high power per unit area is crucial, such as in space applications and concentrated PV. No public data on industrially produced III-V is available. Breakthroughs in cost reduction are expected in coming years due to the increasing development of lower-cost deposition technologies, lift off and upscaling.
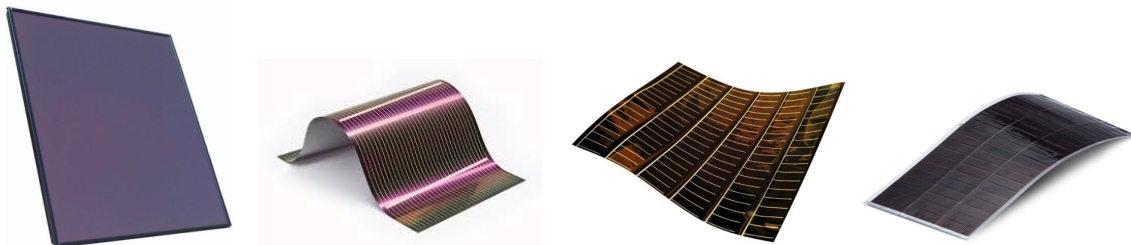
Figure A.2: From left to right: a-Si, CIGS, CdTe GaAs. [7], [8], [9], [10]

Dye-sensitized solar cells (DSSC) : DSSC is a photo electrochemical system, containing photo active dye material (electron donor), ruthenium polypyridine, mixed with TiO_2 nanoparticles (electron acceptor), an electrolyte, usually iodine, and a transparent front electrode and platinum contact. Electrons are collected at front contact where TiO_2 and TCO are present. It has a low-cost price of production but they are toxic in nature. This technology is relatively new and isn't matured yet. But DSSC have high poten-

tial to replace the traditional thin-film solar cells. The maximum efficiency reached by this technology is about 12.3 [20]%.

Organic solar cells : Organic solar cells contain an absorber layer made of carbon-based conductive organic polymers or organic molecules. Different organic solar cells can be produced, with varying material properties, often in a variety of colours. Few of the advantages are - potential low cost, low-temperature production and possibility to deposit on a mechanically flexible or a thin transparent substrate. Max efficiency ever recorded was about 17.5% [20].

Figure A.3: Left: DSSC Right: Organic solar cell [11], [12]

RECORD EFFICINCIES

This section summarises the efficiencies of all the different technologies that were ever reported. Efficiency is an important metric for the selection of particular solar cell technology. Hence it is highly imperative to have a rough idea of the efficiencies realized by various technologies. In the following, efficiencies of the important technologies are mentioned. Figure A.4 in appendix **??** depicts all the available PV technologies and their corresponding efficiencies recorded over the past few decades.

Crystalline silicon:

- c-Si: heterojunction with an interdigitated back contact. 26.7% (Kaneka) approaching theoretical efficiency limit of 29.4%.

- multicrystalline Si: PERC cells. 23.3% (Jinco Solar)

Thin film:

- A-Si: a-Si:H/nc-Si:H/nc-Si:H triple junction, 14.0% (AIST, Japan)

- CIGS: 23.4% (Solar frontier)

- CdTe: 22.1% (First Solar)

- III-V: single junction GaAs, 27.8% (LG)

- III-V: concentrated 6 junction bonded cell, 47.1% (NREL)

Third generation PV technologies:

- DSSC: 12.3% (EPFL)

- Organic: single junction, 17.5% . Tandem, 14.2%

- Perovskite: 24.2%
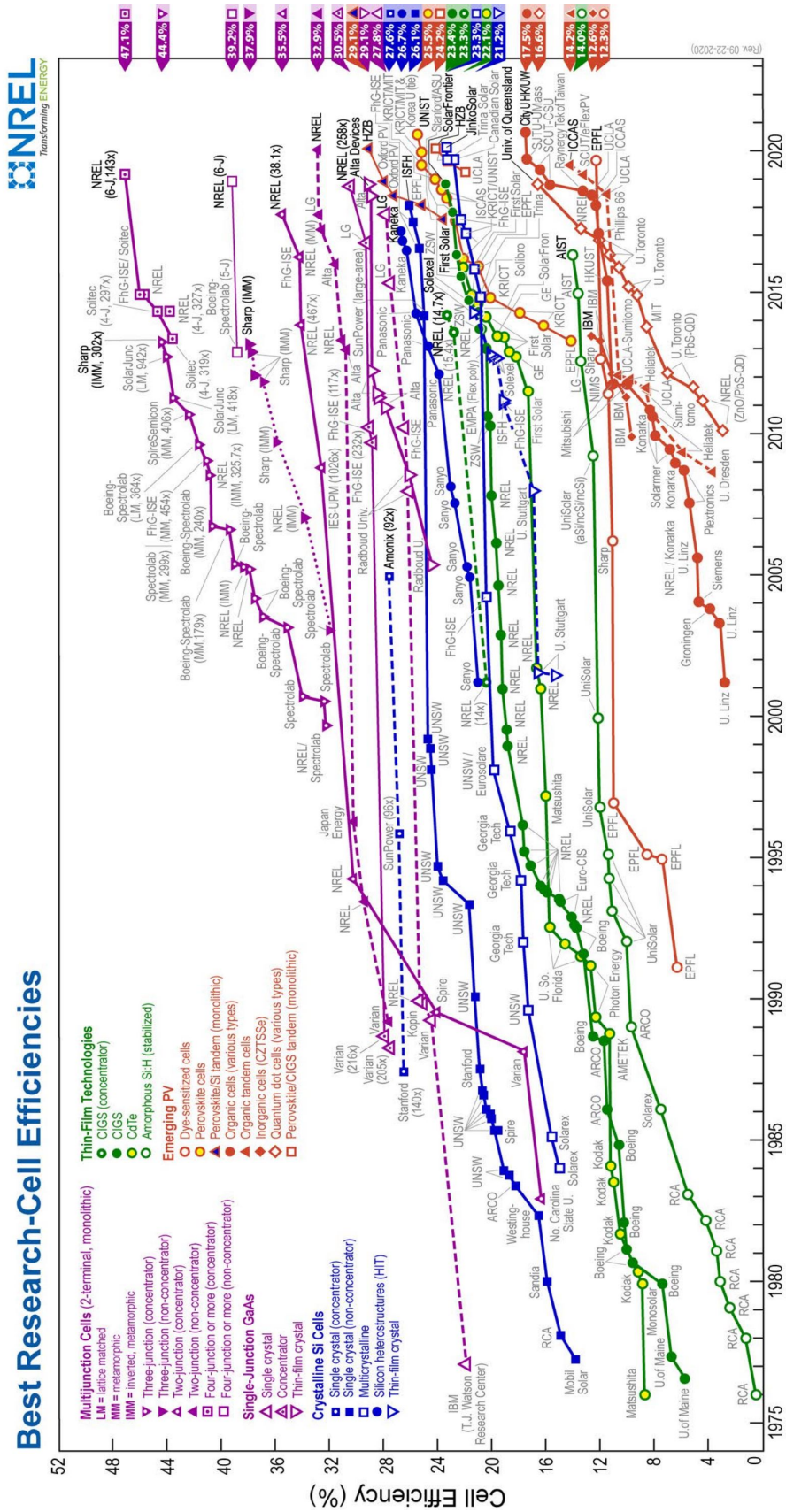
Figure A.4: Efficiencies of different PV technologies

A.2. Grid data

Three types of underground cables and overhead lines are used in the network. The geometry of both the overhead lines and underground cables and their respective specifications are given in the figure A.5, tables A.1 and A.2 respectively. Unlike transmission lines, the distribution lines are generally not transposed as they have shorter lengths. Because of this, the self and mutual inductance between the conductors have to be taken separately. This results in an N X N impedance matrix for a line consisting of N conductors. The diagonal elements in the matrix represent self-impedance, and the off-diagonal elements represent mutual impedance quantities. The primitive phase impedance matrices for all the lines and cables for the chosen distribution network are given in the tables A.3 and A.4

In an unbalanced scenario, for a three-phase-three-wire system, the unbalanced current or zero sequence current flows through the Earth via grounding systems when there is no return path through the neutral wire. Now, when there is current flowing through the Earth, the Earth acts as a conductor. Consider another system configuration, where there is multi-grounded neutral. So the network is a three-phase four-wire system with a neutral conductor. However, the grounding is done at different places. Hence, in this case, the zero-sequence current flows through the neutral wire as well as the Earth because of multi-grounded neutral. In either system, a fractional part of the current flows through the Earth. Due to this, there could be mutual impedance developed between the Earth and the other three-phase conductors. The problem here is that it is challenging to calculate the mutual impedance between the conductors because the Earth does not offer uniform resistance, and hence, the current path is not definite. This further complicates estimating the distance between the three-phase conductors and the effective earth conductors. To overcome such difficulties, Carson developed a bunch of equations (called Carson's equations) that can approximate the mutual impedances between various conductors (including Earth). Over the years, many simplifications are made, and Carson's equations are slightly modified. These equations are used to calculate primitive phase impedance matrices for the lines. Also, for a three-phase four-wire system, the primitive impedance matrix can be simplified using Kron reduction, where a 4 x 4 impedance matrix is converted into a 3 x 3 impedance matrix by considering the effect of the ground/neutral conductor's current on the phase conductors. Such conversion could simplify the design and modelling of a distribution network. Also, the kron reduction is beneficial if the simulator does not support the neutral wire inclusion in the model. In this thesis, the phase impedance matrix after kron reduction is utilized to model the feeder lines. The corresponding data has been given in the tables. A.5 and A.6 respectively. Line installation data and transformer parameters for each sub network are summarised in the tables A.7, A.8, A.9 and A.10.
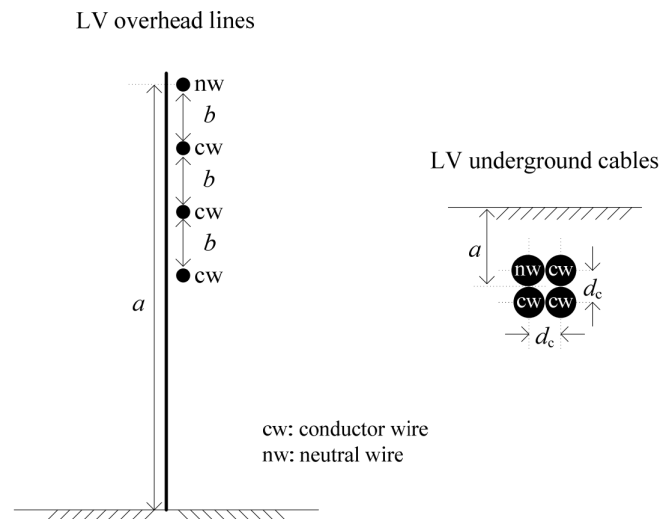
Figure A.5: The geometry of the overhead lines and underground cables [1]

Conductor ID	Type	Size	Number of strands	d_c	R'_{ac} at 50 ºC	GMR	a	b
		[mm²]		[cm]	[Ω/km]	[cm]	[m]	[m]
OH1	Al	70	19	1.05	0.491	0.398	8	0.3
OH2	Al	25	7	0.63	1.320	0.228	8	0.3
OH3	Al	16	7	0.51	2.016	0.185	8	0.3

Table A.1: Geometry of the overhead lines [1]

Conductor ID	Type	Size	Number of strands	d_c	R'_{ac} at 90 ºC / 70 ºC†	GMR	a
		[mm²]		[cm]	[Ω/km]	[cm]	[m]
UG1	NA2XY	240	1	1.75	0.162	0.634	0.90
UG2	NA2XY	150	1	1.38	0.265	0.501	0.90
UG3	NA2XY	50	1	0.80	0.822	0.289	0.90

Table A.2: Geometry of the underground lines [1]

Conductor ID/ Installation		The primitive impedance matrix [Ω/km]			
		A	B	C	N
OH1 / 3-ph	A	0.540 + j0.777	0.049 + j0.505	0.049 + j0.462	0.049 + j0.436
	B	0.049 + j0.505	0.540 + j0.777	0.049 + j0.505	0.049 + j0.462
	C	0.049 + j0.462	0.049 + j0.505	0.540 + j0.777	0.049 + j0.505
	N	0.049 + j0.436	0.049 + j0.462	0.049 + j0.505	0.540 + j0.777
OH2 / 3-ph	A	1.369 + j0.812	0.049 + j0.505	0.049 + j0.462	0.049 + j0.436
	B	0.049 + j0.505	1.369 + j0.812	0.049 + j0.505	0.049 + j0.462
	C	0.049 + j0.462	0.049 + j0.505	1.369 + j0.812	0.049 + j0.505
	N	0.049 + j0.436	0.049 + j0.462	0.049 + j0.505	1.369 + j0.812
OH3 / 3-ph	A	2.065 + j0.825	0.049 + j0.505	0.049 + j0.462	0.049 + j0.436
	B	0.049 + j0.505	2.065 + j0.825	0.049 + j0.505	0.049 + j0.462
	C	0.049 + j0.462	0.049 + j0.505	2.065 + j0.825	0.049 + j0.505
	N	0.049 + j0.436	0.049 + j0.462	0.049 + j0.505	2.065 + j0.825

Table A.3: Primitive impedance matrix of overhead lines [1]

Conductor ID/ Installation		The primitive impedance matrix [Ω/km]			
		A	B	C	N
UG1 / 3-ph	A	0.211 + j0.747	0.049 + j0.673	0.049 + j0.651	0.049 + j0.673
	B	0.049 + j0.673	0.211 + j0.747	0.049 + j0.673	0.049 + j0.651
	C	0.049 + j0.651	0.049 + j0.673	0.211 + j0.747	0.049 + j0.673
	N	0.049 + j0.673	0.049 + j0.651	0.049 + j0.673	0.211 + j0.747
UG2 / 3-ph	A	0.314 + j0.762	0.049 + j0.687	0.049 + j0.665	0.049 + j0.687
	B	0.049 + j0.687	0.314 + j0.762	0.049 + j0.687	0.049 + j0.665
	C	0.049 + j0.665	0.049 + j0.687	0.314 + j0.762	0.049 + j0.687
	N	0.049 + j0.687	0.049 + j0.665	0.049 + j0.687	0.314 + j0.762
UG3 / 3-ph	A	0.871 + j0.797	0.049 + j0.719	0.049 + j0.697	0.049 + j0.719
	B	0.049 + j0.719	0.871 + j0.797	0.049 + j0.719	0.049 + j0.697
	C	0.049 + j0.697	0.049 + j0.719	0.871 + j0.797	0.049 + j0.719
	N	0.049 + j0.719	0.049 + j0.697	0.049 + j0.719	0.871 + j0.797

Table A.4: Primitive impedance matrix of underground cables [1]

Conductor ID/ Installation		Phase impedance matrix after Kron reduction [Ω/km]		
		A	B	C
OH1 / 3-ph	A	0.616 + j0.588	0.131 + j0.306	0.141 + j0.245
	B	0.131 + j0.306	0.628 + j0.566	0.147 + j0.276
	C	0.141 + j0.245	0.147 + j0.276	0.650 + j0.527
OH2 / 3-ph	A	1.457 + j0.728	0.143 + j0.417	0.152 + j0.367
	B	0.143 + j0.417	1.469 + j0.720	0.159 + j0.405
	C	0.152 + j0.367	0.159 + j0.405	1.490 + j0.704
OH3 / 3-ph	A	2.137 + j0.776	0.125 + j0.453	0.133 + j0.406
	B	0.125 + j0.453	2.146 + j0.771	0.138 + j0.447
	C	0.133 + j0.406	0.138 + j0.447	2.163 + j0.762

Table A.5: phase impedance matrix of overhead lines after Kron reduction [1]

Conductor ID/ Installation		Phase impedance matrix after Kron reduction [Ω/km]		
		A	B	C
UG1 / 3-ph	A	0.287 + j0.167	0.121 + j0.110	0.125 + j0.070
	B	0.121 + j0.110	0.279 + j0.203	0.121 + j0.110
	C	0.125 + j0.070	0.121 + j0.110	0.287 + j0.167
UG2 / 3-ph	A	0.455 + j0.204	0.185 + j0.146	0.190 + j0.107
	B	0.185 + j0.146	0.444 + j0.238	0.185 + j0.146
	C	0.190 + j0.107	0.185 + j0.146	0.455 + j0.204
UG3 / 3-ph	A	1.152 + j0.458	0.321 + j0.390	0.330 + j0.359
	B	0.321 + j0.390	1.134 + j0.477	0.321 + j0.390
	C	0.330 + j0.359	0.321 + j0.390	1.152 + j0.458

Table A.6: phase impedance matrix of underground cables after Kron reduction [1]

Line segment	Node from	Node to	Conductor ID	l [m]	Installation
1	I1	I2	UG2	200	UG 3-ph

Table A.7: Line installation data for the Industrial subnetwork [1]

Line segment	Node from	Node to	Conductor ID	l [m]	Installation
1	R1	R2	UG1	35	UG 3-ph
2	R2	R3	UG1	35	UG 3-ph
3	R3	R4	UG1	35	UG 3-ph
4	R4	R5	UG1	35	UG 3-ph
5	R5	R6	UG1	35	UG 3-ph
6	R6	R7	UG1	35	UG 3-ph
7	R7	R8	UG1	35	UG 3-ph
8	R8	R9	UG1	35	UG 3-ph
9	R9	R10	UG1	35	UG 3-ph
10	R3	R11	UG3	30	UG 3-ph
11	R4	R12	UG3	35	UG 3-ph
12	R12	R13	UG3	35	UG 3-ph
13	R13	R14	UG3	35	UG 3-ph
14	R14	R15	UG3	30	UG 3-ph
15	R6	R16	UG3	30	UG 3-ph
16	R9	R17	UG3	30	UG 3-ph
17	R10	R18	UG3	30	UG 3-ph

Table A.8: Line installation data for the residential subnetwork [1]

Line segment	Node from	Node to	Conductor ID	l [m]	Installation
1	C1	C2	OH1	30	OH 3-ph
2	C2	C3	OH1	30	OH 3-ph
3	C3	C4	OH1	30	OH 3-ph
4	C4	C5	OH1	30	OH 3-ph
5	C5	C6	OH1	30	OH 3-ph
6	C6	C7	OH1	30	OH 3-ph
7	C7	C8	OH1	30	OH 3-ph
8	C8	C9	OH1	30	OH 3-ph
9	C3	C10	OH2	30	OH 3-ph
10	C10	C11	OH2	30	OH 3-ph
11	C11	C12	OH3	30	OH 3-ph
12	C11	C13	OH3	30	OH 3-ph
13	C10	C14	OH3	30	OH 3-ph
14	C5	C15	OH2	30	OH 3-ph
15	C15	C16	OH2	30	OH 3-ph
16	C15	C17	OH3	30	OH 3-ph

Table A.9: Line installation data for the Commercial subnetwork [1]

Node from	Node to	Connection	V_1 [kV]	V_2 [kV]	Z_{tr}† [Ω]	S_{rated} [kVA]
R0	R1	3-ph Dyn1	20	0.4	0.0032+j0.0128	500
I0	I1	3-ph Dyn1	20	0.4	0.0107+j0.0427	150
C0	C1	3-ph Dyn1	20	0.4	0.0053+j0.0213	300

Table A.10: Transformer parameters in all the subnetwork[1]

Bus	Active Power (KW)
R1	180
R11	14
R15	47
R16	31
R17	42
R18	50
I2	85
C1	100
C12	16.6
C13	16.6
C14	21
C17	21
C18	6.65
C19	9.3
C20	6.65

Table A.11: Maximum power consumed by the residential, commercial and industrial loads

A.3. PV SYSTEM PASSIVE COMPONENTS

Boost inductor, input capacitor, DC link capacitor and the LC filter has been designed according to the methods explained in the chapter 3. All the Passive components are calculated at STC conditions. The maximum irradtion calculated, reaches around 870 W/m^2 as shown in the figure 3.8. Therefore, the Pmax at STC should be slightly above the load peak consumption. All the values of the passive components of all the PV systems is given in the table A.12

	PV system connected to the Bus				
Component	**R11**	**R15**	**R16**	**R17**	**R18**
$C_{input}(\mu f)$	84.17	273.22	183.6	260	298
$L_{boost}(mh)$	1.3	0.415	0.616	0.435	0.379
$C_{DC}(mf)$	0.503	1.6	1.09	1.6	1.83
$L_{filter}(mh)$	1.8	0.55	0.822	0.58	0.5063
$R_{filter}(ohms)$	6.5	2	2.9	2.29	1.8
$C_{filter}(\mu f)$	79.1	256.75	172.57	244.46	280.31

Table A.12: Calculated values of the passive components

A.4. PV ARRAY CAPACITY

Since the entire residential network analysis is based on 100% PV penetration the PV arrays total capacity is chosen to be equal to the peak consumption of the loads connected to the same load bus. The The maximum load consumption values are given in the table A.11. The rating of the each PV system is given in the table A.13. As discussed in the previous section, the peak irradiation in a day is calculated to be around 870 w/m^2. So the given values in table correspond to the STC conditions. That is why the PV system ratings are slightly above the peak load consumption values. Also there are components like boost converter, LC fiter and transformer and a inverter in a PV system. They cause power losses. So, keeping in mind all these factors The PV systems are designed in such a way that at 870 w/m^2 the PV generated power is exactly equal to peak load consumption power.

PV system Connected to the bus	PV array capcity (KW)
R11	16.790
R15	54.500
R16	36.630
R17	51.890
R18	59.500

Table A.13: Ratings of various PV systems

A.5. REACTIVE POWER TECHNIQUES PARAMETERS

CONSTANT POWER FACTOR METHOD

The rating of all the inverter has been increased by 20% to accommodate Reactive power absorption. The final equation that governs reactive power absorption is given by-

$$Q = \tan(\arccos(C)) * P \tag{A.5.1}$$

Where, P is the PV power produced, Q is the reactive power that must be absorbed to keep the voltages under 1.1 p.u. The C in the equation is the power factor and it is the desired variable. The value of the minimum power factor required to keep the voltages under limit is 0.834. This value is obtained after running multiple simulation with various power factor values. The power factor 0.834 is same for all the PV systems

VARIABLE POWER FACTOR METHOD

All the invertes rating is increased by 20% except for the PV system connected to R16. Since the load connected to the bus R16 consumes significant amount of power, the inverter rating has to be increased slighlty above 20% to absorb more reactive power. So the power factor changes with PV power produced and is given by the equations-

$$\cos\varphi = \begin{cases} C_1, & P < P_1 \\ \frac{C_1 - C_2}{P_1 - P_2}(P - P_1) + C_1, & P_1 \leq P \leq P_2 \\ C_2, & P > P_2 \end{cases} \tag{A.5.2}$$

This control is designed in such a way that the power factor (C) is maintained constant when the PV power produced is below or above P_1 and P_2 respectively. The P_1 is chosen to be 35% of maximum power produced by the PV system. It means when PV starts to produce power more than the 35% of P_{MPP}, the power factor starts slowly going down. Prior to this point, the power factor is kept constant at one. P_2 is chosen to 100% of P_{MPP} as no additional power is produced beyond this point and the power factor cannot go below the value obtained at 100% of P_{MPP}. If the produced power is in between P_1 and P_2, the power factor has a linear relationship with produced power. The values selected for all the PV systems are summarised in the following table A.14-

PV system connected to the bus	C1	C2	P1	P2
R11	1	0.832	4900	1400
R15	1	0.832	16450	4700
R16	1	0.832	10850	31000
R17	1	0.832	14700	42000
R18	1	0.82	17500	50000

Table A.14: tab:Values of various parameters of multiple PV systems connected to their respective buses

These values are selected after running multiple simulations and noticing that they maintain the voltages below 1.1 p.u. successfully.

REACTIVE POWER AS A FUNCTION OF VOLTAGE

In this method the reactive power is absorbed based on the voltages recorded at PCC. The relationship between the reactive power absorbed and voltages at PCC can be given by

$$Q = \begin{cases} Q_1, & V < V_1 \\ \frac{Q_2 - Q_1}{V_2 - V_1}(V - V_1) + Q_1, & V_1 \le V \le V_2 \\ Q_2, & V > V_2 \end{cases} \tag{A.5.3}$$

The reactive power absorbed will be constant when voltages are below V_2 and above V_1 and linearly vary with the voltages when voltages are in between V_1 and V_2. The maximum voltage limit considered in this thesis is 1.1 p.u. because, generally it is at this voltage, where the protective devices disconnect the PV systems connected to the grid. Therefore, V_2 should be 1.1 p.u. V_1 is selected to be 1.05 p.u. value. Q_1 and Q_2 are the maximum and minimum reactive power absorbed by the inverter. The inverters rating has been increased by 20% of the maximum power generated by the PV modules. Since, during the peak irradiation, the maximum reactive power, a PV system can absorb is equal to its inverter's remaining capacity, the Q_2 is therefore must correspond to that 20% increase value. Q_1 is considered to be zero since no reactive power consumption is required below 1.05 p.u. The values of all the design parameters for all the PV systems is given in the table A.15.

PV system connected to the bus	V1	V2	Q1	Q2
R11	1.05	1.1	0	9286
R15	1.05	1.1	0	31170
R16	1.05	1.1	0	20560
R17	1.05	1.1	0	27850
R18	1.05	1.1	0	37210

Table A.15: Values of various parameters of multiple PV systems connected to their respective buses

CONSTANT REACTIVE POWER

In this method constant reactive power is being absorbed once the voltage crosses certain limit that limit considered to be 1.05 p.u. The inverters rating is increased by 20%. The reactive power absorbed must correspond to this value.

PV system connected to the bus	Q
R11	9286
R15	32170
R16	21110
R17	27850
R18	36110

Table A.16: Reactive power absorbed by multiple PV systems connected to their respective buses

A.6. K_p AND K_i PARAMETERS DERIVATION

This sections explains how the K_p and K_i parameters are calculated. This design is only valid for first order plant. In this design phase margin and settling time are the design parameters. A desired value for both the settling time T_s and phase margin (P_m) must selected. Typically the phase margin is between 70° and 80° for stability reason. If it is close to 90°, then it gives first order response which is quite sluggish in nature. If P_m is closer to zero, the feedback becomes positive leading to system instability. The derivation is as follows-
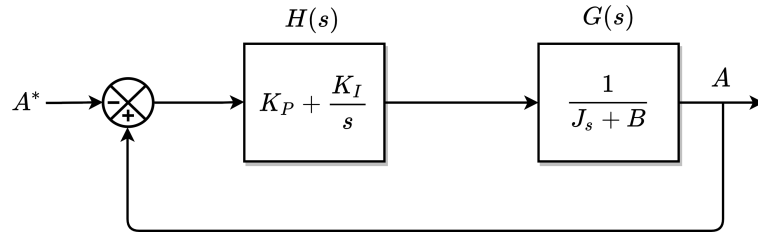
Figure A.6: Closed loop transfer function

The open loop gain of the above closed loop control (A.6) is-

$$GH = \left(K_P + \frac{K_I}{s}\right)\left(\frac{1}{Js+B}\right)$$

Phase margin is defined at gain crossover frequency ω_c as

$$PM = \angle^{le}(GH)\Big|_{\text{at } s=j\omega_c} - \left(-180°\right)$$

$$PM = \tan^{-1}\left(\frac{\omega_c K_P}{K_I}\right) - \tan^{-1}\left(\omega_C \frac{J}{B}\right) \quad -90° - \left(-180°\right)$$

After rearranging the above equation-

$$\left(\frac{\omega_C K_p}{K_I}\right) = \tan\left(PM - 90^0 + \tan^{-1}\left(\omega_c \frac{J}{B}\right)\right) \tag{A.6.1}$$

w_c is gain crossover frequency which can be obtained from the settling time equation $t_s = \frac{4}{\zeta\omega_n}$ with $\omega_c \simeq \omega_n$, where w_n is the location of the second order pole. Generally for the second order system $\omega_n < \omega_c$. So, to calculate t_s, lower value of t_s must be considered in the calculations to get the desired t_s.

$$\frac{1}{\omega_c}\left(\sqrt{(\omega_c K_P)^2 + K_I^2}\right)\left(\frac{1}{\sqrt{B^2 + (\omega_c J)^2}}\right) = 1 \tag{A.6.2}$$

After, rearranging the above equation-

$$k_I = \frac{\omega_c \sqrt{B^2 + (\omega_c J)^2}}{\sqrt{1 + \left(\frac{\omega_c K_P}{K_I}\right)^2}} \tag{A.6.3}$$

Since all the values are known in Eq. (A.6.1), $\left(\frac{\omega_C K_p}{K_I}\right)$ can be calculated and substituted in Eq. (A.6.3). Now, K_I is obtained. K_P can be calculated as,

$$k_P = \left(\frac{\omega_c K_P}{k_I}\right)\frac{k_I}{\omega_c} \tag{A.6.4}$$

Like mentioned before **this method is only suitable for the first order plant transfer function**. Also this whole method is an approximated method. Therefore, the K_P and K_I obtained through this method serves as a starting point and further tuning of these parameters can be done using control designer app in MATLAB.

INNER AND OUTER CONTROL LOOP
For the inner control loop,
$J = L/\omega = 0.2/314.16 = 0.000636618$
$B = R = 0.0035$

The K_p and K_i parameters are designed for $t_s = 20ms$. The values obtained are $k_p = 0.3$ and $K_i = 42.885$. Since L is per-unitised, the K_p and K_i parameters remains same for all the PV systems. Similarly, these

K_p and K_i parameters have been calculated for the outer control loop as well. However, due the the presence of P_b in the Eq. 3.9.13 the K_p and K_i parameters are different for different PV systems. The derived K_p and K_i parameters are given in the table A.17.

PV system connected to the bus	K_p	K_i
R11	20.28	135.885
R15	20.1635	135.0701
R16	19.1	129.64
R17	21.04	140.94
R18	19.765	132.4170

Table A.17: K_p and K_i parameters of outer control loop

BIBLIOGRAPHY

[1] K. Strunz, C. Abbey, C. Andrieu, R. C. Campbell, and R. Fletcher, <u>CIGRE Task Force C6.04.02</u>, July (2009).

[2] J. K.-I. O. v. S. R. . Z. M. Smets, A., <u>Solar Energy: The physics and engineering of photovoltaic conversion, technologies ar</u> (2016).

[3] B. K. Bose, <u>Power Electronics in Renewable Energy Systems and Smart Grid: Technology and Applications</u> (2019).

[4] *Working principle of a solar cell | Download Scientific Diagram,* .

[5] *Rectification of a Three Phase Supply using Diodes,* .

[6] E. Liu and J. Bebic, *Distribution system voltage performance analysis for high-penetration photovoltaics,* Renewable Energy Grid Integration: Technical Performance and Requirements , 107 (2011).

[7] M. Newkirk, *What are monocrystalline, polycrystalline and thin film solar panels?* (2014), consulted on: 2020-09-10.

[8] S. Feed, *Copper indium gallium selenide (cigs)?* (2019), consulted on: 2020-09-10.

[9] S. X. staff, *Efficiency record for flexible cdte solar cell due to novel polyimide film,* (2011), consulted on: 2020-09-10.

[10] S. McMahan, *Flying cell towers enabled by 29.1% efficient single-junction gaas solar cells - new industry products,* (2019), consulted on: 2020-09-10.

[11] D. Johnson, *Examining the new dawn of dye-sensitized solar cells with their discoverer,* (2011), consulted on: 2020-09-10.

[12] M. McGrath, *Organic solar cells set 'remarkable' energy record,* (2018), consulted on: 2020-10-20.

[13] A. Traupmann and T. Kienberger, *Test grids for the integration of RES-A contribution for the european context,* Energies **13** (2020), 10.3390/en13205431.

[14] A. Y. R. Iravani, <u>Voltage-Sourced Converters in Power Systems: Modeling, Control, and Applications</u> (2010).

[15] *What is climate change? A really simple guide - BBC News,* .

[16] *Global Temperature | Vital Signs – Climate Change: Vital Signs of the Planet,* .

[17] *Alarming rise in global temperatures,* .

[18] F. Cimato and M. Mullan, *PMS ??? Non-print 1 Non-print 2 C M Y K JOB LOCATION: PRINERGY 3 Defra Evidence and Analysis Series Adapting to Climate Change: Analysing the Role of Government,* (2010).

[19] *Photovoltaics Report,* .

[20] *Best Research-Cell Efficiency Chart | Photovoltaic Research | NREL,* .

[21] .

[22] *ON THE GLOBAL AND REGIONAL POTENTIAL OF RENEWABLE ENERGY SOURCES,* .

[23] D. government, *Residential electricity consumption in the Netherlands: A model-based policy analysis,* .

[24] *Rooftop Solar Photovoltaic - Global Opportunity Analysis and Industry Forecast, 2017-2023,* .

[25] M. M. Haque and P. Wolfs, *A review of high PV penetrations in LV distribution networks: Present status, impacts and mitigation measures,* Renewable and Sustainable Energy Reviews **62**, 1195 (2016).

[26] J. V. Paatero and P. D. Lund, *Effects of large-scale photovoltaic power integration on electricity distribution networks,* Renewable Energy **32**, 216 (2007).

[27] D. Cheng, B. A. Mather, R. Seguin, J. Hambrick, and R. P. Broadwater, *Photovoltaic (PV) impact assessment for very high penetration levels,* IEEE Journal of Photovoltaics **6**, 295 (2016).

[28] B. H. Chowdhury and A. W. Sawab, *Evaluating the value of distributed photovoltaic generations in radial distribution systems,* IEEE Transactions on Energy Conversion **11**, 595 (1996).

[29] *Gulachenski: Photovoltaic generation effects on distribut... - Google Scholar,* .

[30] J. Fitzer and W. E. Dillon, *IMPACT OF RESIDENTIAL PHOTOVOLTAIC POWER SYSTEMS ON THE DISTRIBUTION FEEDER.* IEEE Transactions on Energy Conversion **EC-1**, 39 (1986).

[31] J. Yaghoobi, N. Mithulananthan, and T. K. Saha, *Practical approach to facilitate photovoltaic integration in distribution systems,* The Journal of Engineering **2016**, 80 (2016).

[32] C. L. Masters, *Voltage rise the big issue when connecting embedded generation to long 11 kv overhead lines,* Power Engineering Journal **16**, 5 (2002).

[33] S. Ghosh, S. Rahman, and M. Pipattanasomporn, *Distribution Voltage Regulation Through Active Power Curtailment With PV Inverters and Solar Generation Forecasts,* IEEE Transactions on Sustainable Energy **8**, 13 (2017).

[34] Z. Zhang, C. Dou, D. Yue, B. Zhang, and P. Zhao, *High-economic PV power compensation algorithm to mitigate voltage rise with minimal curtailment,* International Journal of Electrical Power Energy Systems **125**, 106401 (2021).

[35] R. Luthander, D. Lingfors, and J. Widén, *Large-scale integration of photovoltaic power in a distribution grid using power curtailment and energy storage,* Solar Energy **155**, 1319 (2017).

[36] A. Hoke, R. Butler, J. Hambrick, and B. Kroposki, *Maximum Photovoltaic Penetration Levels on Typical Distribution Feeders Preprint Maximum Photovoltaic Penetration Levels on Typical Distribution Feeders,* (2012).

[37] P. R. Remus Teodorescu, Marco Liserre, GRID CONVERTERS FOR PHOTOVOLTAIC AND WIND POWER SYSTEMS (2011).

[38] *Voltage regulation in radial distribution feeders with high penetration of photovoltaic,* 2008 IEEE Energy 2030 Conference, ENERGY 2008 (2008), 10.1109/ENERGY.2008.4781021.

[39] E. Demirok, D. Sera, R. Teodorescu, P. Rodriguez, and U. Borup, *Evaluation of the voltage support strategies for the low voltage grid connected PV generators,* 2010 IEEE Energy Conversion Congress and Exposition, ECCE 2010 - Proceedings , 710 (2010).

[40] B. Ren, M. Zhang, and S. An, *Local Control Strategy of PV Inverters for Overvoltage Prevention in Low Voltage Feeder,* .

[41] P.-C. Chen, R. Salcedo, Q. Zhu, F. De León, D. Czarkowski, Z.-P. Jiang, V. Spitsa, and R. E. Uosef, *Analysis of Voltage Profile Problems Due to the Penetration of Distributed Generation in Low-Voltage Secondary Distribution Networks,* IEEE TRANSACTIONS ON POWER DELIVERY **27** (2012), 10.1109/TPWRD.2012.2209684.

[42] Jayakumar P and Reji P, *More realistic Approximate LV Feeder model for quick decision on PV interconnection requests,* .

[43] *Challenges of PV Integration in Low-Voltage Secondary Networks,* (2015), 10.1109/TP-WRD.2016.2556692.

[44] M. J. Weisshaupt, B. Schlatter, P. Korba, E. Kaffe, and F. Kienzle, *Evaluation of Measures to Operate Urban Low Voltage Grids Considering Future PV Expansion,* (2016), 10.1016/j.ifacol.2016.10.714.

[45] R. Kabiri, D. G. Holmes, and B. P. Mcgrath, *Voltage Regulation of LV Feeders with High Penetration of PV Distributed Generation Using Electronic Tap Changing Transformers,* .

[46] Z. Mehdi, M. Esmaeil, H. Golshan, and J. M. Guerrero, *Distributed Control of Battery Energy Storage Systems for Voltage Regulation in Distribution Networks with High PV Penetration,* , 1949 (2016).

[47] T. Verschueren, K. Mets, B. Meersman, M. Strobbe, C. Develder, and L. Vandevelde, *Assessment and mitigation of voltage violations by solar panels in a residential distribution grid,* .

[48] A. T. Procopiou and L. F. Ochoa, *Voltage Control in PV-Rich LV Networks without Remote Monitoring ,* 10.1109/TPWRS.2016.2591063.

[49] F. Lamberti, V. Calderaro, V. Galdi, A. Piccolo, and G. Graditi, *Impact Analysis of Distributed PV and Energy Storage Systems in Unbalanced LV Networks,* .

[50] C. T. Gaunt, E. Namanya, and R. Herman, *Voltage modelling of LV feeders with dispersed generation: Limits of penetration of randomly connected photovoltaic generation,* Electric Power Systems Research **143,** 1 (2017).

[51] *Increasing the PV Hosting Capacity with OLTC Technology and PV VAr Absortion in a MV/LV Rural Brazilian Distribution System,* .

[52] T. D. R. B. Seyedmostafa Hashemi, Jacob Østergaard and W. Heckmann, *Efficient Control of Active Transformers for Increasing the PV Hosting Capacity of LV Grids,* .

[53] *Resources | PES Test Feeder,* .

[54] *Pacific Northwest National Laboratory | PNNL,* .

[55] *A review of power distribution test feeders in the United States and the need for synthetic representative networks,* Energies **10** (2017).

[56] *EPRI Home,* .

[57] *European representative electricity distribution networks,* International Journal of Electrical Power and Energy Systems **99,** 273 (2018).

[58] *Development of an agent-based distribution test feeder with smart-grid functionality ,* Economics Presentations, Posters and Proceedings Economics (2012).

[59] *Non-synthetic European low voltage test system,* International Journal of Electrical Power Energy Systems **118,** 105712 (2020).

[60] K. A. Aganah and A. W. Leedy, *A constant voltage maximum power point tracking method for solar powered systems,* Proceedings of the Annual Southeastern Symposium on System Theory , 125 (2011).

[61] J. Ahmad, *A fractional open circuit voltage based maximum power point tracker for photovoltaic arrays,* ICSTE 2010 - 2010 2nd International Conference on Software Technology and Engineering, Proceedings **1** (2010), 10.1109/ICSTE.2010.5608868.

[62] *Short-current pulse-based maximum-power-point tracking method for multiple photovoltaic-and-converter module system,* IEEE Transactions on Industrial Electronics **49,** 217 (2002).

[63] *Design of a P--O algorithm based MPPT charge controller for a stand-alone 200W PV system,* Protection and Control of Modern Power Systems 2018 3:1 **3,** 1 (2018).

[64] *Maximum Power Point Tracking for Photovoltaic Using Incremental Conductance Method,* Energy Procedia **68**, 22 (2015).

[65] *Temperature based maximum power point tracking for photovoltaic modules,* Scientific Reports 2020 10:1 **10,** 1 (2020).

[66] I. C. O. S. C. T. M. Pierre Giroux, Gilbert Sybille (Hydro-Quebec, *Detailed Model of a 100-kW Grid-Connected PV Array,* .

[67] *intro - Meteonorm (en),* .

[68] R. Prakash and S. Singh, *Designing and Modelling of Solar Photovoltaic Cell and Array,* (2016).

[69] *Photovoltaic Module Modeling using Simulink/Matlab,* Procedia Environmental Sciences **17**, 537 (2013).

[70] *Implement PV array modules - Simulink - MathWorks Benelux,* .

[71] *Home - System Advisor Model (SAM),* .

[72] R. K. Naidu, *Design and development of control system for three phase grid integration of a 5.5KW photovoltaic system IIT (Master's thesis from IIT Kanpur -Y9104059),* (2011).

[73] D. B. Yelaverthi, *Grid integration of three level inverter for modular PV applications (Master's thesis from IIT Kanpur -11104031),* (2013).

[74] P. Sudeepika and G. M. Gayaz Khan, *Related papers Analysis Of Mat hemat ical Model Of PV Cell Module in Mat lab/Simulink Environment udayakumar vengat esan St udy of Partial shading effect on Solar Module Using MAT LAB International Journal of Advanced Research in Electrical, Electronics and Instrumentation Engineering Analysis Of Mathematical Model Of PV Cell Module in Matlab/Simulink Environment,* ().

[75] C.-S. T. Huan-Liang Tsai and Y.-J. Su, *Development of generalized photovoltaic model using MATLAB/SIMULINK,* .

[76] A. P. Dobos, *An Improved Coefficient Calculator for the California Energy Commission 6 Parameter Photovoltaic Module Model,* Journal of Solar Energy Engineering **134** (2012), 10.1115/1.4005759.

[77] S. Motahhir, *Contribution to the optimization of energy withdrawn from a PV panel using an Embedded System. (doctoral dissertation). University sidi mohammed ben abdellah, Fez, Morocco.* .

[78] *Implement PV array modules - Simulink - MathWorks Benelux,* .

[79] N. Mohan, T. M. Undeland, and W. P. Robbins, *Power Electronics Convertors, Applictions, and Design,* , 824 (2002).

[80] *250-kW Grid-Connected PV Array - MATLAB Simulink - MathWorks Benelux,* .

[81] *RLC Low-pass Filter Design Tool - Result -,* .

[82] Y. Levron, J. Belikov, and D. Baimel, *A Tutorial on Dynamics and Control of Power Systems with Distributed and Renewable Energy Sources Based on the DQ0 Transformation,* Applied Sciences 2018, Vol. 8, Page 1661 **8,** 1661 (2018).

[83] N. Hamrouni, S. Younsi, and M. Jraidi, *A Flexible Active and Reactive Power Control Strategy of a LV Grid Connected PV System,* Energy Procedia **162,** 325 (2019).

[84] B. Lang, H. Zhang, L. Sun, B. Wang, and X. Zheng, *Design of three phase grid-connected inverter based on grid-voltage oriented control,* Chinese Control Conference, CCC **2019-July,** 6525 (2019).

[85] M. Vijayrao, M. P. Reddy, and B. S. Reddy, *VOLTAGE-ORIENTED CONTROL OF A GRID CON-NECTED PV SYSTEM BY MODIFIED MPPT ALGORITHM,* .

[86] P. Sudeepika and G. M. Gayaz Khan, *Related papers Analysis Of Mat hemat ical Model Of PV Cell Module in Mat lab/Simulink Environment udayakumar vengat esan St udy of Part ial shading effect on Solar Module Using MAT LAB International Journal of Advanced Research in Electrical, Electronics ,* ().

[87] E. Romero-Cadaval, B. Francois, M. Malinowski, and Q. C. Zhong, *Grid-connected photovoltaic plants: An alternative energy source, replacing conventional sources,* IEEE Industrial Electronics Magazine **9**, 18 (2015).

[88] *Integration of Distributed Energy Resources in Power Systems: Implementation, Operation and Control,* Integration of Distributed Energy Resources in Power Systems: Implementation, Operation and Control , 1 (2016).

[89] C. Schauder and H. Mehta, *Vector analysis and control of advanced static VAR compensators,* IEE Proceedings C: Generation Transmission and Distribution **140**, 299 (1993).

[90] P. Sensarma, *Analysis and development of a distribution STATCOM for power quality compensation (A doctor of philosophy thesis from IISC Banglore),* (2000).

[91] *NPTEL :: Electrical Engineering - Power System Generation, Transmission and Distribution (Encapsulated from earlier Video),* .

[92] K. Turitsyn, P. Sulc, S. Backhaus, and M. Chertkov, *Local Control of Reactive Power by Distributed Photovoltaic Generators,* , 79 (2010), arXiv:1006.0160 .

[93] *Local reactive power control methods for overvoltage prevention of distributed solar inverters in low-voltage grids,* IEEE Journal of Photovoltaics **1**, 174 (2011).

[94] K. Turitsyn, P. Šulc, S. Backhaus, and M. Chertkov, *Distributed control of reactive power flow in a radial distribution circuit with high photovoltaic penetration,* IEEE PES General Meeting, PES 2010 (2010), 10.1109/PES.2010.5589663, arXiv:0912.3281 .

[95] M. Braun, *Reactive power supply by distributed generators,* IEEE Power and Energy Society 2008 General Meeting: Conversion and Delivery of Electrical Energy in the 21st Century, PES (2008), 10.1109/PES.2008.4596266.

[96] G. Mokhtari, G. Nourbakhsh, F. Zare, and A. Ghosh, *Overvoltage prevention in LV smart grid using customer resources coordination,* Energy and Buildings **61**, 387 (2013).

[97] Q. Xie, X. Shentu, X. Wu, Y. Ding, Y. Hua, and J. Cui, *Coordinated voltage regulation by on-load tap changer operation and demand response based on voltage ranking search algorithm,* Energies **12** (2019), 10.3390/en12101902.

[98] T. Fawzy, D. Premm, B. Bletterie, and A. Goršek, *Active contribution of PV inverters to voltage control - From a smart grid vision to full-scale implementation,* Elektrotechnik und Informationstechnik **128**, 110 (2011).

[99] Y. Zhou, L. Liu, and H. Li, *Autonomous control integrating fast voltage regulation and islanding detection for high penetration PV application,* Conference Proceedings - IEEE Applied Power Electronics Conference and Exposition - APEC , 606 (2011).

[100] H. B. Jürgen BACKES, Christian SCHORN, *Cost-Efficient Integration of Dispersed Generation Using Voltage Dependent Reactive Power Control,* Proc. of CIRED Workshop , 7 (2010).

[101] E. M. Darwish, H. M. Hasanien, A. Atallah, and S. El-Debeiky, *Reactive power control of three-phase low voltage system based on voltage to increase PV penetration levels,* Ain Shams Engineering Journal **9**, 1831 (2018).

[102] J. Runyon, *Wafer-based solar cells aren't done yet,* (2019), consulted on: 2020-09-22.

[103] Fraunhofer Institute for Solar Energy Systems, ISE, *Photovoltaic report,* (2018).

[104] A. H. M. Smets, J. Klaus, O. Isabella, R. A. C. M. M. v. Swaaij, and M. Zeman, Solar energy: the physics and engineering of photovoltaic conversion, technologies and systems (UIT Cambridge Ltd., 2016).

[105] N. D. Weimar, *Polycrystalline silicon cells: production and characteristics,* (2020), consulted on: 2020-09-25.